JSR

Journal of Sedimentary Research, 2025, v. 95, 1080–1113
Research Article
DOI: 10.2110/jsr.2025.019

SEDIMENTOLOGY AND STRATIGRAPHY OF THE FLUVIAL–DELTAIC SKRINKLE HAVEN MEMBER, TENBY FORMATION, JEZERO CRATER, MARS

LIBBY R.W. IVES,[1,2] KATHRYN M. STACK,[1] EMILY C. GEYMAN,[3] SANJEEV GUPTA,[4] GWÉNAËL CARAVACA,[5,6] KIRSTEN L. SIEBACH,[7] SAMANTHA GWIZD,[1] JOHN P. GROTZINGER,[3] MICHAEL P. LAMB,[3] NICOLAS MANGOLD,[8] OAK KANINE,[3] ROBERT BARNES,[4] PATRICK RUSSELL,[9] JORGE I. NÚÑEZ,[10] JUSTIN I. SIMON,[11] BENJAMIN P. WEISS,[12] AILEEN YINGST,[13] SUNANDA SHARMA,[14] STÉPHANE LE MOUÉLIC,[8] JOSHUA HUGGETT,[15] ALYSSA PASCUZZO,[15] BRITTAN WOGSLAND,[16] WOODWARD W. FISCHER,[3] AND NICOLAS RANDAZZO[17]

[1]*Jet Propulsion Laboratory, California Institute of Technology, Pasadena, California, U.S.A.*
[2]*Michigan Geological Survey, Department of Geological and Environmental Sciences, Western Michigan University, Gwinn, Michigan, U.S.A.*
[3]*Division of Geological and Planetary Sciences, California Institute of Technology, Pasadena, California, U.S.A.*
[4]*Department of Earth Science and Engineering, Imperial College, London, U.K.*
[5]*Laboratoire Géosciences Environnement Toulouse, UMR 5563 CNRS, IRD, UPS, CNES, Université Paul Sabatier Toulouse III, Toulouse, France*
[6]*Institut de Recherche en Astrophysique et Planétologie, UMR 5277 CNRS, UPS, CNES, Université Paul Sabatier Toulouse III, Toulouse, France*
[7]*Department of Earth, Environmental and Planetary Sciences, Rice University, Houston, Texas, U.S.A.*
[8]*Laboratoire Planétologie et Géosciences, Centre National de Recherches Scientifiques, Nantes Université, Nantes, France*
[9]*Department of Earth and Planetary Research Sciences, University of California–Los Angeles, Los Angeles, California, U.S.A.*
[10]*Johns Hopkins University, Applied Physics Laboratory, Laurel, Maryland, U.S.A.*
[11]*Astromaterials Research and Exploration Science, NASA Johnson Space Center, Houston, Texas, U.S.A.*
[12]*Department of Earth, Atmospheric and Planetary Sciences, Massachusetts Institute of Technology, Cambridge, Massachusetts, U.S.A.*
[13]*Planetary Science Institute, Tucson, Arizona, U.S.A.*
[14]*Earth and Planets Laboratory, Carnegie Institution for Science, Washington D.C., U.S.A*
[15]*Malin Space Science Systems, San Diego, California, U.S.A.*
[16]*Earth, Environmental, and Planetary Sciences Department, The University of Tennessee Knoxville, Knoxville, Tennessee, U.S.A.*
[17]*Department of Earth and Atmospheric Sciences, University of Alberta, Edmonton, Alberta, Canada*
e-mail: elizabeth.ives@wmich.edu

ABSTRACT: **In 2023, the Mars 2020 *Perseverance* rover investigated the Skrinkle Haven member of the Tenby formation in the > 3.5-billion-year Jezero Crater western fan. This unit was interpreted from orbiter data as bank attached, lateral-accretion bars in a sinuous river on a muddy delta plain. To test that hypothesis, this study applies facies and stratigraphic analyses of both rover and orbiter data. Rover images show that the Skrinkle Haven member is composed of two lithofacies: a fine-grained sandstone and a pebble conglomerate. Both lithofacies are composed of structureless, ungraded, planar-parallel beds that have sharp, nongradational contacts and depositional angles up to ∼ 30°. These characteristics indicate that grain flow was the main depositional process and that the sedimentary bodies were built through downstream accretion. Architectural analysis suggests that the Skrinkle Haven member was deposited primarily as delta foresets and mouth bars, with limited river bar deposition. The sequence stratigraphic analysis identified five maximum-flooding surfaces associated with relative-lake-level increases ranging from 5 to 25 m. In the sequences, deltaic strata prograded during normal and forced regressions. Some sequences have evidence for compensational stacking. Lake levels decreased through time both within sequences and throughout the duration of the Skrinkle Haven member deposition, from at least –2415 m in the oldest sequence to at most –2455 m in the youngest. The elevation range of the Skrinkle Haven member is below the modern Jezero Crater outlet breach, suggesting that the Jezero Crater lake basin was closed at that time. Overall, the Skrinkle Haven member records the deposition of a sandy to conglomeratic deltaic system that prograded into a closed lake basin during both forced and normal regressions. This type of fluvial–deltaic system is significantly different from the muddy delta topsets originally interpreted from orbiter data, because of the different implications for biosignature preservation and the paleohydrology of the Jezero Crater.**

INTRODUCTION

Sedimentary rocks are widespread on the surface of Mars (Malin and Edgett 2000; Grotzinger and Milliken 2012; Edgett and Sarkar 2021). Since NASA's *Viking* missions in the 1970s, sedimentary rocks on Mars have been studied using remotely sensed images from orbiting spacecraft and ground-based robotic missions (see Grotzinger and Milliken (2012) and McLennan et al. (2019) for reviews). These sedimentary rocks are interpreted to have been deposited through aqueous (e.g., Williams et al. 2013; Gwizd et al. 2024a; Stack et al. 2024), aeolian (e.g., Grotzinger et al. 2005; Banham et al.

Published Online: December 2025
 1527-1404/25/095-1080

2018), and glacial processes (Milliken et al. 2003; Butcher et al. 2024) and subsequently cemented. The deposition and cementation of sedimentary rocks on Mars largely occurred between ~ 4 and 3 billion years ago (Ga) when the atmosphere was thicker and climatic conditions were wetter and warmer than today (Wordsworth 2016; Kite 2019). In contrast to their Archean and Proterozoic counterparts on Earth, ancient sedimentary deposits present on the surface of Mars today are commonly preserved in their original depositional location because Mars has likely never experienced plate tectonics (e.g., Breuer and Spohn (2003)). Such rocks are primary records of the climate, environments, processes, and potential habitability of the ancient Martian surface, and potential analogs for the early evolution of other rocky planets in our solar system, including Precambrian surface environments on Earth (Lapôtre et al. 2020, 2022).

This study uses data collected on Mars by the Mars 2020 *Perseverance* rover (Farley et al. 2020). The objectives of the Mars 2020 mission include characterizing the geology and past habitability of Jezero Crater and the surrounding region (Fig. 1), and collecting scientifically compelling samples as part of the Mars Sample Return campaign (Beaty et al. 2019; Farley et al. 2020). Orbiter data show that Jezero Crater contains geomorphic, sedimentary, and mineralogical evidence of water (Fassett and Head 2005; Ehlmann et al. 2008), including a fan-shaped deposit of sedimentary rocks dubbed the Jezero Crater western fan, located downstream of the large inlet channel Neretva Vallis (Fig. 1C, D). Since beginning surface operations in February 2021, *Perseverance* has enabled a more thorough understanding of the sedimentary geology of the western fan (Caravaca et al. 2024; Gupta et al. 2024; Mangold et al. 2024; Stack et al. 2024b). Perseverance has also collected 13 sedimentary rock cores from Neretva Vallis and the western fan (Farley and Stack 2023, 2024a, 2024b; Herd et al. 2025).

Between March and June 2023, *Perseverance* collected observations of a group of sedimentary rocks in the western fan designated the Skrinkle Haven member (mbr) of the Tenby formation (fm) (Figs. 1D, 2, 3). This unit was known from orbiter data as the "curvilinear unit" due to the distinct planform geometry of sedimentary bodies that constitute it (Goudge et al. 2018; Stack et al. 2020). The consensus hypothesis before *Perseverance*'s landing was that the Skrinkle Haven mbr was deposited by lateral-accretion of bank-attached fluvial bars in a sinuous river on a delta plain (Schon et al. 2012; Goudge et al. 2018; Lapôtre and Ielpi 2020). However, interpretations of on-the-ground observations from *Perseverance* of similar strata elsewhere in the western fan suggest that a deltaic-foreset hypothesis is more appropriate for the curvilinear unit strata (Mangold et al. 2021, 2024; Caravaca et al. 2024).

This study uses orbiter and *Perseverance* rover data to determine the depositional origin of the Skrinkle Haven mbr and test the hypotheses that its strata were deposited as laterally accreting point bars in a meandering fluvial system (Schon et al. 2012; Goudge et al. 2018) or as deltaic foresets. This study characterizes the depositional environment of the Skrinkle Haven mbr by describing its lithofacies, sedimentary architecture, and sequence stratigraphy. This work uses new observations from instruments on board *Perseverance* along with remotely sensed orbiter images and elevation data.

Differentiating between a fluvial setting and a delta-foreset setting is important since those scenarios have different implications for relative lake levels during deposition and therefore would establish different paleolacustrine histories of Jezero Crater. This work contributes to understanding the depositional history of the Jezero Crater western fan and therefore the history of ancient water, surficial conditions, and habitability in Jezero Crater. Additionally, this work provides geologic context for the "Melyn" sedimentary rock core sample (Fig. 2A, C) which was collected by *Perseverance* from the Skrinkle Haven mbr (Farley and Stack 2024b; Weiss et al. 2024; Herd et al. 2025) and may be returned to Earth for study as part of the Mars Sample Return mission.

GEOLOGIC SETTING

Jezero Crater Geography

Jezero Crater is an ~ 45-km-diameter impact crater located along the northwestern edge of Isidis Planitia in the southeastern Nili Fossae region of Mars (18.4°N, 77.7°E; Fig. 1A, B). The crater is thought to have formed during the late Noachian period between 3.96 Ga (Werner 2008) and 3.82 Ga (Mandon et al. 2020). Jezero Crater has paleogeomorphic features that indicate that water was once an active and powerful agent of surficial change in the crater and the surrounding region (Fassett and Head 2005; Schon et al. 2012). Two notable landforms are the bedrock inlet valleys, Neretva Vallis and Sava Vallis (Fig. 1C). These valleys appear to have drained an area northwest of the crater (Fassett and Head 2005; Goudge et al. 2015; Mangold et al. 2020). The combined watershed areas feeding these valleys have been estimated to be between ~ 15,000 km^2 and ~ 30,700 km^2 (Fassett and Head 2005; Goudge et al. 2015; Mangold et al. 2020). This range is similar to the moderately sized watershed area of regionally important terrestrial rivers such as the River Thames in the United Kingdom (~ 16,000 km^2). The slopes of discrete reaches of the modern Neretva Vallis channel range from 0.7% to 1.7% (Mangold et al. 2020) which are similar to channel slopes of terrestrial rivers in mountainous regions (e.g., Cohen et al. 2018).

Neretva Vallis and Sava Vallis end in Jezero Crater downstream of where they incise the crater rim (Fig. 1C). Two coalesced sedimentary fans are present downstream of where the valleys enter the crater (Fig. 1C) (Fassett and Head 2005; Schon et al. 2012; Goudge et al. 2015, 2018; Mangold et al. 2020; Stack et al. 2020; Jodhpurkar et al. 2024). The preserved western fan is ~ 7 km long, ~ 10 km wide, has a surface area of ~ 26 km^2, and a maximum height of ~ 210 m above the igneous and volcanic crater floor. Counts of impact craters on the Jezero Crater western fan indicate a minimum depositional age of 3.5 (+0.1/−0.3) Ga (Mangold et al. 2020). Jezero Crater also has a bedrock outlet valley (Pliva Vallis) that begins where it incises the eastern crater rim with a brink-point elevation of around –2400 m (Fig. 1C). The presence of this paleo-outlet channel indicates that the crater was filled at least once with sufficient water to incise an exit down to an elevation of ~ 200 m above the modern crater floor (Salese et al. 2020; Fassett and Goudge 2021; Villette et al. 2025). Geomorphic evidence from Pliva Vallis suggests that multiple flood events led to incision of the brink-point and valley through time (Villette et al. 2025). The crater would have acted as an open lake basin when lake levels in the crater exceeded the outlet's brink-point elevation, and as a closed lake basin when lake levels were below that outlet elevation.

Previous Work

Before the Mars 2020 mission, the origin of the Jezero Crater fans was interpreted using orbiter datasets. A deltaic origin for both the northern and western Jezero Crater fans was initially proposed by Fassett and Head (2005) based on the planform morphology of the fans and the similar elevation of the fan tops to the Pliva Vallis outlet channel. This hypothesis was bolstered by spectral observations collected by the Compact Reconnaissance Imaging Spectrometer for Mars instrument (CRISM; Murchie et al. 2009) on the Mars Reconnaissance Orbiter (MRO; Zurek and Smrekar 2007) that were interpreted by Ehlmann et al. (2008) to show evidence for Fe-Mg smectite minerals in the Jezero Crater western fan. Ehlmann et al. (2008) used the smectite observations in combination with MRO High-Resolution Imaging Science Experiment (HiRISE; McEwen et al. 2007) images of the Jezero Crater western fan to infer the presence of distinct delta lobes and fluvial lateral-accretion sets in the western fan. This interpretation of fluvial lateral-accretion sets was based on the observation of features described as epsilon cross-beds and the interpretation of those features as scroll bars created as migrating point bars formed through lateral accretion in a muddy, clay-rich, delta-top fluvial setting (Schon et al. 2012). The Fe-Mg smectite detected in the western fan was predicted to be detrital in origin instead of authigenic because similar spectral signatures were observed in potential source rocks in the Jezero Crater watershed (Ehlmann et al. 2008; Goudge et al. 2015).

Subsequently, Schon et al. (2012) expanded on the prior observation of epsilon cross-bedding and inferred scroll bars, arguing that the surficial expression of curvilinear strata in the Jezero Crater western fan is representative of ridge-and-swale topography (e.g., Nanson 1980). Goudge et al. (2017, 2018)

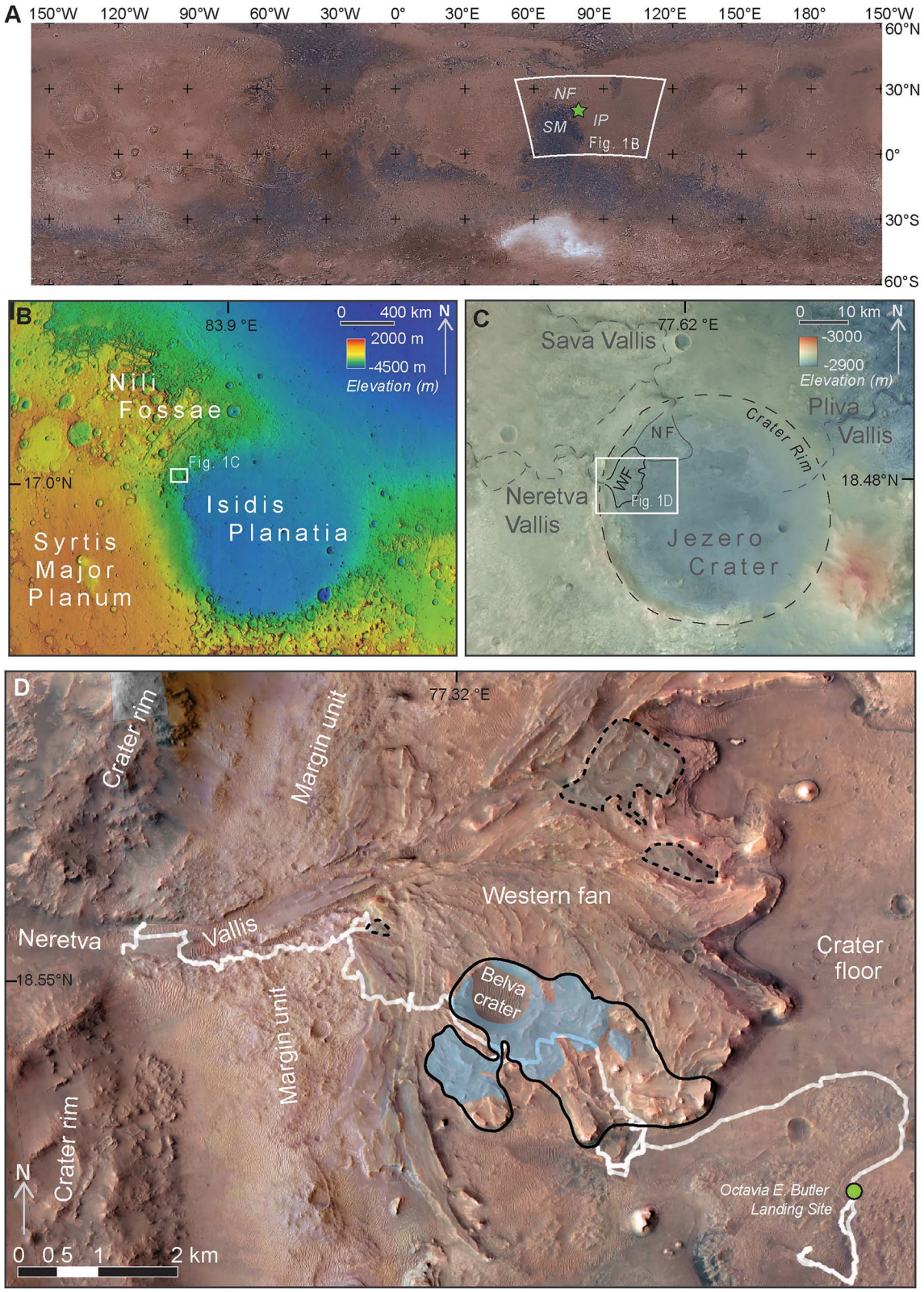

FIG. 1.—Orbiter images showing the global and regional context of the Jezero Crater western fan, Mars (Table S3). **A)** Colorized-image mosaic of Mars' surface showing the global context of Jezero Crater (location indicated by green star) at the junction of three regions of Mars: Isidis Planatia (IP) lies within a giant, ~ 3.96 Ga impact crater (Werner 2008), Syrtis Major Planum (SM) is a large dark-toned region of Mars that derives its color from extensive mafic lava flows that are likely ~ 3.5–3.8 Ga (Hiesinger and Head 2004; Bramble et al. 2017), and Nili Fossae (NF) is a series of grabens that formed in country rocks of enigmatic composition and origin (Mandon et al. 2020). The white outline indicates the extent of Part B. The basemap is an equiangular projection of the Mars Viking Colorized Global Mosaic (USGS Astrogeology Science Center 2009).

corroborated this fluvial hypothesis by using HiRISE images and HiRISE-derived elevation data products to measure the geometry of strata in the Jezero Crater western fan, and interpreting the strata as point-bar deposits. Subsequent studies used this fluvial hypothesis to inform calculations of potential discharge through the Neretva Vallis channel system and rates of Jezero Crater western fan deposition (Goudge et al. 2018; Lapôtre and Ielpi 2020; Salese et al. 2020).

At the time *Perseverance* operations began, there was considerable confidence that the Jezero Crater western fan was deposited as a delta and that the curvilinear unit identified from orbit represented topsets of this delta deposited as laterally accreting bars in a sinuous river channel with floodplains rich in detrital clay during individual flood events. Based on this depositional interpretation and the resulting stratigraphic analysis, Goudge et al. (2018) concluded that the strata of the curvilinear unit were deposited during a transgression produced by a gradual increase in lake levels in the Jezero basin.

Geologic and Stratigraphic Context from the Rover Perspective

Observations collected by instruments onboard *Perseverance* have enabled detailed characterization of the geology of Jezero Crater, including the sedimentology and stratigraphy of the Jezero Crater western fan. The sedimentary rocks of the western fan unconformably overlie mafic igneous and volcanic units of the crater floor (Farley et al. 2022; Liu et al. 2022; Wiens et al. 2022; Beyssac et al. 2023; Simon et al. 2023; Sun et al. 2023; Paige et al. 2024). Pre-landing orbiter observations identified three distinct sedimentary rock types making up the lower, middle, and upper parts of the fan (Goudge et al. 2018; Stack et al. 2020).

On-the-ground rover observations have confirmed that these three orbitally identified sedimentary rock types correspond to three distinct sedimentary units: the Shenandoah fm, the Tenby fm, and the Otis Peak fm (Fig. 3). The base of the fan is made up of the ~ 25-m-thick Shenandoah fm (Fig. 3) (Stack et al. 2024). The Shenandoah fm is a fining-upward clastic sedimentary succession of laminated fine-grained sandstone and mudstone intercalated with lenses of granule and pebbly sandstone (Fig. 3C). This succession has been interpreted to represent an unconfined, distributive depositional system—either a distal alluvial fan (Stack et al. 2024) or a turbidite system (Tebolt et al. 2025).

The relatively flat-lying strata of the Shenandoah fm are erosionally overlain by coarse-grained, often steeply dipping strata of the Tenby fm (Fig. 3) (Gupta et al. 2024; Mangold et al. 2024; Stack et al. 2024). The Tenby fm is generally composed of coarse-grained sandstones and conglomerates with diverse sedimentary architectures, which have been divided into the Rockytop mbr, the Franklin Cliffs mbr, the Skrinkle Haven mbr, and the Carew Castle mbr (Fig. 3). The Rockytop mbr is up to 20 m thick and is made up of lenses of dipping, planar, thin-bedded sandstone and conglomerate couplets that are interpreted as distal delta foresets (see Facies Association 3 of Stack et al. 2024). The Franklin Cliffs mbr is up to 50 m thick and is composed of steeply inclined, pebbly and cobbly coarse-grained sandstone beds that are overlain by conglomeratic fluvial strata. These units are interpreted to be delta foresets and gravel-rich fluvial topsets (Mangold et al. 2024). The Skrinkle Haven mbr, the topic of this paper, is also up to 50 m thick and consists of steeply dipping sandstone and conglomerate beds. Although both the Skrinkle Haven mbr and the Franklin Cliffs mbr contain steeply dipping strata, the Skrinkle Haven mbr is distinguished in two ways. First, the Skrinkle Haven mbr does not include the same fluvial strata (interpreted topsets) as the Franklin Cliffs mbr. Second, the sandstones and conglomerates of the Skrinkle Haven mbr have sharp contacts and alternate in a pseudo-rhythmic fashion. The Carew Castle mbr consists of a 25-m-thick succession of cross-stratified sandstone and conglomerates that overlies an erosional contact with the Skrinkle Haven mbr (Fig. 3). Though some members of the Tenby fm tend to occur at higher or lower elevations than others (Fig. 3), their stratigraphic order is likely not as straightforward. This lateral variability is not reflected in the synthetic column in Figure 3C.

The Otis Peak fm overlies an erosional unconformity with the Tenby fm (Fig. 3). This unit is organized into distinct lobes on the top of the western fan that are thought to correspond to erosionally inverted channel-belt deposits (Goudge et al. 2018; Kronyak et al. 2023; Gwizd et al. 2024b). The Otis Peak fm lithologies include planar-bedded and cross-bedded sandstone to pebble conglomerate, boulder conglomerate, and a mafic igneous unit (Fig. 3A, C) (Gwizd et al. 2024b).

DATA AND METHODS

Data Sources

The lithofacies of the Skrinkle Haven mbr were characterized using rover instrument observations, and the sedimentary architecture and sequence stratigraphy were largely characterized using orbiter data aided by rover observations. Rover and orbiter data sources are described in Table 1 and Supplementary File S2. Observations of the Skrinkle Haven mbr were made between mission sols 715 and 836 (between March and June 2023) (Fig. 2A).

METHODS

Lithofacies Characterization.—Lithofacies descriptions and interpretations were made based on various scale images of outcrops, workspaces, and targets, all collected by rover instruments (Table 1; Supplementary File S2).

Grain-size data were collected by point count and grain tracing on colorized SHERLOC ACI (Table 1) images of the Solva and Solitude Lake abrasion patches (Figs. 2, 4). The methods used were aimed at replicating classic thin-section point-counting techniques but with the high-resolution ACI images of a section of the abrasion patch surface. Grain sizes were classified according to Wentworth (1922). ACI images were imported into Adobe Illustrator and overlaid by a 0.5 mm grid. Each grid intersection point was classified as having "Data" or "No Data." Data points were classified as being a grain, intergranular cement, intragranular cement, or void. No Data points were due to either the point being covered by dust or the image at that point being unclear. The Solva and Solitude Lake targets yielded 562 and 566 data points, respectively. Where a point overlies a grain, that grain's outer edge was traced in Adobe Illustrator. The long axis of each grain trace was measured using Feret's Diameter function in the software ImageJ (Schneider et al. 2012). This long axis length was treated as an approximation of grain-size and used to calculate grain size distribution and sorting for each abrasion patch.

Characterization of Sedimentary Architecture.—The stratigraphic architecture of the Skrinkle Haven mbr was characterized using observations from orbiter data and validated with rover data wherever possible (Table 2). First-order architectural units of the Skrinkle Haven mbr are individual beds

←

B) Regional context of Jezero Crater, the Mars 2020 *Perseverance* landing site and exploration area, shown on a digital elevation model and derived hillshade from Mars Orbiter Laser Altimeter (MOLA) and High-Resolution Stereo Camera (HRSC) data (Fergason et al. 2018). **C)** DTM overlaid on a Context Camera (CTX) basemap (Dickson et al. 2023) of Jezero Crater and surrounding region showing the location of the main inlet (Neretva and Sava) and outlet (Pliva) valleys, western fan (WF) and northern fan (NF) deposits, and crater rim and floor. **D)** *Perseverance's* traverse (white line) in Jezero Crater from the Octavia E. Butler Landing Site (green dot; sol 0) to the sol 1232 rover position annotated on a High Resolution Imaging Science Experiment (HiRISE) false-color, orthophoto mosaic (Fergason et al. 2020). The solid black line indicates the likely outcrop extent of the Tenby fm, and the blue shaded area within that indicates where the Skrinkle Haven mbr crops out. The black dashed line indicates areas on the western fan surface where sedimentary rocks similar to the Skrinkle Haven mbr crop out.

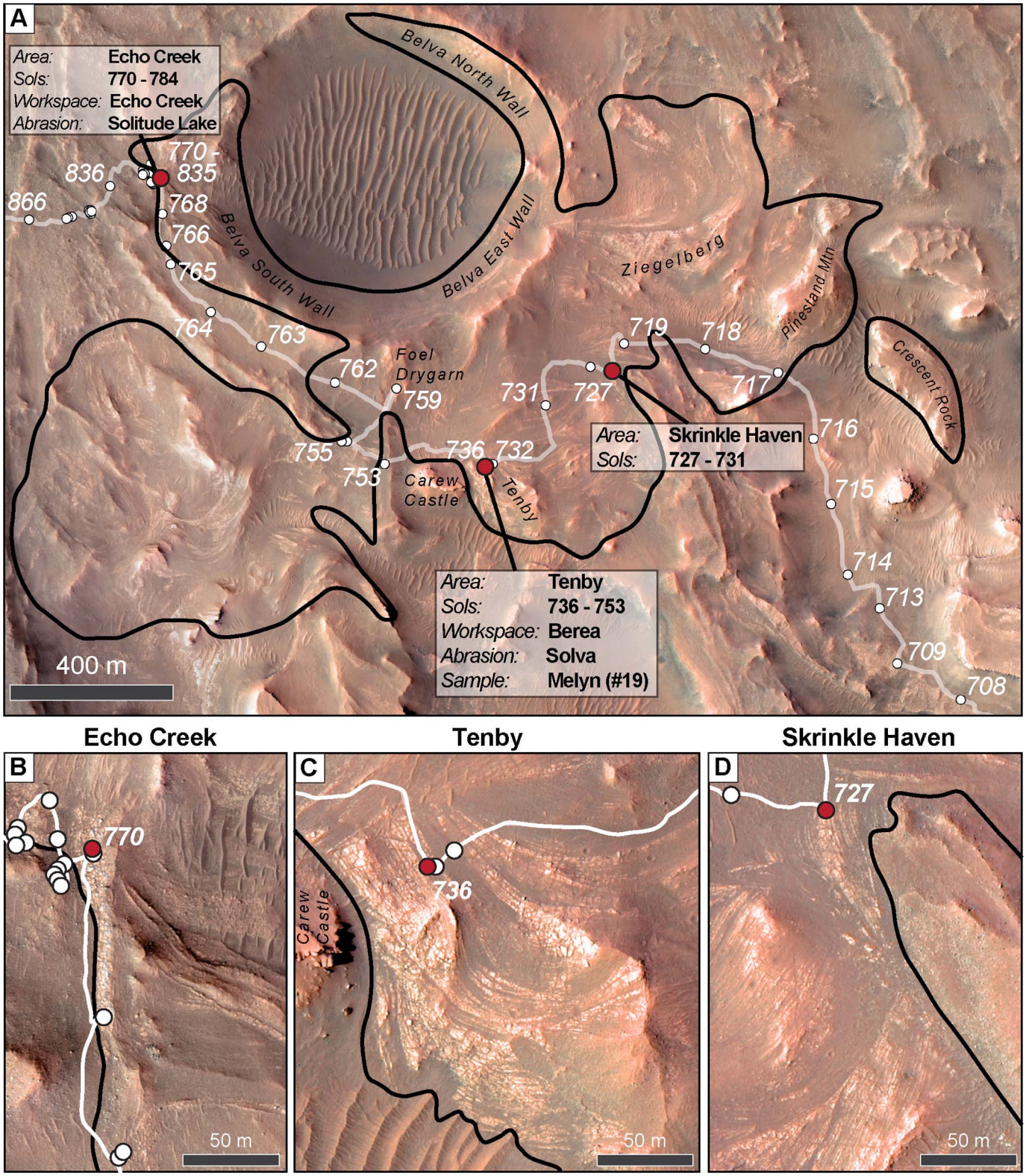

FIG. 2.—**A)** Geographic context for observations of the Skrinkle Haven member made by the *Perseverance* rover between mission sols 715 and 835 on a High Resolution Imaging Science Experiment (HiRISE) false-color orthophoto mosaic basemap (Fergason et al. 2020) (Table S3). The thick black line delineates the outcrop extent of the Skrinkle Haven mbr. Black, italic labels indicate named parts of outcrop area referred to in the text. The white line shows *Perseverance's* traverse across the study area. White and red circles along the traverse mark end-of-sol parking locations of the rover, and the adjacent white numbers are the first sol the rover was parked at that location. Red dots are parking locations where significant, proximal observations were made of the Skrinkle Haven mbr at **B)** Echo Creek, **C)** Tenby, and **D)** Skrinkle Haven. At the Tenby and Solva locations, *Perseverance* abraded and conducted proximity science using the instruments on the rover's arm. The Melyn drill core was collected by *Perseverance* at the Tenby location.

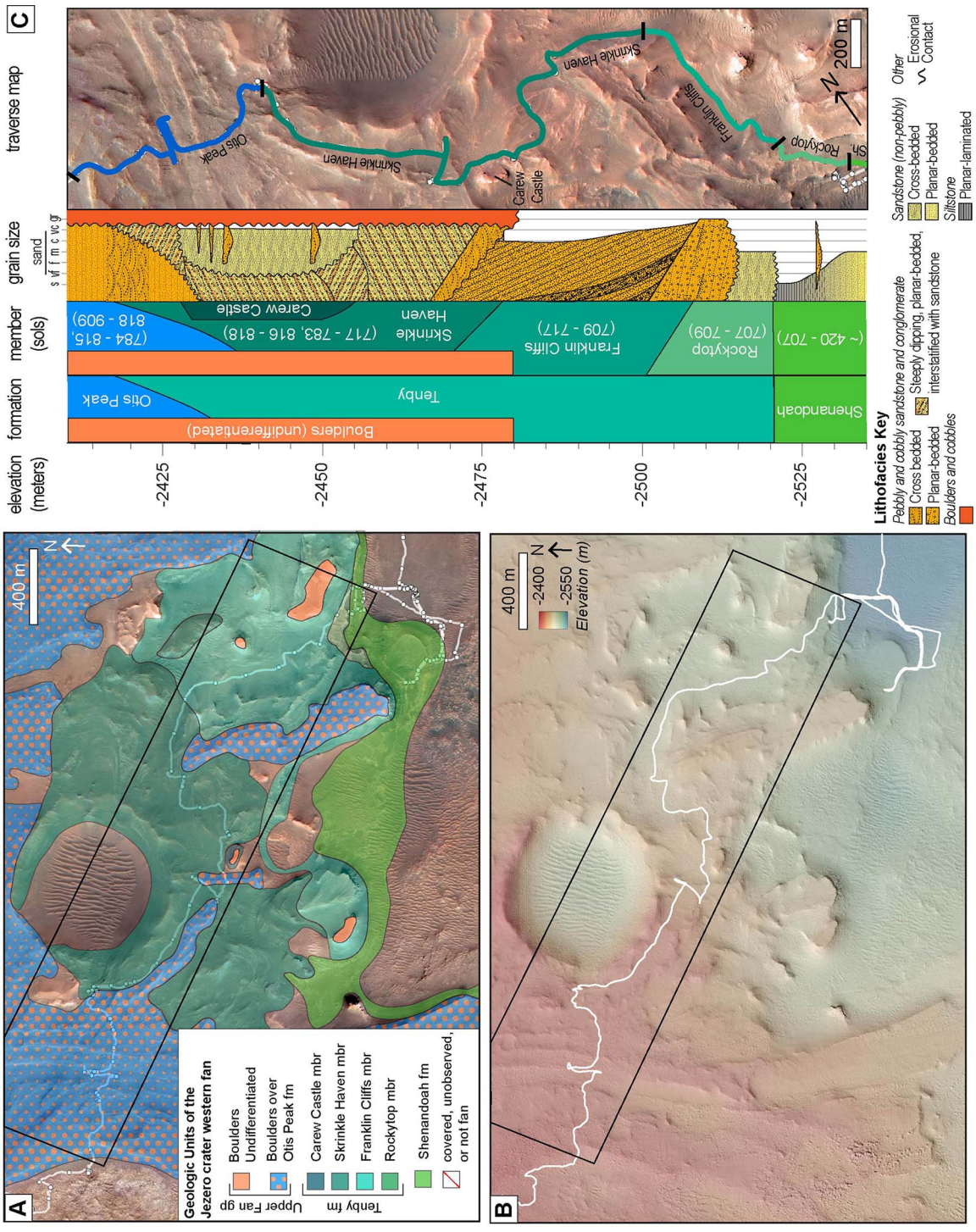

FIG. 3.—Geologic and stratigraphic context of the Skrinkle Haven mbr in the Jezero Crater western fan. **A)** Geologic map of the Jezero Crater western fan observed along *Perseverance's* traverse. The basemap is a false color orthophoto mosaic compiled from HiRISE (Fergason et al. 2020) (Table 1). The white line indicates the rover's traverse across the area from southeast to northwest. White dots indicate parking locations of the rover. The black rectangle shows the extent of the map inset in Part C. **B)** HiRISE-derived digital model and hillshade for the same area as in Part A. The white line indicates the rover's traverse across the area. The black rectangle shows the extent of the map inset in Part C. **C)** Synthetic stratigraphic column showing the vertical elevation and present understanding of relationships between sedimentary units of the Jezero Crater western fan that crop out along *Perseverance's* traverse between sols 707 and 909. This column does not account for total stratigraphic thickness or lateral variations in elevations and thicknesses. On the inset map, the line indicating the rover's traverse has been color-coded to correspond to the formation or member it was driving on at that time.

TABLE 1.—*Description of data sources and their application in this study.*

Data Source					Data Product						Analysis and Results		
									Observable Scale				
Spacecraft	Instrument		Data Source	Instrument Description	Data Product	Processing Methods	Pixel Size	Figures	Min	Max	Analysis	Physical Parameter	Relevant Figures
Perseverance	SHERLOC	ACI	(Beegle and Bhartia 2021)	(Bhartia et al. 2021)	Colorized, focus-merged (mosaic) image	(Sharma et al. 2024)	10.1 µm	8A, E	µm	mm	Point Count (0.5 mm × 0.5 mm grid)	Percent abundance of clastic grains, cements, and voids	8
		WATSON			Image			4D, G			N/A	Grain Size Grain Sorting	
	Mastcam-Z		(Bell and Maki 2021)	(Bell et al. 2021)	Image mosaic	(St. Clair et al. 2022)	Variable	4B, C, E, F, 5A, B, 7A–C, 9A, 9B–D, 10A, C	mm–cm	m–km	Facies descriptions	Color, stratification, sedimentary structures, grain size, grain sorting	7, 9, 10
	SuperCam	RMI	(Wiens and Maurice 2021)	(Wiens et al. 2020; Gasnault et al. 2021; Maurice et al. 2021)	Image mosaic	(Le Mouélic et al. 2024)	Variable	10B, D	mm –cm	m–km			10
	RIMFAX		(Hamran and Paige 2021)	(Hamran et al. 2020; Hamran and Paige 2021)	Radargram	(Hamran et al. 2020)	N/A	14A, B	cm–m	m	Cross sections	Relative time order or architectural elements	14
Mars Reconnaisance Orbiter (MRO)	High Resolution Imagine Experiment (HiRISE)		Fergason et al. (2020)	McEwen et al. (2007)	False color mosaic image of Jezero crater	Fergason et al. (2020)	1 m	1D, 2A–D, 3A, C, 4A, 5C, 6, 12A	m	km	Trace bedding sets	Distribution of curvilinear bedsets in the Skrinkle Haven mbr	6
												Delineate curvilinear set areas	12
											Thickness of dark toned and light toned rock intervals	Bedset thickness	5
					DTM of Jezero crater			3B, 13A–D			Fitting planes to bed set traces	Dip direction of bedsets	12
											Elevation spatial statistics of curvilinear sets	Mean elevation, elevation range, apparent height, etc. (Table S7)	12, 13
											Cross sections	Relative time order or architectural elements	13, 15

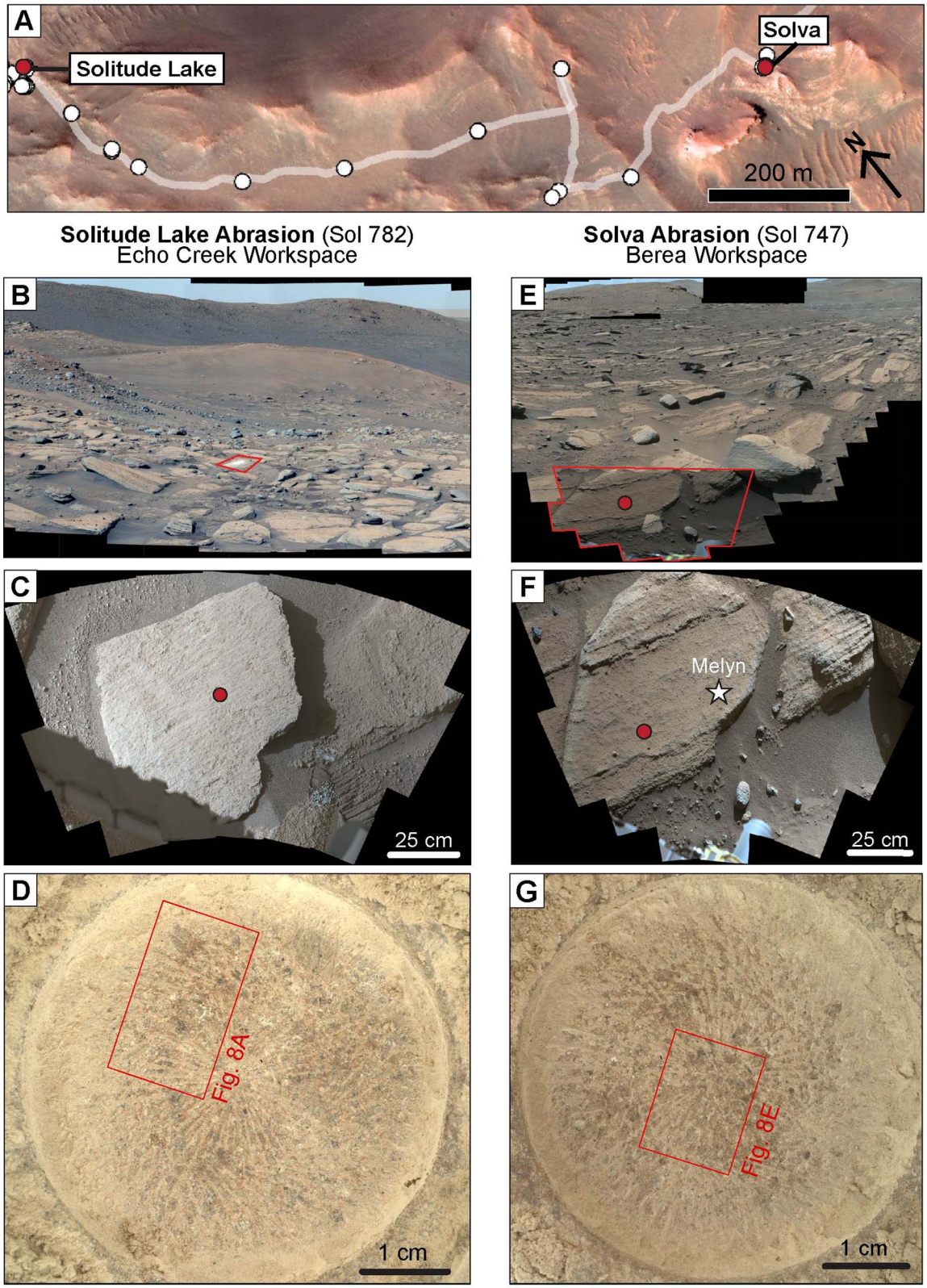

FIG. 4.—The Solitude Lake (Parts B, C, D) and Solva (Parts E, F, G) abrasion patches that were used to measure the grain-size distribution of Facies 1 (F1). **A)** Map showing the locations of the abrasion patches. The basemap is a false color orthophoto mosaic compiled from HiRISE observations (Fergason et al. 2020). The white, translucent line is the *Perseverance* rover traverse, and the white dots along the traverse are rover parking locations, as in Figure 2. **B)** Mastcam-Z 110 mm mosaic looking toward north at the Echo Creek workspace on sol 792 (rover sequence zcam08817). The Belva crater south wall is also visible in the foreground and the north wall in the background. The red box indicates the location of Part C. **C)** Mastcam-Z 110 mm mosaic looking down at the Echo Creek workspace before abrasion (Sol 775 z08795).

(Fig. 5A). Beds of the Skrinkle Haven mbr are difficult to trace laterally for more than a few meters at the outcrop scale since outcrop quality is variable (Fig. 5A). Bedsets, the second-order architectural element, are composed of multiple beds of the same lithofacies (Fig. 5A, B). Bedsets are easily traced at the outcrop and orbital scale (Fig. 5B, C). The bedsets of the Skrinkle Haven mbr are organized into curvilinear sets, third-order stratigraphic architectural elements in which the planes of the constituent bedsets are parallel to and congruent with one another (Figs. 5C, 6).

Geospatial analyses were conducted on Skrinkle Haven mbr geometries visible in orbiter data to determine their geometric characteristics. QGIS (QGIS.org 2024) and a HiRISE image mosaic (Fergason et al. 2020) were used to trace the geometry and spatial distribution of bedsets in the Skrinkle Haven mbr as a line shapefile (Fig. 6; File S5). Parallel, congruent bedsets were then grouped into curvilinear sets. A polygon was traced around the exterior of each curvilinear set, and each was given a nondescriptive alpha name code (e.g., A, BB, CCC, etc.; Fig. 6; File S6). Where available, rover images were used to assist in the delineation of both spatial data sets. The python packages GeoPandas (Jordahl et al. 2020), Rasterio (Gilles 2024), and rasterstats (Perry 2024) were used to analyze the characteristics of the HiRISE DTM in each curvilinear set (File S8). Extracted characteristics for each curvilinear set polygon include shape parameters (length, width, area) and elevation statistics including mean, median, minimum, and maximum elevation as well as amplitude (apparent height), which is the 90th percentile (P_{90}) elevation less the 10th percentile (P_{10}) elevation in any given polygon (Tables 1, S7).

Dip magnitude and dip direction of strata in the Skrinkle Haven mbr were estimated using HiRISE DTMs. The orientations of traced bedsets for the entire Skrinkle Haven mbr were estimated by assigning elevation values from the HiRISE DTM to each trace (making each line three-dimensional) and then applying a method of plane fitting to each bed set trace adapted from (Quinn and Ehlmann (2019); Supplementary File S5). The circular mean dip direction and standard deviation of the fitted planes were used to characterize the dip direction and spread of each curvilinear set. These measurements were enabled by the irregular surface at the top of the Jezero Crater western fan, in which curvilinear sets often crop out over a topographic surface with tens of meters of relief (Fig. 3B).

The characteristics of bedsets and curvilinear sets were also assessed in six cross sectional transects across the Skrinkle Haven mbr (Fig. 6). The mapped bedset traces were used along with the HiRISE DTM to construct the cross sections.

The arrangement of bedsets in the cross sections was used to assess stacking patterns in curvilinear sets. The stacking pattern of each curvilinear set was classified as being primarily prograding, aggrading, or retrograding, based on the orientation of constituent bedsets derived from cross sections, Wheeler diagrams, and estimated dip direction (Table S7). Curvilinear sets were classified as prograding if their bedsets appeared to have a growth direction towards the south to northeast (basinward; away from the Neretva Vallis channel) and retrograding if they appeared to have a growth direction towards the north to southwest (toward the Neretva Vallis Channel). Curvilinear sets were classified as aggrading if the vertical growth of the strata was more pronounced than either its basinward or anti-basinward growth.

Then, the relative stratigraphic order of the curvilinear sets was determined using HiRISE images, the HiRISE DTM, Mastcam-Z images and image mosaics, and RIMFAX observations. Using these data, Wheeler diagrams (Wheeler 1964; Qayyum et al. 2017) were constructed along the same transects as the cross sections.

Where possible, the nature of the lower bounding surfaces of the curvilinear sets were determined using plan view, outcrop, and cross-section observations. The lower bounding surface of each curvilinear set was described as either erosional, non-erosional, or unknown (Table S7). The lower bounding surface of a curvilinear set was considered erosional if the bedsets in a younger curvilinear set truncate the bedsets of an older curvilinear set in plan view (Fig. 6) and the younger set is at the same or a lower elevation (i.e., the younger set is not overlying the older set). If no erosional truncation of the older set could be observed at a contact, the stratigraphic termination type (e.g., downlapping) of the younger curvilinear set was assessed either from outcrop images or inferred from cross sections. If neither the erosional state nor the stratigraphic termination of a curvilinear set's lower bounding surface could be discerned, the lower bounding surface was classified as unknown.

Defining Sequence Stratigraphic Components and Surfaces.—A sequence stratigraphic approach was applied to the curvilinear sets of the Skrinkle Haven mbr to understand the time–space relationships of strata and their relationship to relative lake level (Table 2). In the case of the Skrinkle Haven mbr, the relative age of its curvilinear sets can be inferred only through their stacking order. For this analysis, curvilinear sets were considered to be architectural elements—groups of sedimentary bodies that share common facies associations, geometries, stacking patterns, and bounding surfaces (Table 2) (Pickering et al. 1995). Cross sections, architectural element stacking patterns, RIMFAX radargrams, and rover images were all incorporated into the interpretation of the relative ages of the stacked curvilinear sets. Since the Skrinkle Haven mbr was most likely deposited through downstream-accreting grain flows, we assume that the bedsets in each curvilinear set young in the dip direction. To illustrate the relationship between curvilinear sets in time and space, Wheeler diagrams (Wheeler 1964; Qayyum et al. 2017) were constructed along each cross section. The duration of unitless time assigned to each curvilinear set was selected purely to illustrate trends on the Wheeler diagrams. While determining the relative ages of curvilinear sets in a single cross section is a straightforward exercise, only a handful of curvilinear sets serve as tie points between cross sections.

A sequence stratigraphic approach can be applied in lacustrine settings to understand how the deposition of clastic sequences is affected by changes in relative lake level on short (< 1–1000 year) timescales (e.g., Moran et al. 2023; Zavala et al. 2024). Systems tracts are defined as successive curvilinear sets with the same stacking pattern type and general growth direction that are not separated by major unconformities (Table 2). Following the preferred nomenclature for lacustrine systems, systems tracts are either transgressive or regressive (Embry and Johannessen 2017; Zavala et al. 2024). A transgressive systems tract (TST) is defined by an underlying maximum regressive surface (MRS) and an overlying maximum flooding surface (MFS) (Van Wagoner et al. 1988; Embry and Johannessen 2017). A regressive system tract (RST) is defined by the inverse relationships with MRS and MFS (Embry and Johannessen 2017). An MFS is a stratigraphic surface that marks a maximum relative lake level and the correlative paleolake floor at the end of a transgression (Catuneanu 2015; Zavala et al. 2024). In the Skrinkle Haven mbr, MFSs are defined by the base of the youngest architectural element in a regressive trend on the Wheeler diagram. An MRS is a stratigraphic surface that marks the change from shoreline transgression to shoreline

←

The red dot marks the location of the abrasion patch. **D)** WATSON 10 cm standoff of the Solitude Lake abrasion patch acquired on sol 781. The red box indicates the extent of Figure 8A, the higher-resolution ACI image on which point counts were conducted. **E)** Part of a Mastcam-Z 110 mm mosaic of the Berea Workspace and Tenby outcrop area acquired between sols 736 and 739 during rover sequences zcam08745, zcam08746, zcam08747, zcam0848, zcam08749, and zcam08750. The red box shows the extent of image 4F, and the red dot shows the location of the Solva abrasion patch. **F)** Mastcam-Z 0 mm mosaic looking down at the Berea Workspace acquired on sol 736 before abrasion or coring activities (zcam08745). The red dot indicates the location of the Solva abrasion patch, and the white star indicates the location where the Melyn core was collected. **G)** WATSON 10 cm standoff of the Solva abrasion patch acquired on sol 744. The red box indicates the extent of Figure 8E, the higher-resolution image on which point counts were conducted.

TABLE 2.—*Description of sequence stratigraphic components.*

Sequence Stratigraphic Component	Definition and Purpose	Definition Sources	Skrinkle Haven Mbr Definition
Architectural Elements	A group of sedimentary bodies that share common facies associations, geometries, common bounding surfaces.	Pickering et al. 1995	Curvilinear sets; groups of conformable bedsets. Architectural elements may be dominantly **progradational, aggradational, or retrogradational.**
Systems Tract	A linkage of contemporaneous depositional systems that represents a specific sedimentary response to the interaction between sediment flux, physiography, environmental energy, and changes in accommodation.	Brown and Fisher 1977; Posamentier and Allen 1999; Catuneanu 2022; Zavala et al. 2024	Successive curvilinear sets with the same stacking-pattern type and general progradation direction that are not separated by major unconformities. Boundaries between systems tracts are either maximum regressive surfaces or maximum flooding surfaces. Systems tracts may be **transgressive** or **regressive.**
Maximum Regressive Surface	A stratigraphic surface that marks the change from shoreline transgression to shoreline regression.	Catuneanu 2022	Base of the youngest architectural element in a regressive trend on the Wheeler diagram.
Maximum Flooding Surface	A stratigraphic surface that marks a maximum relative lake level, and its correlative surface (i.e., the paleo-lake floor at the end of transgression).	Catuneanu 2015; Zavala et al. 2024	Base of the youngest architectural element in a transgressive trend on the Wheeler diagram.
Sequence (genetic)	Groups of systems tracts bounded by maximum-flooding surfaces; a genetic stratigraphic sequence records a "depositional episode" where the maximum-flooding surface marks a significant change in the distribution of depocenters and sediment dispersal.	Galloway 1989; Zecchin and Catuneanu 2013; Catuneanu 2022; Zavala et al. 2024	A group of systems tracts that share upper and lower maximum flooding surfaces.

regression (Table 2). This transition occurs during relative-lake-level rise, when the rate of the rise outpaces sedimentation rates (Catuneanu 2022). In the Skrinkle Haven mbr, an MRS is defined by the base of the youngest architectural element in a transgressive trend on the Wheeler diagram.

Sequences in the Skrinkle Haven mbr are defined systems tracts bounded by MFSs, usually with one RST and one TST (Table 2) (Galloway 1989; Zecchin and Catuneanu 2013; Catuneanu 2022; Zavala et al. 2024). Once sequences were defined, interpretations were made about relative lake levels during deposition of the Skrinkle Haven mbr and lake basin dynamics (Bohacs et al. 2000; Zavala et al. 2024).

SEDIMENTOLOGY AND STRATIGRAPHY OF THE SKRINKLE HAVEN MBR (TENBY FM)

Lithofacies

Facies 1 Description: Fine-Grained Sandstone.—Facies 1 (F1) is a fine-grained sandstone (Figs. 5, 7, 8; Table 3). This facies is relatively resistant to weathering (Fig. 5A) and has a relatively light-toned weathering color. The upper and lower contacts of F1 with Facies 2 (F2) are sharp, planar, and parallel to internal stratification (Fig. 5A, B). Contacts between sets of F1 and F2 have steep dips up to ~ 35° (Figs. 5A, B, 9, 10). Some upper contacts with F2 have minor, mm- to cm-scale scour (Fig. 10A). Bedsets of F1 range in thickness from ~ 0.2 m to ~ 10 m, with the most common thicknesses being between 0.5 and 1.0 m. Bedsets of this facies are often laterally continuous within a curvilinear set, and are visible both in outcrop (Fig. 5A, B), and in orbital images (Figs. 2, 5C, 6). In HiRISE images and image mosaics collected by Mastcam-Z and SuperCam, sets of F1 can be reliably traced 4–12 m across modern surface topography, terminating only at the contact with an adjacent curvilinear set (Figs. 5C, 6, 9).

F1 appears to be composed of thin (3–10 cm thick), planar parallel beds (Fig. 7). Resolvable grain-size does not noticeably change between adjacent beds or laminae (Figs. 4, 5, 7). No resolvable grain size trends (e.g., fining upward, coarsening upward, grading) are observed in beds, bedsets, or curvilinear sets (Fig. 7). All internal stratal surfaces dip parallel to the high depositional dips of up to ~ 35° between the bedsets (Figs. 7, 9). While bedset boundaries can be traced laterally in outcrop for tens of meters due to erosional difference, internal stratification is difficult to follow in outcrop images (Figs. 5, 7).

Point counts of the Solitude Lake and Solva abrasion patches indicate that F1 is a moderately sorted to moderately well sorted, upper-fine-grained sandstone (Fig. 8; Supplementary Table S4). In both abrasion patches, measured grain sizes range from ~ 1 mm to below the resolution of the WATSON ACI imager (~ 0.03 mm) (Fig. 8A, E). The most common grain-size class in both assessments is fine sand, although this is likely a slight underestimate of grain-size due to the 2-D nature of the studied area (Fig. 8C, G). Grains in the Solva abrasion patch are composed primarily of olivine, pyroxene, and feldspar (Farley and Stack 2024a). Mastcam-Z and SuperCam observations show that this facies produces spectra consistent with an ultramafic composition and Fe-bearing carbonate in outcrop (Dehouck et al. 2024; Farley and Stack 2024a; Núñez et al. 2024). Point counts show that ~ 80% of the area of the Solva and Solitude Lake abrasion patches are detrital grains and ~ 20% is intergranular cement (Fig. 8; Table S4). No intragranular cement (cement in clastic grains) or voids were observed. A primary porosity of ~ 20% is consistent with fine-grained, moderately sorted sandstone observed on Earth (Hough 1969). There are two colors of cement present in both abrasion patches: bright white and tan (yellow-red) (Fig. 8A, E). No assessment was made of the relative abundance or void-filling character of these different cement types.

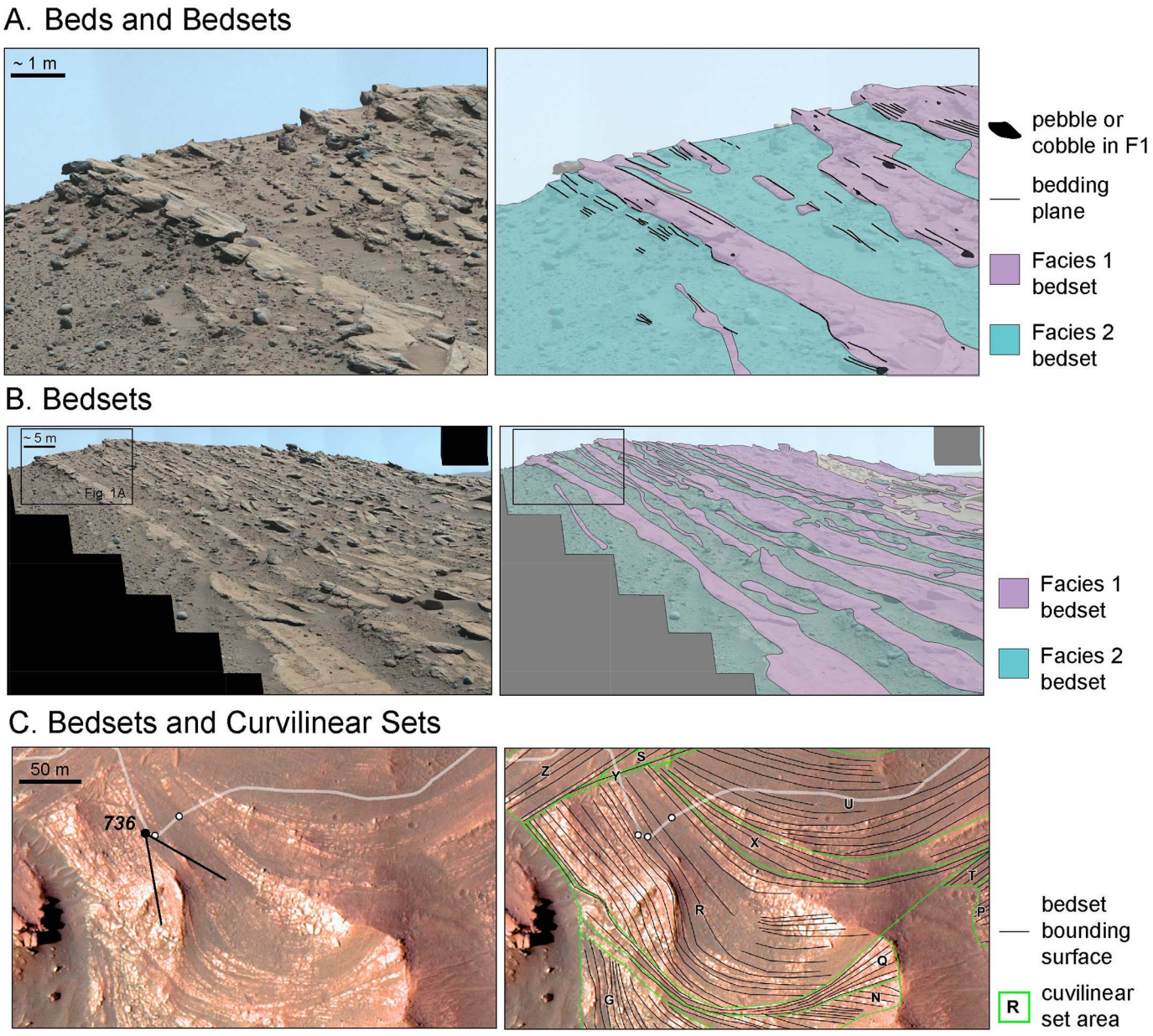

FIG. 5.—Hierarchy of sedimentary architectural elements of the Skrinkle Haven mbr referred to in this study, beds (first order), bedsets (second order), and curvilinear sets (third order), using curvilinear set R as an example. **A)** Meter-scale example of how beds and bedsets of Facies 1 (FA1) and Facies 2 (FA2) appear in outcrop (Mastcam-Z Sol 739 8750). **B)** A wider-field-of-view version of Part A that illustrates how bedsets appear in outcrop at the 5–10 m scale. The inset shows the location of Part A in this image. **C)** Bedsets and curvilinear sets annotated on a HiRISE basemap (Fergason et al. 2020) (Table S3). The images in Parts A and B show portions a Mastcam-Z 110 mm mosaic acquired from the sol 736 parking location (Part C) between sols 736 and 739 during rover sequences zcam08745, zcam08746, zcam08747, zcam0848, zcam08749, and zcam08750.

This facies also contains trace quantities of granules, pebbles, and small cobbles (Figs. 5A, B, 7C). These outsized clasts are typically restricted to individual beds, and the distribution of the beds containing outsized clasts appear somewhat random (Fig. 7C). The distribution of the gravel-size clasts also appear random—the clasts do not appear to occur preferentially along bedding planes, near contacts with F2, or co-occur with a change in average grain-size. Outsized clasts tend to be dark-gray or black with a smooth, aphanitic texture, and have Mastcam-Z spectra consistent with olivine and low-calcium pyroxene (Kildaras et al. 2024).

Facies 2 Description: Conglomerate.—F2 is a dark-toned, recessively weathering, pebble to cobble conglomerate (Figs. 5A, B, 10; Table 3). The recessive, crumbly, weathered appearance of this facies made rover observations difficult. Coherent outcrops are rare, spatially limited, and generally of poor quality.

Bedsets of this facies are often interstratified with F1 (Figs. 5A, B, 10C). Contacts between intervals of F1 and F2 have bedding dips of up to ~ 35° (Figs. 5A, B, 9, 10). Lower and upper contacts with facies F1 are sharp and parallel to F1 bed dips (Figs. 5A, B, 9, 10). Some lower contacts of this facies with F1 have minor, mm- to cm-scale scour or erosion (Fig. 10A). Bedsets of facies F2 range in thickness from ~ 0.2 m to ~ 10 m, with the most common thicknesses being between 0.5 and 3.0 m (Figs. 5A, B, 6, 10).

Few sedimentary structures were discernible in facies F2, likely due to poor outcrop quality (Fig. 10). Where outcrops are present, the facies appears

FIG. 6.—Map of the Skrinkle Haven mbr showing bedset traces (narrow black lines) and curvilinear sets (white-bounded polygons) identified from a HiRISE basemap (Fergason et al. 2020) (Table S3). The thick black lines show the transects along which the cross sections and Wheeler diagrams were constructed. The white, translucent line is the *Perseverance* rover traverse, and the white dots along the traverse are rover parking locations, as in Figure 2. Lettered labels (A, AA, etc.) are the names of the curvilinear sets. Shapefiles of the bedset traces and curvilinear set areas are available in Supplementary Materials (S5 and S6).

structureless to crudely stratified and ungraded (Figs. 5A, B, 10). Images of small outcrops of F2 show that this facies is grain-supported with limited pore space and composed predominantly of small pebbles (2–10 mm) with common cobble- and small-boulder-size clasts (Fig. 10). The wide range of grain-sizes in this facies and the apparent limited pore space in outcrops suggest that this conglomerate is variably, but predominantly, poorly sorted. Mastcam-Z and SuperCam observations show that this facies produces spectra consistent with a mafic composition and Fe-bearing carbonate (Dehouck et al. 2024; Núñez et al. 2024).

Facies Interpretations.—The consistency with which F1 and F2 were deposited as conformable, generally steeply dipping strata suggests that the facies share a common depositional setting and mechanism. The steep dips of strata in the Skrinkle Haven mbr are likely depositional because there is no evidence for large-scale deformation of sedimentary rocks in the Jezero Crater western fan. The steep stratal dip angles in the Skrinkle Haven mbr are in the range of the angle of repose (~ 25–45°) of noncohesive sediments (e.g., van Burkalow 1945; Pohlman et al. 2006). The angle of repose for noncohesive granular materials does not change meaningfully for sand-size and larger particles if gravity is less than at Earth's surface (Kleinhans 2004; Nakashima et al. 2011; Elekes and Parteli 2021). Therefore, Skrinkle Haven mbr strata with dips above ~ 25° were deposited at or just under their angle of repose. In sedimentary systems, angle-of-repose deposition occurs on oversteepened slopes where gravity drives sediment movement independent of any fluid-induced stress (Allen 1970).

The dominance of dip-parallel, ungraded beds at or near the angle of repose, and the decided absence of any other sedimentary structures, suggests that the most likely depositional process for both F1and F2 is mass transport via grain flows (Allen 1970; Middleton and Hampton 1973; Talling et al. 2012; Shanmugam 2021). Grain flows may, but do not necessarily, produce inverse grading depending on the effectiveness of kinetic sieving in a particular flow (Kleinhans 2004). Grain-flow processes may have occurred subaerially, as in the slip faces of aeolian dunes (Cornwall et al. 2018a, 2018b) or subaqueously, as in the downstream accretion of fluvial bars (Kleinhans 2004; Herbert et al. 2020) and delta fronts (Nemec 1990; Long and Lowey 2006; Winsemann et al. 2021). Since both F1 and F2 include pebbles and

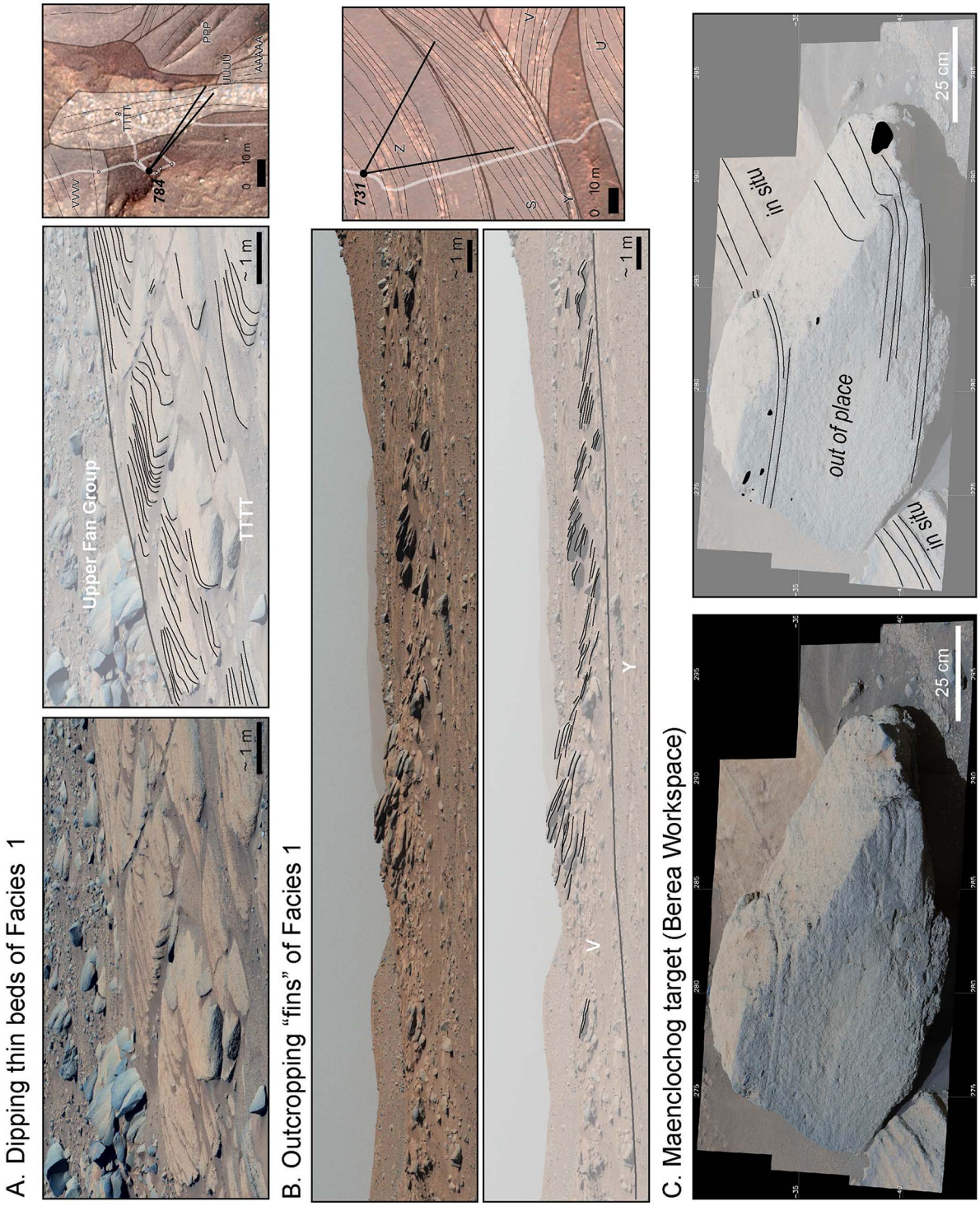

FIG. 7.—Images illustrating the outcrop-scale characteristics of Facies 1 (F1). Lettered labels (A, AA, etc.) are the names of the curvilinear sets. **A)** Thin, steeply dipping beds. The black lines indicate bedding planes, and the labels (e.g., TTTT) identify the curvilinear set and the Otis Peak fm. The image is a part of a 110 mm Mastcam-Z mosaic collected on Sol 792 (zcam08817). The reference maps for Parts A and B show the parking location from which the mosaics were collected and the viewshed represented in the images. The basemap is the same as in Figure 6 (Fergason et al. 2020) (Table S3). **B)** Steeply dipping beds of Facies 1. The black lines on the annotated image indicate bedding planes, and the labels indicate which curvilinear set is in the image (V and Y). The image is a part of a 63 mm Mastcam-Z mosaic collected on Sol 731 (zcam08739, zcam08740). **C)** A rare proximal, vertical exposure of Facies 1 on a slightly displaced rock in the Berea workspace (Maenclochog; Figs. 2, 4E). The numbered grid in the image background shows the azimuth (vertical lines) and declination (horizontal lines) from the perspective of Mastcam-Z. The black lines indicate bedding planes, and the black outlines show the location of outsized pebbles. The image is a 110 mm Mastcam-Z mosaic collected on Sol 745 (zcam08755).

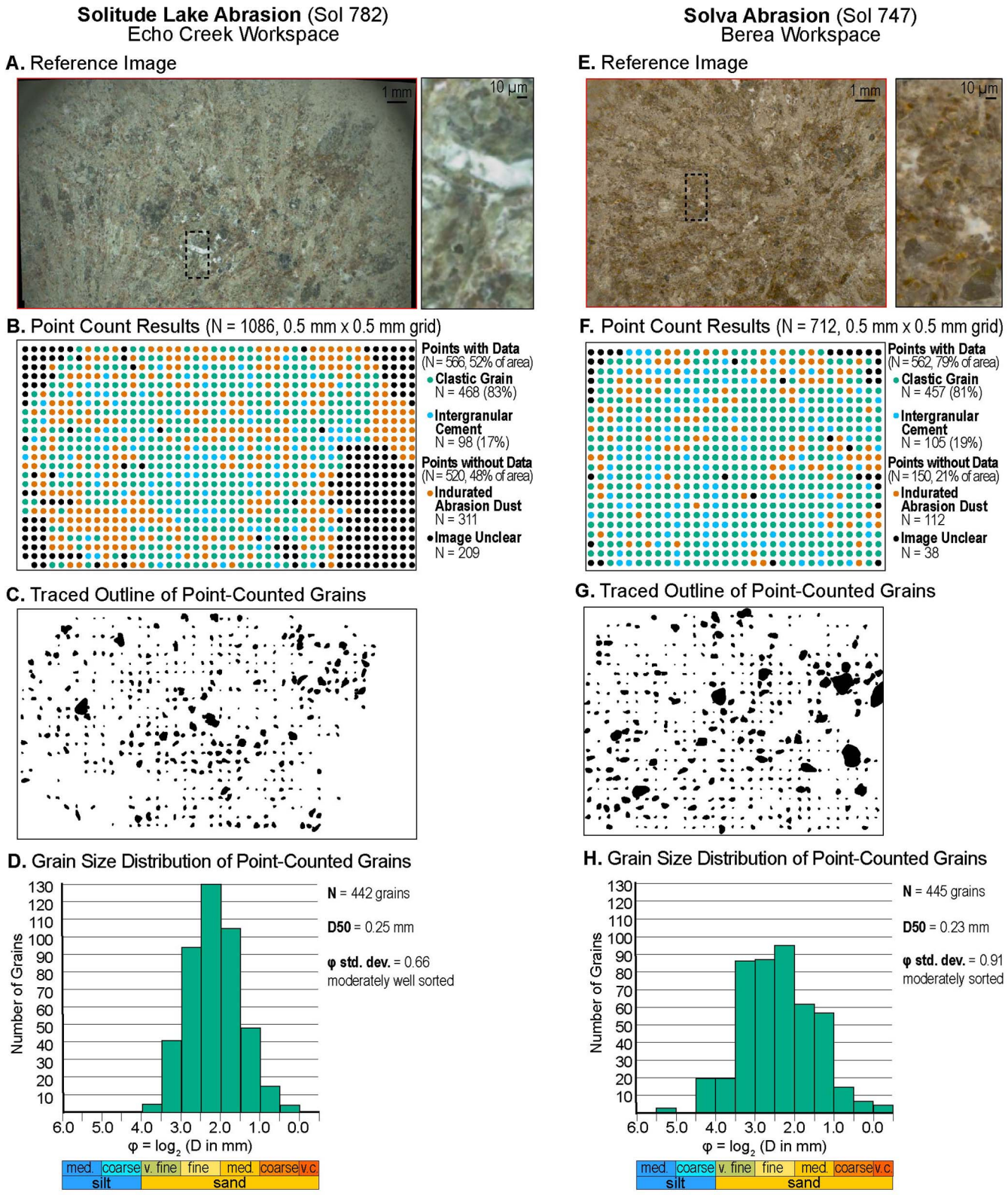

FIG. 8.—Grain-size point counts of the Solitude Lake (Parts A–D) and Solva (Parts E–H) abrasion patches in Facies 1 (F1). **A**, **E)** show the images used for point counting. The dotted black lines on the main images show the extent of the inset images. The Solitude Lake reference (Part A) was collected on Sol 782 and is a colorized SHERLOC ACI mosaic (Solitude_Lake.PSC.0.0675) acquired at nighttime at a 4.8 cm standoff with white LED lights on. The mosaic was colorized using sol 782 daytime, fully shadowed SHERLOC WATSON images. The Solva reference image (Part E) was collected on sol 747 and is a colorized SHERLOC ACI mosaic (Solva_747.PSC.0.0750) acquired at nighttime at a 4.8 cm standoff with white LED lights on. The mosaic was colorized using sol 747 daytime, fully shadowed SHERLOC

TABLE 3.—*Lithofacies.*

Facies Name	Weathered Geomorphic Expression	Grain Size	Sorting	Sedimentary Structures	Diagenetic Effects	Depositional Process Interpretation	References
F1	Resistant	Upper fine sand	Moderate to moderately well	Structureless, ungraded thin beds and thick laminae	Fe-carbonate cement; sulfate cement	Grain flow (subaqueous)	Allen 1970; Talling et al. 2012
F2	Recessive	Pebble conglomerate	Poor	Structureless thin to thick beds	Unknown, likely poorly cemented	Grain flow (subaqueous)	Allen 1970; Talling et al. 2012

cobble-size clasts, which are unlikely to have been transported by Martian winds (Preston et al. 2024), deposition of the Skrinkle Haven mbr is interpreted to have occurred subaqueously.

If both facies F1 and F2 were deposited by the same process and in the same setting, what is the depositional relationship between them? There are no resolvable fining-up or coarsening-up trends within beds, bedsets, or curvilinear sets observed in either facies F1 or F2. Additionally, while alternations between F1 and F2 are common, the range of bedset thicknesses (0.1–10 m) suggests that switching occurred frequently but without any apparent regularity. Therefore, the sharp contacts between facies and the lack of grading suggest that the deposition of the two facies did not occur as part of the same depositional event, as might occur in hybrid event beds (e.g., Dodd et al. 2022). Instead, the differences between fine-sand-dominated and pebble-dominated elements are likely to have been a function of discontinuous sediment supply and/or irregular flood events. Alternatively, the variation in grain-size could be related to the inherent "patchiness" of gravel-bed rivers, where the coarser and finer components of the bedload naturally become segregated (Paola and Seal 1995; Laronne et al. 2001), or result from the grain-size segregation that can occur at a delta brink point, where sediments of different grain-sizes fall out of suspension at different rates and therefore distances downstream (e.g., Kleinhans 2005).

In summary, Skrinkle Haven mbr sediments were deposited as a series of subaqueous grain flows initiated by oversteepened slopes. These slopes were oversteepened by the delivery of sediment to relatively deep water (a brink point) by fluvial transport. Therefore, the sedimentary bodies in the Skrinkle Haven mbr most likely accumulated through downstream accretion. Downstream-accreting grain flows can occur during the building of:

- mid-channel or bank-attached fluvial bars (Bridge and Lunt 2006; Reesink and Bridge 2011; Herbert et al. 2020; Korus et al. 2020),
- fluvial bars created during megaflood events (Baker and Bunker 1985; Carling et al. 2016),
- delta mouth bars (van Yperen et al. 2020; Cole et al. 2021; Winsemann et al. 2021), and
- delta foresets (Nemec 1990; Mortimer et al. 2005; Mikes and Geel 2006; Gobo et al. 2015) (Fig. 11).

Though not conclusive, the lack of current-transport bedforms in the Skrinkle Haven mbr, such as cross-stratification, makes a deltaic setting overall more likely than a fluvial setting, because their absence implies that these strata were not deposited as bar-top deposits, upstream accretion surfaces, and/or lateral-accretion surfaces.

Sedimentary Architecture

The lithofacies interpretations lead to the hypotheses that the Skrinkle Haven mbr was deposited as subaqueous grain flows that accreted downstream in either fluvial bars, delta foresets, or delta mouth bars (Fig. 11). Differentiating between a fluvial setting and a deltaic setting is important since those scenarios have different implications for relative lake levels during deposition and therefore different paleolacustrine histories of Jezero Crater. We use a detailed characterization of sedimentary architecture, including size, amplitude, dip direction, stacking pattern, and relative age, to distinguish between fluvial bar, megaflood fluvial bar, delta mouth bar, and delta foreset hypotheses (Fig. 11).

Observations of Architectural Elements.—The physical characteristics of the curvilinear sets and their constituent bedsets in the Skrinkle Haven mbr are variable (Fig. 12; Table S7). The amplitudes (apparent heights) of curvilinear sets determined from the HiRISE DTM and in cross section projections (Fig. 13) ranges from 0.73 m to 27 m with a mean of 8.5 m (Fig. 12C). There is no clear relation between the elevation of a curvilinear set and its other physical characteristics (Fig. 12C). Curvilinear-set plan view areas range from 145 m^2 to 61576 m^2 (Fig. 12D). There is a positive correlation between the apparent height of curvilinear sets and their plan view area, with larger sets exhibiting higher amplitudes (Fig. 12D). Although the modern surface erosion of the Jezero Crater western fan features tens of meters of topographic relief (Fig. 3B), which likely affects the relationship between apparent height and plan-view area, the positive correlation between the area of curvilinear sets and their amplitude across several orders of magnitude indicates that larger surface areas of curvilinear sets do correspond to larger amplitudes (Fig. 12D).

When aggregated, the mean dip direction of all measured bedset dips, not grouped by curvilinear sets, is toward 165° (± 63°), which agrees with the apparent accretion directions toward southeast in orbiter observations (Fig. 12E). When dip directions are grouped by curvilinear sets (Fig. 12B–D), curvilinear sets less than 10 m tall are responsible for most dip directions not toward the southeast and sets greater than 10 m tall tend to show mean dip directions clustered near the mean (Fig. 12B).

Most of the curvilinear sets (N = 83) show progradational stacking patterns (Figs. 12, 13; Table S7). These progradational curvilinear sets are more likely to have amplitudes > 10 m (Fig. 12). Sets with dominantly aggradational stacking patterns are less common (N = 17), and are about equally divided between those that are solely aggradational (N = 5) and those that have minor progradational (N = 7) or retrogradational (N = 5) components (Table S7). Aggradational stacking patterns are observed in

←
WATSON images. In both images, the tan cement is likely carbonate and the bright white cement is likely sulfate (Phua et al. 2024). **B**, **F)** show the point count results. **C**, **G)** show traces made of clastic grains that were included in the point count. These traces were used to calculate the **D**, **H)** grain-size distributions. Like any two-dimensional grain-size analysis, the average size of individual grains is likely underestimated.

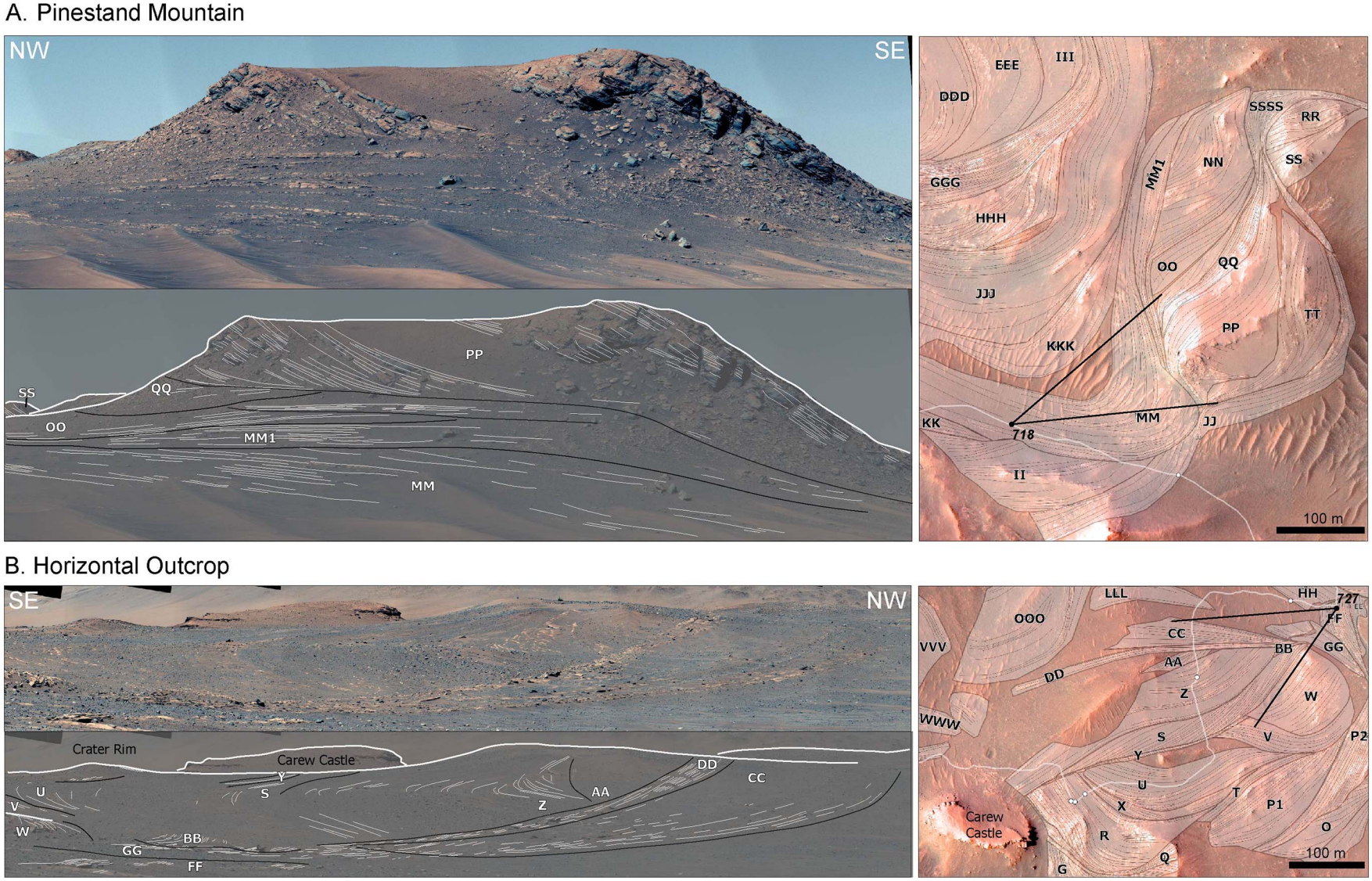

FIG. 9.—Mastcam-Z landscape mosaics illustrating how Skrinkle Haven mbr strata crop out and correspond to orbiter images. Annotations on the Mastcam-Z mosaics include: thin white lines indicating visible bedding planes, thick black lines showing inferred contacts between curvilinear sets, thick white lines indicating modern surface, bold white text indicating curvilinear set names (MMM, W, etc.), and normal white text indicating the orientation of each image. Annotations on the orbiter images include: thin black lines indicating visible bedding planes, translucent white areas showing curvilinear set areas, bold black text indicating curvilinear set names, a black dot with a number showing the location from which the image was collected and the sol of the parking location, and black lines indicating the orientation and field of view of the image mosaic. The orbiter maps of bedsets and curvilinear sets are the same as in Figure 6 (Fergason et al. 2020) (Table S3). **A)** Vertical outcrop of the Skrinkle Haven mbr in Pinestand Mountain. This image is a part of a 110 mm Mastcam-Z image mosaic collected on sol 718 (zcam08726). **B)** Horizontal outcrop across the rolling modern topography of the Skrinkle Haven mbr. This image is a part of a 110 mm Mastcam-Z image mosaic (zcam08726). **C**, **D)** Parts of the same 110 mm Mastcam-Z image mosaic of Belva Crater collected on sol 772 (zcam08789).

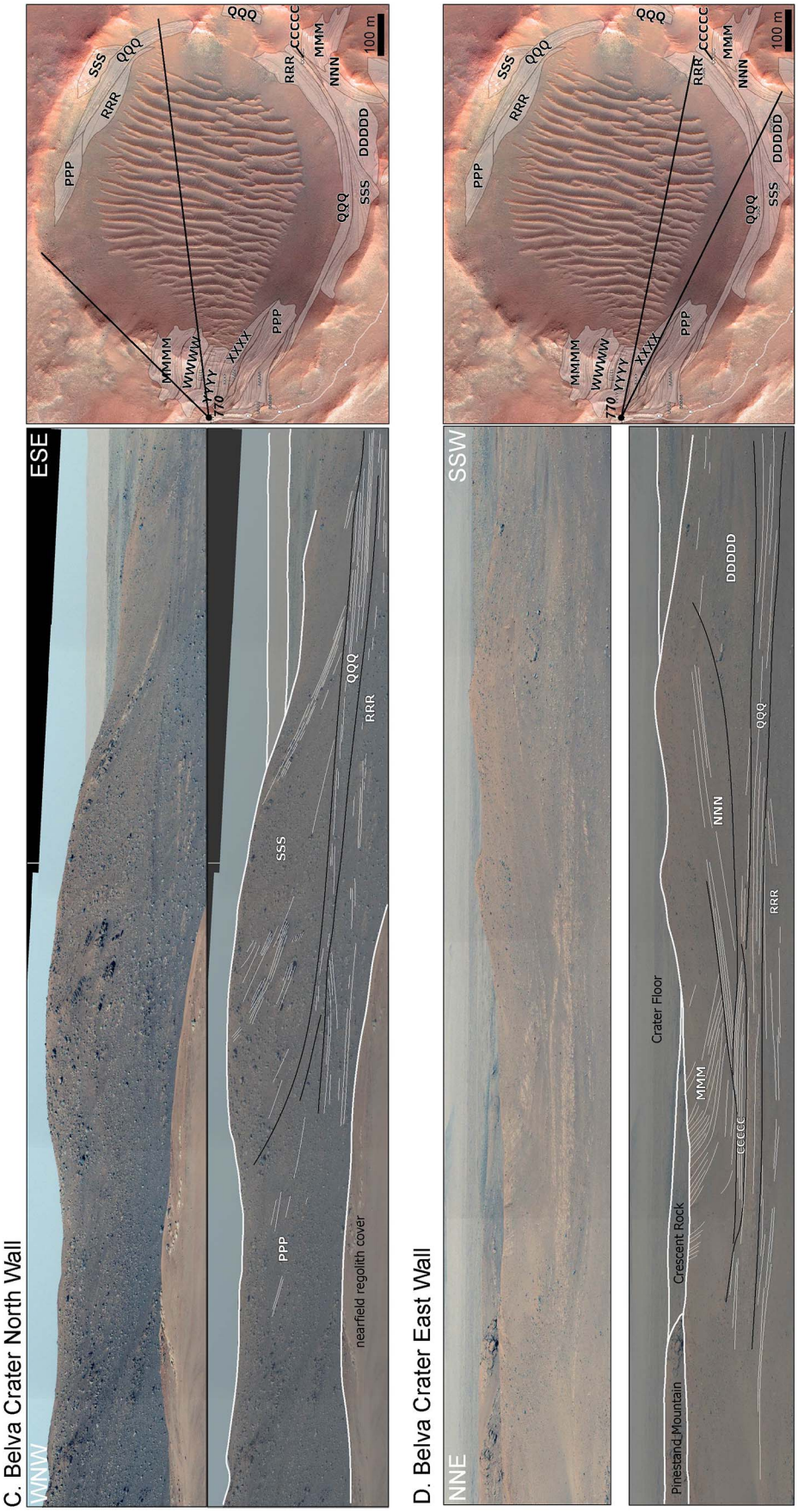

FIG. 9.—Continued.

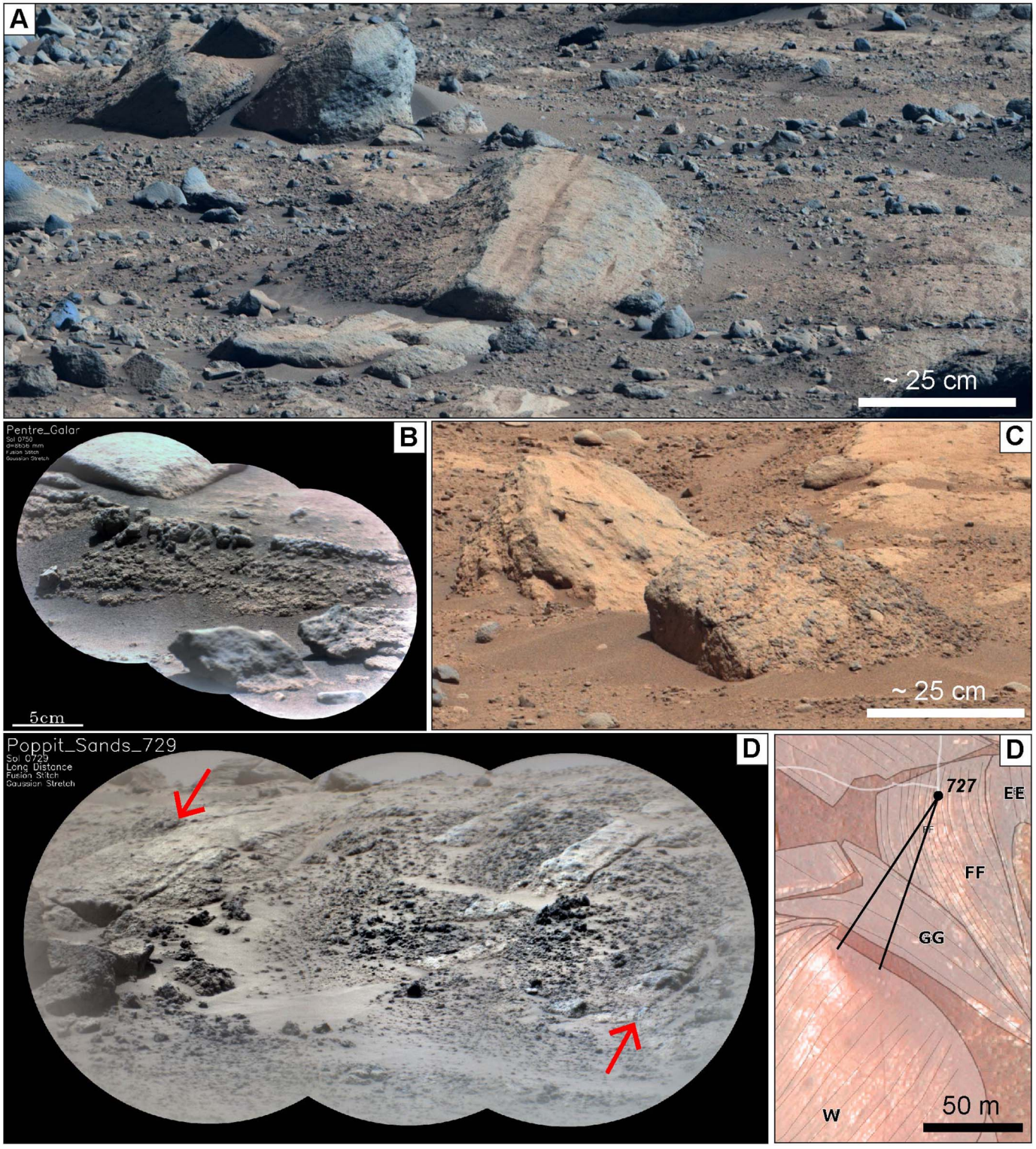

FIG. 10.—Images showing rare outcrops of Facies 2 (F2). **A)** Part of a 63 mm and 110 mm Mastcam-Z mosaic acquired on Sols 721, 727, and 729 (zcam08734, zcam08736, and zcam08738) showing *in situ* Facies 2 strata overlying a sharp, lightly scoured lower contact with Facies 1. **B)** SuperCam RMI mosaic of a small Facies 2 outcrop acquired on sol 750 (scam01750, target: Pentre_Galar). **C)** Part of a 110 mm Mastcam-Z mosaic collected on sol 736 (zcam08744) showing a displaced block of Facies 2. **D)** SuperCam RMI mosaic (scam01729, target: Poppit_Sands_729) acquired on sol 729 of Facies 2 interstratified with thinner intervals of Facies 1 in curvilinear set W. The red arrows point to some possible *in situ* boulders. On the map thin black lines indicate visible bedding planes, translucent white areas show curvilinear set areas, bold black text indicates curvilinear set names (GG, W, etc.), the black dot with a number shows the parking location from which the image was collected, and black lines indicating the orientation and field of view of the image mosaic. The bedsets and curvilinear sets on this map are the same as in Figure 6 (Fergason et al. 2020) (Table S3).

Types of Downstream Accreting Architectural Elements with Primarily Grain Flow Deposition

Depositional Environment	**River - variable flow conditions (including delta plain)**	**River - "megaflood" conditions**	**Delta**	**Delta**
Unit Bar Type	Fluvial Bar	Fluvial Bar	Mouth Bar	Foreset
Lower Bounding Surface	Erosional	Erosional	Non-erosional (minor erosion may occur near jet initiation)	Non-erosional (minor erosion may occur near jet initiation)
Mean Dip Direction	Direction of channel flow	Direction of channel flow	"lakeward", can be bidirectional	"lakeward"
Primary Stacking Pattern	Aggradational, Progradational, Retrogradational (if channel flow direction "landward")	Progradational, Retrogradational (if channel flow direction "landward")	Aggradational, Progradational	Aggradational, Progradational
Height Scale	meters	~ 10 - 20 meters	meter to decameter	decameter
Bar Cross-section	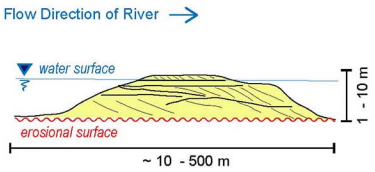	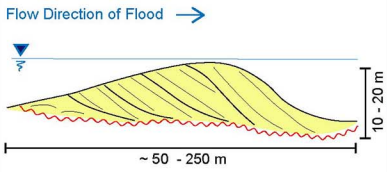	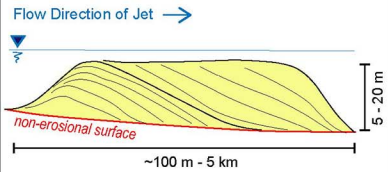	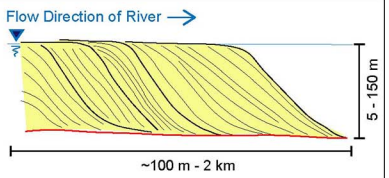
References	Bristow (1993); Best et al. (2003); Bridge and Lunt (2006); Mumpy et al. (2007); Sambrook Smit et al. (2009); Herbert et al. (2020); Almeida et al. (2024)	Baker (2002); Carling et al. (2009, 2016)	Cole et al. (2021); Winsemann et al. (2021)	Nemec (1990); Gobo et al. (2015); Winsemann et al. (2018); Budai et al. (2021)

FIG. 11.—Comparison of the physical and lower-bounding-surface characteristics of four downstream-accreting architectural elements with different depositional origins based on Earth analogs. When selecting analogous environments, preference was given to analog settings rich in sand and gravel (high bedload) with significant contributions from grainflow deposition. In the cross section, the architectural-element area is shaded yellow, the lower bounding surface is highlighted in red, depositional packages (e.g., unit bars) are bounded by bold black lines, stratification in depositional packages is indicated by thin black lines, and the water level is indicated by a blue horizontal line.

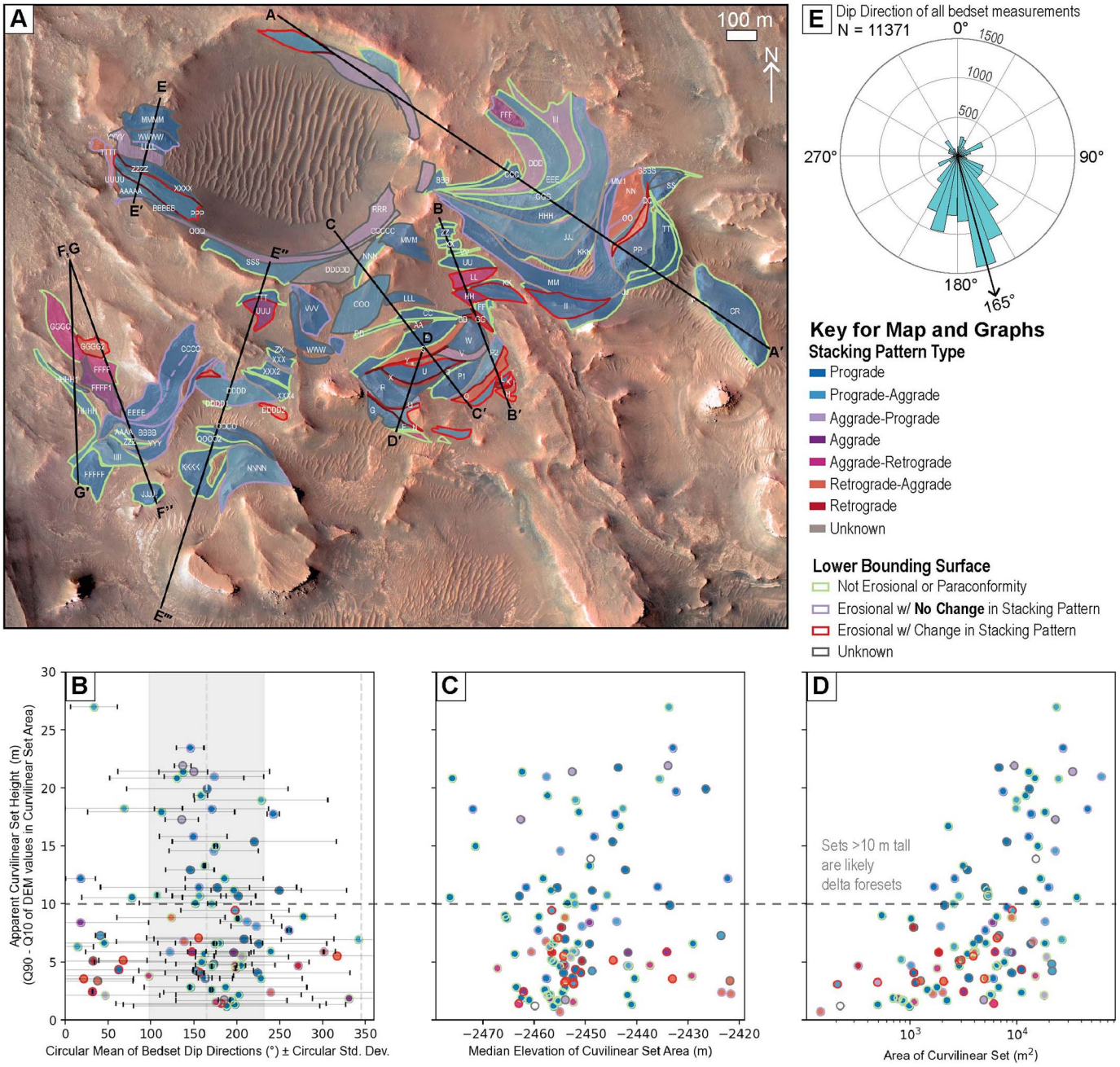

FIG. 12.—Physical attributes of curvilinear sets as derived from HiRISE image and elevation data (McEwen et al. 2007; Fergason et al. 2020) (Table 1; Table S3). **A)** Map of the curvilinear sets, color-coded by their stacking pattern and types of lower bounding surface. Graphs comparing apparent heights of curvilinear sets with their **B)** mean bedset dip directions, **C)** median elevations, and **D)** area. Dots are color-coded in the same way as in Part A. **E)** Rose diagram showing the distribution of all measurements of bedset dip directions.

curvilinear sets of all amplitudes. Curvilinear sets with retrogradational stacking patterns are the least common (N = 16), and most retrogradational curvilinear sets have an aggradational component (N = 12). All retrogradational sets have apparent heights of < 8 m.

The relative stacking order of adjacent curvilinear sets was determined using stratal relations in cross section (Fig. 13) constructed from orbital image data with some input from rover images (e.g., Fig. 9) and RIMFAX radargrams (Fig. 14). Erosional and non-erosional lower bounding surfaces are present in curvilinear sets of all apparent amplitudes and stacking patterns (Fig. 12).

Interpretations of Sedimentary Architecture.—There appear to be two populations of curvilinear sets with distinct physical characteristics: those > 10 m tall and those < 10 m tall.

Curvilinear sets whose amplitudes are greater than 10 m have progradational stacking patterns and lower bounding surfaces that are either non-erosional or erosional without change in stacking pattern (Fig. 12). These characteristics suggest that the tall curvilinear sets are delta foresets, with heights in the decameter range, "lakeward" bedset dip directions (assuming a sand-dominated, low-cohesion, low-rugosity delta; Caldwell and Edmonds (2014) and Burpee et al.

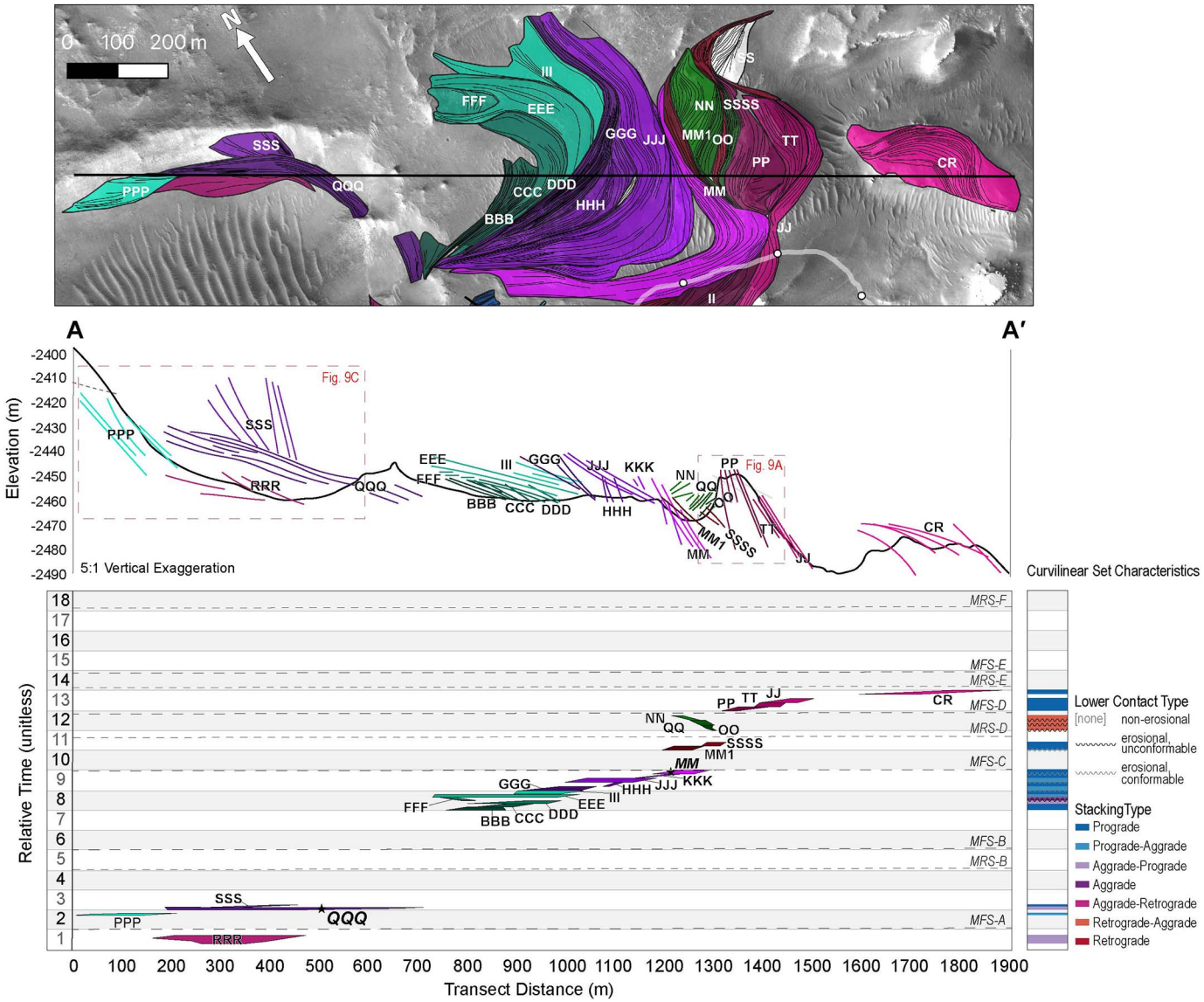

FIG. 13.—Map views, cross sections, and the resulting Wheeler diagrams of the Skrinkle Haven mbr curvilinear sets from **A)** A–A′, **B)** B–B′, C–C′, and D–D′, **C)** E–E′ and E″– E‴, and **D)** F–F′ and G–G′. The Wheeler diagrams are summarized and related to curvilinear-set attributes in Figure 15. Curvilinear sets are indicated by the set name (A, AAA, AAAA, etc.) and the same color in the map views, cross sections, and Wheeler diagrams. Dashed lines on Wheeler diagrams show maximum-flooding surfaces (MFSs) and maximum regressive surfaces (MRSs) interpreted from the composite Wheeler diagram in Figure 15. Dashed red boxes on the cross sections indicate extent of outcrops shown in Figure 9. A shapefile of bedset traces is File S5, a shapefile of curvilinear set areas is File S6, and a table of curvilinear-set attributes is S7.

(2015)), non-erosional lower bounding surfaces, and principally prograding stacking patterns.

Curvilinear sets with amplitudes less than ~ 10 m have much more diverse characteristics, including retrogradational stacking patterns, a wider range of mean dip directions, and lower bounding surfaces that are either erosional or non-erosional but delineate changes in stacking patterns (Fig. 12). There is sufficient diversity in these shorter curvilinear sets that they may represent more than one type of architectural element (Figs. 11, 12). Shorter curvilinear sets with progradational or aggradational stacking patterns and non-erosional lower bounding surfaces could be delta mouth bars or small delta foresets. Delta mouth bars will typically have heights up to ~ 10 m, dominantly lakeward bedsets dip directions, non-erosional lower bounding surfaces (possibly with minor scouring), and either progradational or aggradational stacking patterns. Shorter sets with erosional lower bounding surfaces, and especially those with retrogradational stacking patterns, are more likely to have been deposited as fluvial bars. Rivers bars that form under "megaflood" conditions are commonly ~ 10–20 m tall, have dip directions that mirror the direction of water flow (can be variable), have erosional lower bounding surfaces, and can have either progradational or retrogradational stacking patterns depending on the channel flow direction. Since these curvilinear sets are < 10 m tall, they are not likely megaflood bars (Fig. 11). Downstream-accreting fluvial unit bars (that are likely part of a larger compound bars) can have meter-scale heights, dip directions that mirror the direction of water flow (can be variable), and erosional lower bounding surfaces, and can have progradational, retrogradational, or aggradational stacking patterns.

The nature of curvilinear stratal sets in the Skrinkle Haven mbr suggests that the strata were deposited primarily as delta foresets but

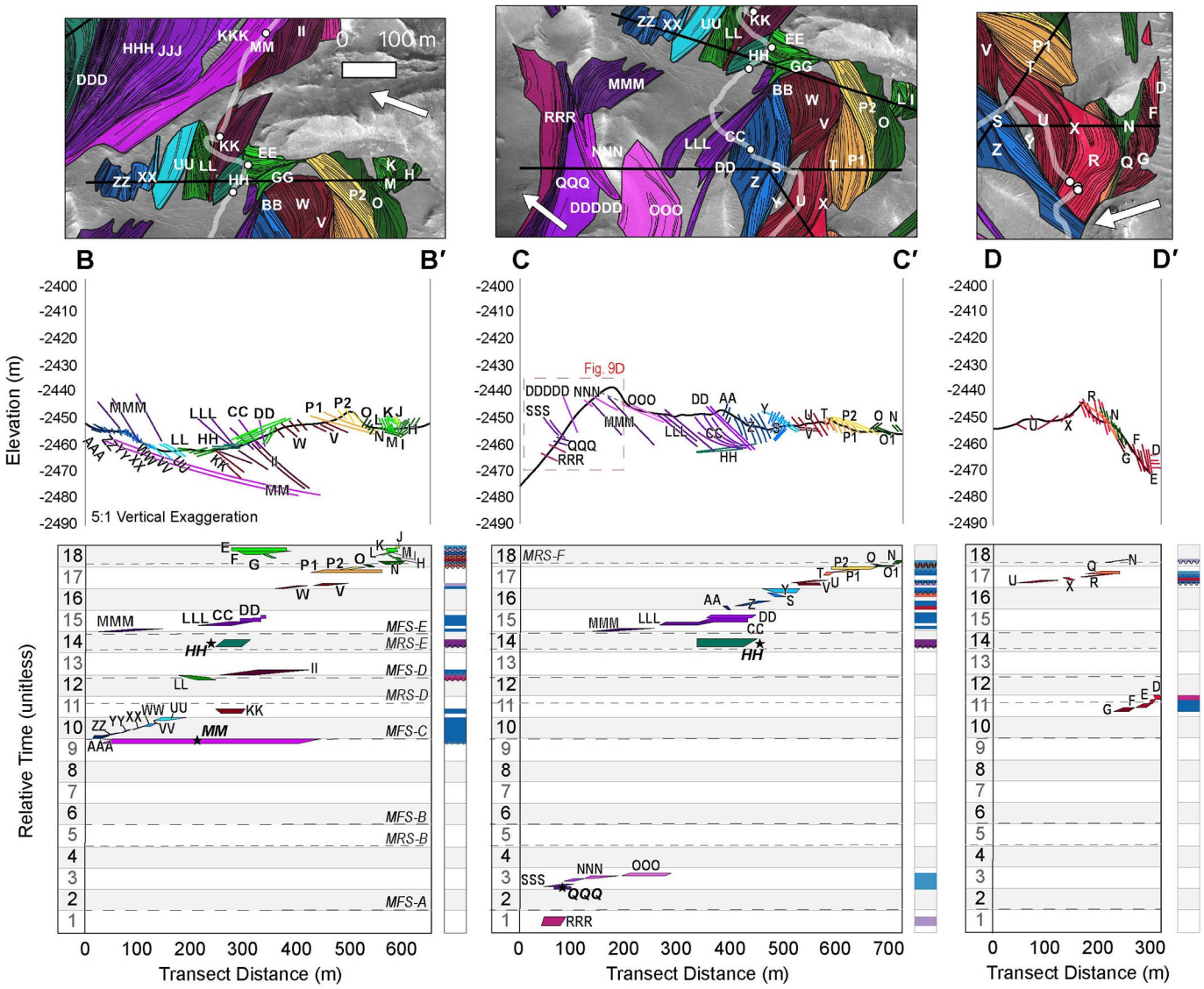

FIG. 13B.—Continued.

that delta mouth bars and/or (non-megaflood) fluvial bars may also be present.

Sequence Stratigraphy of the Skrinkle Haven Mbr

The sequence stratigraphy of the Skrinkle Haven mbr was analyzed to determine how its architectural elements (curvilinear sets) are related to each other in time and space. Cross sections (Fig. 13), architectural element geometries (Fig. 12), RIMFAX radargrams (Fig. 14), and rover images (Fig. 9) were all incorporated into the interpretation of the relative ages of the stacked curvilinear sets. Since the Skrinkle Haven mbr was most likely deposited through downstream-accreting grain flows, we assume that the bedsets in each curvilinear set young in the dip direction. To illustrate the relationship between curvilinear sets in time and space, Wheeler diagrams (Wheeler 1964; Qayyum et al. 2017) were constructed along each cross section (Figs. 13, 15; Table S7). The duration of unitless time assigned to each curvilinear set was selected purely to illustrate trends on the Wheeler diagrams. While determining the relative ages of curvilinear sets in a single cross section is a straightforward exercise, only a handful of curvilinear sets serve as tie points between cross sections (Figs. 13, 15).

Description of Sequences.—Six sequences were defined using five identified MFSs (Figs. 13, 15). Four of the six sequences have both regressive and transgressive systems tracts (Fig. 15A).

Sequence A, the oldest in the Skrinkle Haven mbr, consists of a single curvilinear set (RRR). This curvilinear set has an aggradational stacking pattern and an apparent height of ~ 17 m. Its bedsets dip consistently towards the southeast (Fig. 15). Whether this sequence is transgressive or regressive cannot be determined because there is only one curvilinear set. Sequence A is capped by maximum-flooding surface A (MFS-A; Figs. 13, 15). MFS-A is most clearly illustrated in cross section A–A′ (Figs. 9C, 13A) and C–C′ (Fig. 13B), where strata of Sequence B can be observed to downlap onto Sequence A. MSF-A is associated with an ~ 25 m increase in minimum relative lake level, as indicated by the maximum elevation of the curvilinear sets on either side of the surface (Fig. 15).

Sequence B is a full regressive–transgressive sequence bounded by MFS-A and MFS-B (Fig. 15A). This sequence contains the systems tracts RST-1 and TST-1, which are separated by MRS-B (Fig. 15). RST-1 progrades toward the south-southwest. The curvilinear sets in RST-1 decrease in apparent height through time from ~ 20 m to ~ 2 m. The curvilinear sets in

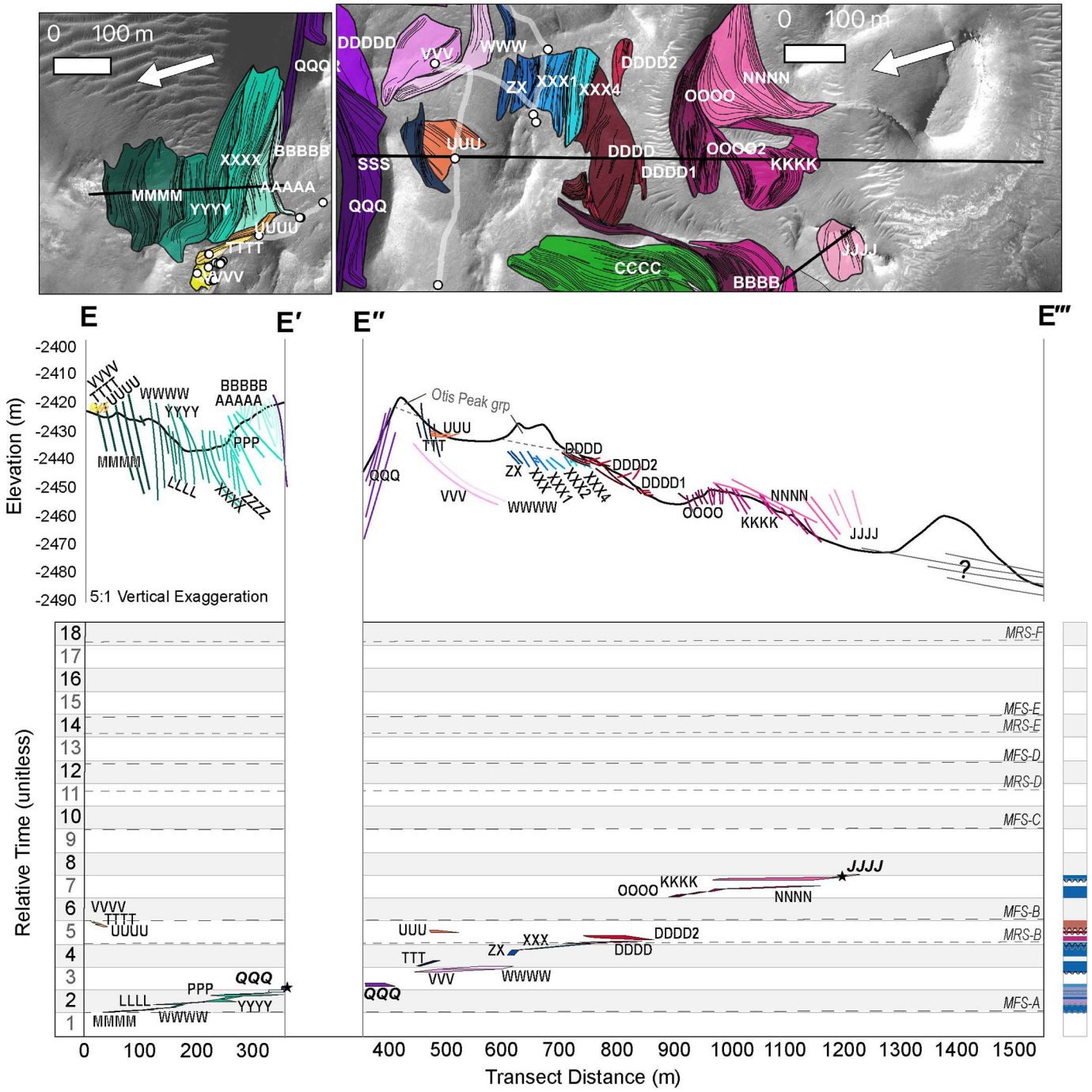

FIG. 13C.—Continued.

TST-1 overlie the RST-1 strata. The curvilinear sets in TST-1 have amplitudes that are consistently 5 m or less, and have erosional lower bounding surfaces (Figs. 13C, D, 15). The retrogradational character of the curvilinear sets in the TST-1 systems tract is best illustrated in time step 5 of cross section E″–E‴ (Fig. 13C), cross section F–F′ (Fig. 13D), and cross section G–G′ (Fig. 13D). Sequence B is overlain by MFS-B (Figs. 13, 15). MFS-B is most clearly illustrated in cross section G–G′ (Fig. 13D), where the progradational curvilinear sets of RST-2 (Sequence C) can be observed to downlap onto and have erosional contacts with TST-1 sets. MFS-B is associated with an ~ 25 m increase in relative lake level, as indicated minimum elevation of the curvilinear sets in TST-1 and the maximum elevation of the curvilinear sets in RST-2 (Fig. 15).

Sequence C is made up of two regressive systems tracts, RST-2 and RST-3, and is bounded by MFS-B and MFS-C (Fig. 15A). Both RST-2 and RST-3 are composed of tall, wide, progradational curvilinear sets with non-erosional lower bounding surfaces. RST-2 is best visualized in cross sections E″–E‴ (Fig. 13C) and F–F′ (Fig. 13D), and RST-3 in cross section A–A′ (Fig. 13A). The switch from RST-2 to RST-3 is accompanied by a change in depocenters from the south (RST-2) to the east (RST-3; Figs. 15, S9). Like RST-1, the average and maximum elevation of curvilinear sets in RST-2

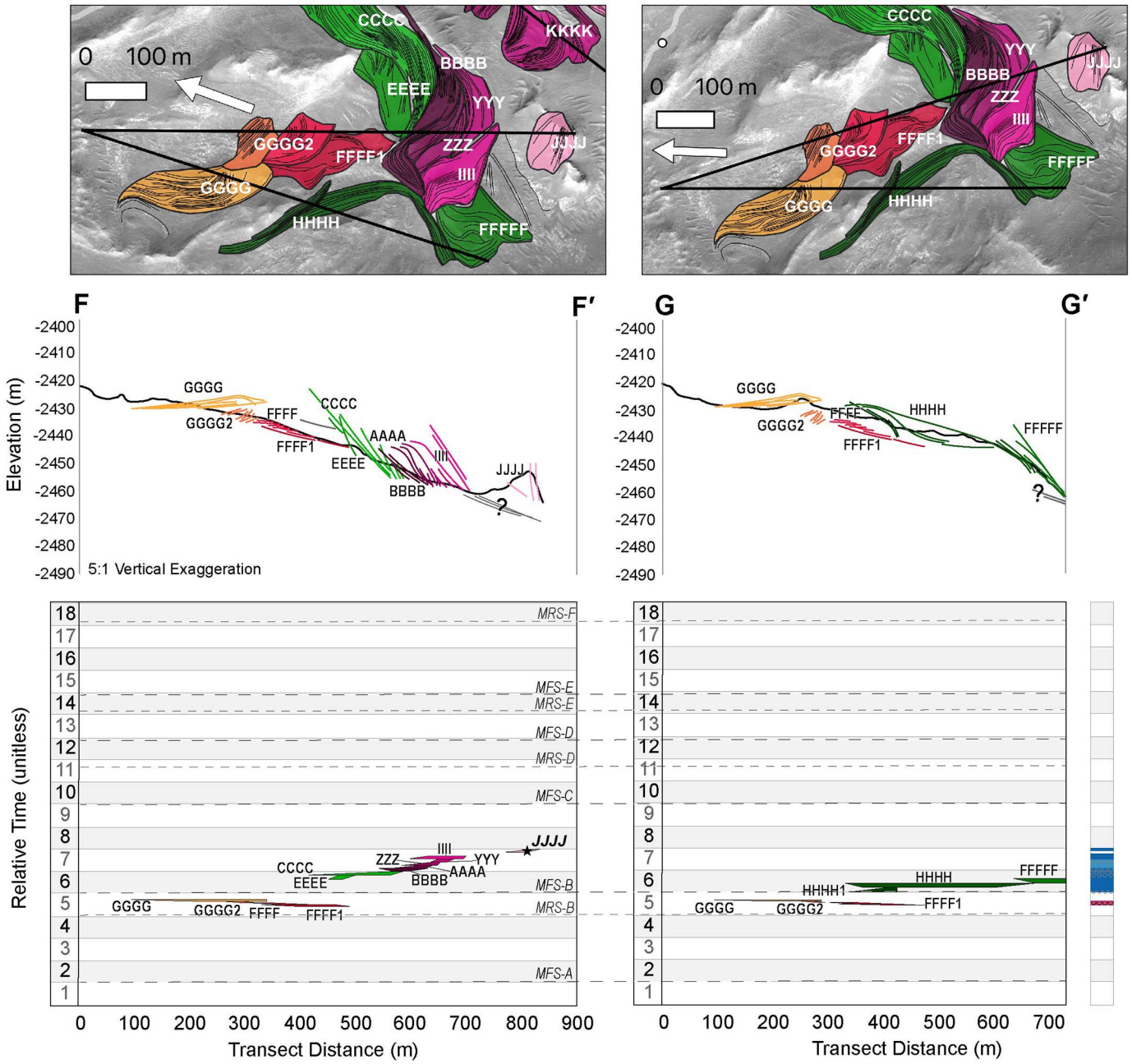

FIG. 13D.—Continued.

and RST-3 decrease over time (Fig. 15B). In RST-2, this decrease in elevation is accompanied by a decrease in curvilinear-set height from ~ 25 m to ~ 5 m, while in RST-3 the height increases through time from ~ 5 m to ~ 20 m (Figs. 15, 13A). Sequence C is overlain by MFS-C (Fig. 15). This surface is illustrated most clearly in cross section B–B′ (Fig. 13B), where progradational curvilinear sets in RST-4 can be observed to downlap onto RST-3. MFS-C is associated with an ~ 5 m increase in minimum lake level (Fig. 15).

Sequence D consists of a regressive systems tract (RST-4) followed by a transgressive systems tract (TST-4) and is bounded by MFS-C and MFS-D (Fig. 15A). The apparent set heights of RST-4 increase through time from 1.5 m to ~ 9 m, while the average elevation decreases from –2455 m to –2467 m (Fig. 15). The curvilinear sets of RST-4 are best visualized in cross sections A–A′ (Fig. 13A) and B–B′ (Fig. 13B). The curvilinear sets in TST-4 have retrogradational to aggradational stacking patterns, erosional bases, are 1.5 to 6 m tall, and their average elevation ranges from –2454 m to –2463 m (Fig. 15; Table S7). Sequence D is overlain by MFS-D. MFS-D is illustrated most clearly in cross sections A–A′ (Fig. 13A) and B–B′ (Fig. 13B), where the progradational curvilinear sets of RST-5 downlap and offlap strata in RST-4. MFS-D is associated with an ~ 15 m increase in lake level, as indicated by the minimum elevation of the curvilinear sets in TST-4 and maximum elevation of the curvilinear sets in RST-5 (Fig. 15).

Sequence E includes systems tracts RST-5 and TST-5, and is bounded by MFS-D and MFS-E. Curvilinear sets in RST-5 have apparent heights between 10.5 and 21 m and mean elevations from –2454 m to –2468 m. There are no clear temporal trends in the apparent heights of the curvilinear sets. The

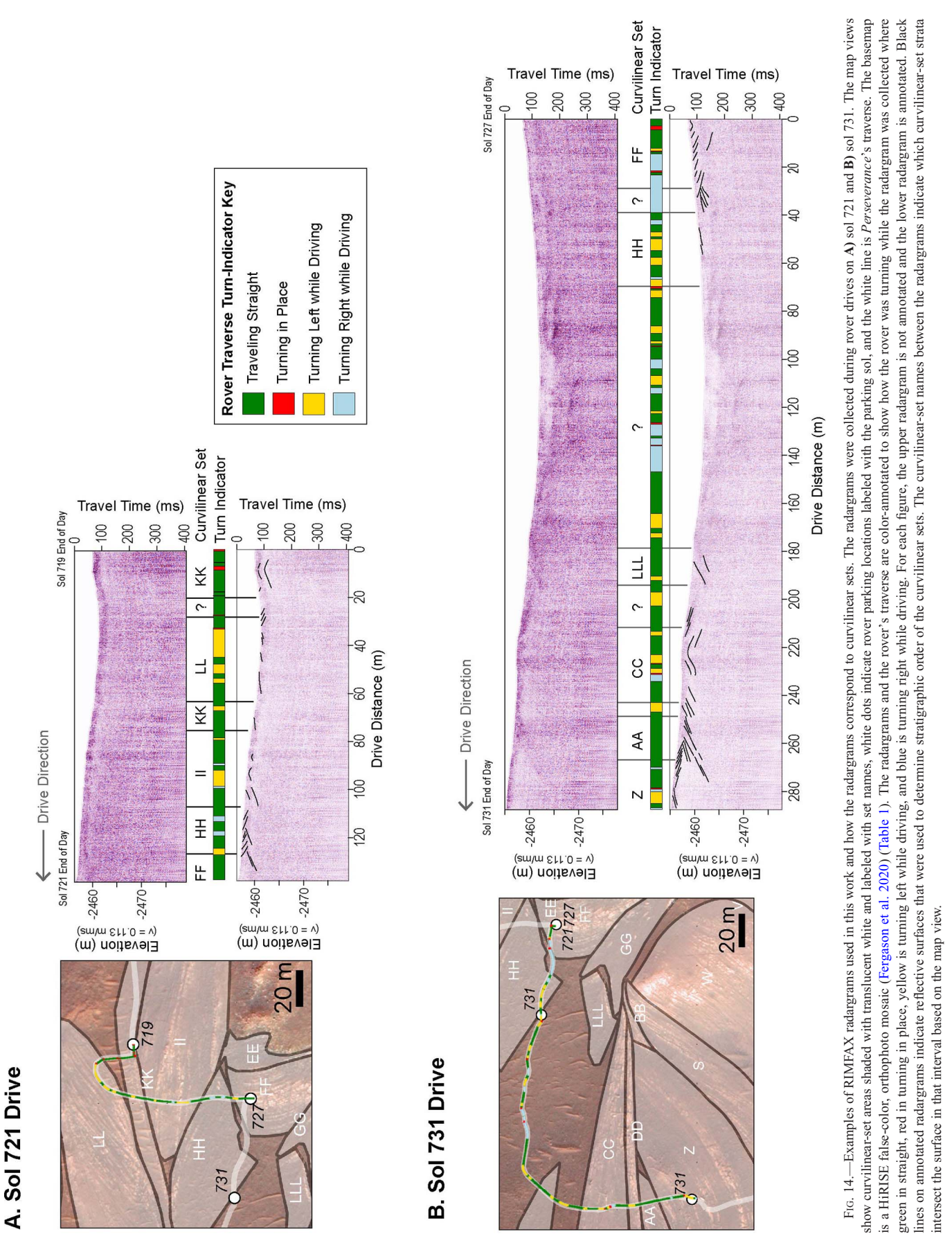

FIG. 14.—Examples of RIMFAX radargrams used in this work and how the radargrams correspond to curvilinear sets. The radargrams were collected during rover drives on **A)** sol 721 and **B)** sol 731. The map views show curvilinear-set areas shaded with translucent white and labeled with set names, white dots indicate rover parking locations labeled with the parking sol, and the white line is *Perseverance*'s traverse. The basemap is a HiRISE false-color, orthophoto mosaic (Fergason et al. 2020) (Table 1). The radargrams and the rover's traverse are color-annotated to show how the rover was turning while the radargram was collected where green in straight, red in turning in place, yellow is turning left while driving, and blue is turning right while driving. For each figure, the upper radargram is not annotated and the lower radargram is annotated. Black lines on annotated radargrams indicate reflective surfaces that were used to determine stratigraphic order of the curvilinear sets. The curvilinear-set names between the radargrams indicate which curvilinear-set strata intersect the surface in that interval based on the map view.

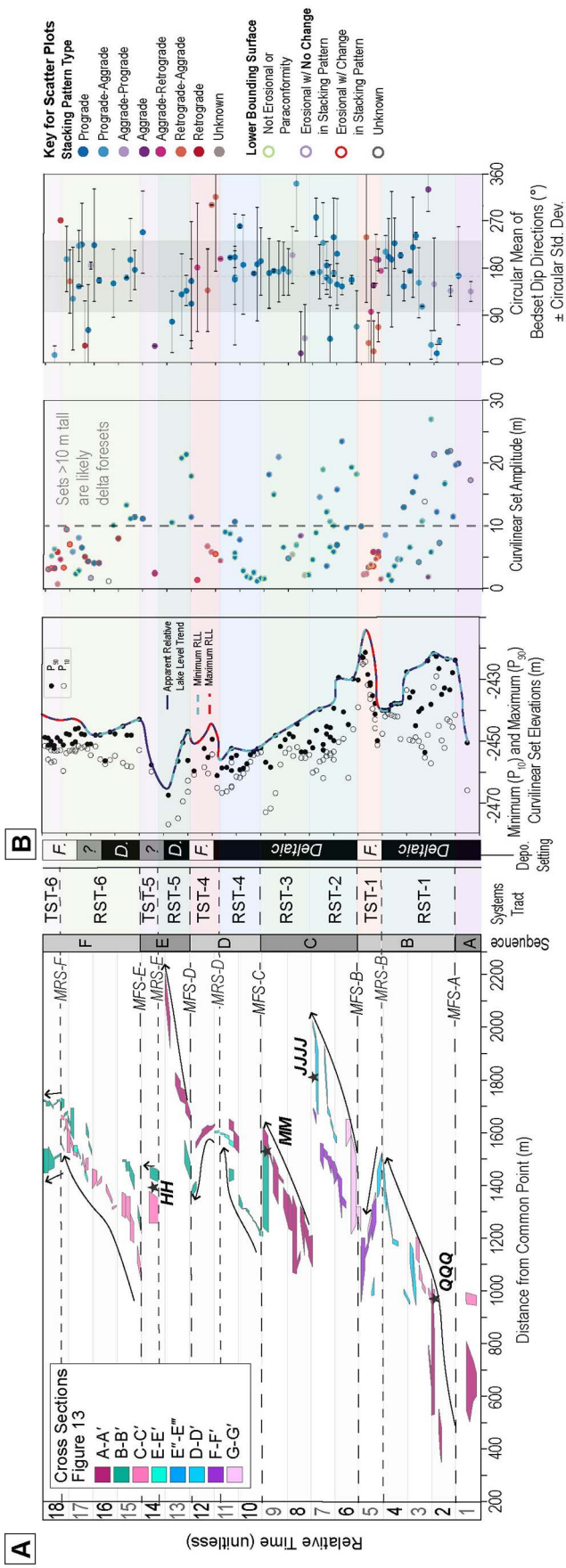

FIG. 15.—Summary of stratigraphic observations and interpretations. **A)** A composite relative Wheeler diagram created by converting distance along cross sections (Fig. 13) to distance from a common point located northwest of Belva Crater (Fig. S9). The extent of curvilinear sets is illustrated by colored polygons. The polygons are color-coded according to the cross section from which they are derived. Curvilinear sets with stars and labels occur on multiple cross sections and act as tie points. The black arrows show the general transgressive and regressive trends on the Wheeler diagram. Dashed lines indicate maximum-flooding surfaces (MFSs) and maximum regressive surfaces (MRSs). Systems tracts and sequences described in the text are labeled. **B)** Curvilinear set characteristics, elevation range, curvilinear set amplitude (relative height), and mean dip directions placed in relative stratigraphic order and the resulting interpretations including interpreted depositional setting (D, deltaic; F, fluvial;?, unknown) and trend of apparent relative lake level (RLL) in Jezero Crater inferred from minimum RLL of deltaic strata and maximum RLL of fluvial strata.

average elevations of the curvilinear sets in RST-5 do appear to decrease through time, but this may be due to the significant modern topographic drop that is present between the oldest and youngest sets of this interval (Fig. 13A). TST-5 consists of a single, aggradational curvilinear set (HH) that outcrops along cross section B–B′ and was imaged with RIMFAX (Figs. 6, 13B, 14, 15). While the stratigraphic context of TST-5 (HH) is somewhat ambiguous, HH acts as a cornerstone of the Skrinkle Haven mbr's relative stratigraphy because it overlies an erosional contact with systems tracts RST-4 and RST-5 and is overlain by strata in Sequence F (Fig. 13B). Sequence E is overlain by MFS-E (Figs. 13, 15). MFS-E is most clearly illustrated in cross section B–B′ and C–C′ (Fig. 13B) where systems tract RST-6 overlie the strata of Sequence E. MFS-E is associated with an ∼ 20 m increase in minimum lake level (Fig. 15B).

Sequence F is composed of system tracts RST-6 and TST-6 (Fig. 15). The base of Sequence F is bounded by MFS-E, and the top of constrained by the modern erosional surface. This is the youngest sequence, has the most diverse array of curvilinear set characteristics, and is also unique from the preceding sequences in that the average elevation of these sets remains relatively constant while the apparent heights of the sets decrease through time (Fig. 15). The strata of this sequence are best visualized in cross sections B–B′, C–C′, and D–D′ (Fig. 13B). The apparent height of curvilinear sets in RST-6 decreases from 11–13 m in the older sets to 1–1.5 m in the youngest sets (Fig. 13B). Regardless of height, the mean elevations of curvilinear sets in RST-6 range from –2450 m to –2455 m. RST-6 includes several small curvilinear sets with aggrading or retrograding stacking trends and erosional lower bounding surfaces (Figs. 15, 13B). In TST-6, curvilinear sets generally separated by erosional lower bounding surfaces, may have aggradational, progradation, or retrogradational stacking patterns, and are all < 10 m tall (Figs. 15, 13B).

Summary and Interpretation of Sequence Stratigraphy.—The oldest parts of the Skrinkle Haven mbr (Sequences A, B, and C) are composed primarily of tall (> 10 m), progradational curvilinear sets that are most likely deltaic foresets (Fig. 15). The amplitude (apparent height) of curvilinear sets in these sequences decreases through time, but they retain progradational stacking patterns and non-erosional bases, indicating that they are likely delta foresets. Some curvilinear sets that could represent fluvial deposition are present in TST-1 (Fig. 15). Next, in Sequences D and E, deltaic curvilinear sets continued to prograde over the area, but their size and growth appear constrained by the antecedent topography created by the preceding delta lobes, which lead to more avulsion and compensational stacking. The youngest strata of the Skrinkle Haven mbr are in Sequence F. Deposition of Sequence F began with prograding delta foresets and possibly delta mouth bars (RST-6) before transitioning into smaller, shorter, retrogradational, amalgamated curvilinear sets that are likely fluvial (TST-6).

Variation in relative lake levels of Jezero Crater through time can be inferred for the Skrinkle Haven mbr using the minimum and maximum elevation of curvilinear sets and their interpretation as either deltaic or fluvial. For curvilinear sets interpreted as deltaic (Fig. 15B), their maximum elevation is indicative of a minimum relative lake level. For curvilinear sets interpreted as possible fluvial bars, the maximum relative lake level is interpreted to be ∼ 10 m higher than their lowest point (P10, Fig. 15). This interpretation is based on the following assumptions:

1. that the minimum elevation (P10) of fluvial bars marks the maximum base level of the possible river flowing into Jezero Crater lake at the time of their deposition (Fig. 15).
2. Since no alluvial plain is preserved, we assume that these fluvial strata were deposited very near the river's mouth—that is, in the backwater zone—where a river's base level is below the local lake or sea level (e.g., Nittrouer et al. 2012).
3. The observations from this study provide information that is insufficient to calculate river characteristics in this backwater zone (e.g., van Yperen et al. 2024).

However, since all possible fluvial bars in the Skrinkle Haven mbr are < 10 m tall we assumed that 10 m is approximately the maximum channel depth, and therefore that maximum relative lake level is ∼ 10 m higher than river base level.

Based on those interpretations, relative lake levels appear to have ranged from –2415 m at the highest to –2465 m at the lowest during the deposition of the Skrinkle Haven mbr (Fig. 15B). There is an overall decreasing relative-lake-level trend from the oldest to the youngest sequences, and decreases through time during most sequences. The magnitude of apparent relative-lake-level rises associated with the maximum-flooding surfaces also appears to decrease through time, from ∼ 30 m during MFS-A and MFS-B to ∼ 15 m during MFS-D and MFS-E.

A decrease in relative lake level through time is present in most sequences, suggesting that the Skrinkle Haven mbr was deposited primarily during forced regressions. While the maximum elevation of deltaic strata constrains only minimum lake elevation, and cannot alone show lake-level decrease through time, the additional constraint of maximum lake level interpreted from the erosional lower bounding surface of fluvial curvilinear sets does allow the interpretation of falling lake levels during Sequences B, D, and F (Fig. 15). The interpretation of forced regression during Sequences A, C, and E cannot be made as confidently, since those sequences do not contain possible fluvial strata (Fig. 15B). Additionally, the Skrinkle Haven mbr has many of the characteristics of forced-regressive deposits (Posamentier and Morris 2000), including the presence of deposits of sharp-based delta front (Figs. 9, 13), the presence of progressively shallower clinoforms from proximal to distal positions (e.g., Sequence F), and the absence of correlative fluvial strata capping proximal regressive deposits (Figs. 13, 15).

The sequence stratigraphy of the Skrinkle Haven mbr suggests that variability in the physical characteristics of the curvilinear sets occurred in response to variations in accommodation, which, along with sediment supply, ultimately drove whether deposition of the curvilinear sets as either delta forests, delta mouth bars, and fluvial bars. Accommodation in the Jezero Crater lake basin can be considered entirely a consequence of relative-lake-level fluctuations and sediment input because Mars lacks the mechanisms for tectonic subsidence and any subsidence of the Jezero Crater basin due to deposition of the 200-m-thick Jezero Crater western fan is likely negligible. Accommodation is inferred to have changed through time due to a combination of change in relative lake level on the order of tens of meters with concomitant filling of accommodation at the shoreline by a prograding delta system. The tallest apparent height of a deltaic curvilinear set is 27 m in RST-1, indicating that water in that location was at least 27 m deep during deposition. Sediment filling of antecedent topography is demonstrated by the downlapping relationships between sequences of the Skrinkle Haven mbr (Fig. 13). Additionally, the regressive systems tracts of Sequence C illustrate how the height of deltaic foresets of the Skrinkle Haven member are responding to decrease in accommodation due to sediment supply. The different accretion directions of systems tracts RST-2 (south-southwest) and RST-3 (southeast) indicate that these intervals were deposited as different depocenters or delta lobes. Since the lake-level elevation does not appear to change significantly between the end of RST-2 and the beginning of RST-3 (Fig. 15), this change in depocenter location is likely due to avulsion and indicates that compositional stacking was sometimes the driver of lobe switching.

DISCUSSION

The Skrinkle Haven mbr of the Tenby fm is composed of planar-bedded, steeply dipping sandstones and conglomerates that were likely deposited as subaqueous grain flows. The contacts between sandstone and conglomerate

lithologies are sharp (nongradational). Beds and bedsets of the Skrinkle Haven mbr are organized into curvilinear sets—stratigraphic architectural elements in which the planes of the constituent bedsets are parallel to one another. The sedimentary architecture of these curvilinear sets suggests that they were deposited as deltaic foresets, delta mouth bars, and fluvial bars. The foresets, mouth bars, and fluvial bars were deposited as delta lobes that prograded toward the southeast into lake waters that were, at their deepest, at least 27 m deep. The sequence stratigraphy of this delta system suggests that lake level fluctuated on the order of tens of meters during the deposition of the Skrinkle Haven mbr. There also appear to be times when lake level was relatively stable compared to sediment input rates, resulting in avulsion and compensational stacking of delta lobes (Sequence C).

Comparison with Other Rover-Characterized Deltaic Strata in Jezero Crater

The Skrinkle Haven mbr is not the only deltaic sedimentary succession present in the Jezero Crater western fan. Other parts of the Tenby fm (Fig. 3) near the southern edge of the fan (Mangold et al. 2021, 2024), outcrops at the Kodiak Butte outlier (Mangold et al. 2021; Caravaca et al. 2024), and the Rockytop mbr (Stack et al. 2024) have also been interpreted from rover observations to be deltaic. However, the deltaic strata described by Mangold et al. (2024) and Caravaca et al. (2024) differ meaningfully from the Skrinkle Haven mbr in two ways that emphasize some idiosyncratic characteristics of the Skrinkle Haven mbr's sedimentology and stratigraphy. First, the Kodiak Butte and fan-front deltaic strata have a classic Gilbert-type stratigraphy, complete with topsets, foresets, and bottom sets. This contrasts with the Skrinkle Haven mbr, which has a much less ordered stratigraphy. Specifically, the Skrinkle Haven mbr does not have consistently preserved fluvial strata (topsets), which limits our ability to understand how sediment was delivered to the delta slope. This dearth of topsets is, however, consistent with steep, subaqueous, coarse-grained deltas deposited in relatively deep water (Nemec 1990) and with the diagnostic criteria for forced regressions (Posamentier and Morris 2000). The possibility exists that the cross-bedded gravels of the Carew Castle mbr (Fig. 3) are preserved topsets, but their stratigraphic relationship to the Skrinkle Haven mbr is unclear since the contact between the two formations is obscured by talus and regolith. Second, the Kodiak Butte and fan-front deltaic strata are composed of sandstones and conglomerates, like the Skrinkle Haven mbr, but do not exhibit such a stark contrast in grain-size distribution between bedsets, a consistent feature of the Skrinkle Haven mbr. The stark contrast in grain-size between F1 and F2 in the Skrinkle Haven mbr could have several causes (see Lithofacies Interpretations), but regardless of the driver the same does not appear to influence deposition in the Kodiak Butte or fan-front deltaic strata.

These contrasts suggest that not all of the deltaic strata in the Jezero Crater western fan were deposited under the same conditions, and that these differences were likely driven by both lake-level variability (as indicated by the stratigraphy) and differences in watershed dynamics (as indicated by the lithofacies).

Comparison with Pre-Landing Hypotheses

Before the investigation of these strata by the *Perseverance* rover, analysis of orbiter data had led to the following interpretations: that a) the Jezero Crater western fan was deposited as a delta, and b) that the curvilinear unit (Skrinkle Haven mbr) represents topsets of this delta deposited as laterally accreting bars in a sinuous river channel in muddy floodplains rich with detrital clay (Ehlmann et al. 2008; Schon et al. 2012; Goudge et al. 2015, 2017, 2018). These hypotheses were largely supported by observations of Fe-Mg smectite (clay) minerals in Mars Reconnaissance Orbiter data (Table 1) and the interpretations of curvilinear geometries as scroll bars in a meandering fluvial system. The interpretation of the Skrinkle Haven mbr outlined in this paper also calls for deltaic and fluvial deposition, but of a character that is very different from that of the meandering channels in a mud-rich floodplain topping a delta prograding into a gradually rising lake conceptualized before *Perseverance*'s exploration on the surface in Jezero Crater (Schon et al. 2012; Goudge et al. 2018; Lapôtre and Ielpi 2020). The clay minerals detected from orbit in this unit do not appear to have been deposited as clay-size detrital grains, but instead are weathering products associated with larger detrital grains.

We conclude here that the depositional process (grain flow) required to explain the lithofacies of the Skrinkle Haven mbr, and the sequence stratigraphy of the member, cannot be explained as laterally accreting point bars. Rather, we favor an interpretation of the Skrinkle Haven mbr as a sequence of delta foresets and mouth bars, with intervals of fluvial deposition, deposited preferentially during forced regressions under decameter-scale variations in lake level.

Though both the orbiter- and rover-derived hypotheses for the origin of the Skrinkle Haven mbr call for a deltaic interpretation, the character of the invoked deltas differ in key ways. One difference between the interpretations is how the clay minerals (Fe-Mg smectites) fit into the depositional system, which is important to consider because the presence of clay informs interpretations of the paleohydrology of the watershed and the potential habitability of Jezero Crater western fan (Bosak et al. 2021). In the orbiter hypothesis, these clays are part of a muddy delta plain. Such a delta plain suggests that the river had a relatively low gradient (0.0001–0.01%; Orton and Reading 1993) and that the clay was deposited through suspension from settling in overbank deposits. Such a relatively calm and wet environment of a muddy, flooded delta plain has a high potential for habitability and for biosignature preservation (Summons et al. 2011; Mangold et al. 2020). In contrast, a coarse-grained delta with few to no preserved muddy intervals (like the delta described in this work) has poor biosignature-preservation potential due to its lack of deposited fine-grained sediments. Delta plains fed by coarse-grained rivers typically have relatively steep gradients of 0.05–0.5% (Orton and Reading 1993), which is more similar to the 0.7–1.7% gradient calculated for the modern Neretva Vallis channel (Mangold et al. 2020). The orbiter interpretation of the Skrinkle Haven mbr as fluvial topsets led to the interpretation that the Jezero western fan was deposited during a period of lake-level rise, resulting in shoreline transgression (Goudge et al. 2018). This interpretation is more-or-less the opposite of the findings of the sequence stratigraphic analysis presented in this paper, where shoreline regression and relative-lake-level falls appear to have strongly influenced depositional patterns.

Therefore, though both orbiter and rover observations resulted in deltaic interpretations of the Skrinkle Haven mbr, the two interpretations have very different implications for biosignature preservation and paleolacustrine history of Jezero Crater.

Paleohydrology of the Jezero Crater Lake System

The sequence stratigraphy of the Skrinkle Haven mbr can be used to constrain lake level in Jezero Crater through time (Fig. 15). Based on the interpretations presented in this work, the highest minimum relative lake level is –2415 m, and the lowest is –2465 m. This difference in lake level and the patterns in the sequence stratigraphy suggest that the lake level in Jezero fluctuated by at least 40–50 m during the deposition of the Skrinkle Haven mbr, with a preference for deposition during intervals of lake-level fall (Fig. 15). The modern elevation of the Jezero Crater lake basin's spillpoint through the Pliva Vallis bedrock channel is around –2400 m (Schon et al. 2012; Goudge et al. 2015). Therefore, the Skrinkle Haven mbr was likely deposited when the Jezero Crater lake was a closed basin. Since the top of deltaic curvilinear sets indicate only the minimum lake level at the time of deposition, there is a possibility that the lake was at or above the –2400 m elevation of the Pliva Vallis outlet.

The history of lake levels in Jezero Crater during the deposition of the western fan can be reconstructed when lake-level interpretations in this

study are combined with those from the fan front (Mangold et al. 2021, 2024; Stack et al. 2024), outcrops at the Kodiak Butte outlier (Mangold et al. 2021; Caravaca et al. 2024), and the underlying Shenandoah fm (Stack et al. 2024). First, the lower Shenandoah fm was deposited as a distal alluvial fan with some standing water in overbank settings, indicating that relative lake levels in Jezero Crater did not exceed –2540 m (Stack et al. 2024). The upper Shenandoah fm is composed of fine-grained, laminated lacustrine sediments that indicate that lake levels subsequently rose to at least –2510 m (Stack et al. 2024). As lake levels rose, the Tenby fm and other deltaic strata, like Kodiak Butte, were deposited (Mangold et al. 2021; Caravaca et al. 2024; Stack et al. 2024). During the deposition of these fluvial–deltaic systems, lake levels ranged from –2490 m at Kodiak Butte to at least –2415 m in the Skrinkle Haven mbr.

Ultimately, rover observations of stratigraphy and interpretation of lake levels in the Skrinkle Haven mbr partially agree with the interpretation made by Goudge et al. (2018) that the deltaic strata of the Jezero Crater western fan were deposited during a gradual transgression. Broadly, the Tenby fm was deposited by the progradation of fluvial–deltaic strata into a lake in Jezero Crater following a significant transgression whose onset was recorded by the upper Shenandoah fm. However, the decameter fluctuations in lake levels recorded in the stratigraphy of the Skrinkle Haven mbr do not seem to reflect a steady lake level or transgression. Instead, the Skrinkle Haven mbr invokes a picture of episodic deposition during decameter-scale lake-level falls punctuated by lake-level rises of equal or greater magnitude. Within these lake-level fluctuations, there were intervals where lake levels were sufficiently stable relative to sediment input such that compensational stacking occurred (Sequence C). Notably, most of these lake-level fluctuations occurred below –2400 m and therefore are unlikely related to the breach of Jezero Crater via the Pliva Vallis outlet. Therefore, the apparent dynamic lake levels in Jezero Crater during the deposition of the Skrinkle Haven mbr were likely due to closed-lake-basin processes.

Future Work

The architectural-element and sequence-stratigraphic observations and interpretations made in this work were derived from orbiter data. Such orbiter data are also available for the northern exposure of curvilinear strata (likely Skrinkle Haven mbr) in the Jezero Crater western fan (Fig. 1D). A similar analysis conducted on the northern exposure of curvilinear strata could be used to test the findings of this study and possibly extend our understanding of how lake-level fluctuations influenced the deposition of the Skrinkle Haven mbr.

The depositional interpretations presented in this work are strongly informed by the fact that no current-transport bedforms were observed in the Skrinkle Haven mbr. If *Perseverance* returns to the Jezero Crater western fan, the assumption that all the Skrinkle Haven mbr strata were deposited through grain flow could be tested by looking for current-transport bedforms in outcrops not previously imaged by the rover. If current-transport bedforms were identified, then the sedimentary architecture and sequence stratigraphy interpretations in this paper could be improved. Of particular interest would be curvilinear sets identified as potentially fluvial (retrogradational stacking trends and erosional bases; Figs. 12, 15), since fluvial strata would have the highest potential for producing current-transport bedforms. Additionally, rover-proximal observations of any competent F2 outcrops would allow refinement of the depositional model for that facies by supplying detailed information on grain-size distribution and grain composition.

Future laboratory measurements of the Melyn sample could test the depositional model proposed here, if the sample is returned to Earth for study as part of the Mars Sample Return mission (Weiss et al. 2024; Herd et al. 2025). The grain-size distribution of facies F1 can be assessed more precisely. A detrital versus authigenic origin of phyllosilicates and other alteration minerals can be established using relationships observed with microscopy and measurements comparing their magnetization directions with that of unaltered materials. The relative depositional ages of curvilinear sets can be bounded using radioisotope measurements of cements and detrital grains. Analysis of the cements would allow insights into past aqueous conditions before and following deposition, including dissolution of the protolith, cementation, the chemistry of the fluid, and, ultimately, the habitability of Jezero lake.

CONCLUSIONS

- The Skrinkle Haven mbr of the Tenby fm is a clastic sedimentary unit in the Jezero Crater western fan, Mars. It is composed of two distinct lithofacies, a fine-grained sandstone and a pebble conglomerate. These facies are interstratified, and contacts between them are sharp. Both lithofacies were deposited through grain flow as downstream-accreting delta foresets, delta mouth bars, and fluvial bars.
- The sequence stratigraphy of the Skrinkle Haven mbr suggests that these strata accumulated as prograding delta lobes during normal and forced regressions with some possible fluvial deposition during transgressions and some lowstands.
- Water levels in Jezero Crater likely fluctuated on the order of tens of meters during the deposition of the Skrinkle Haven mbr, from around –2465 m and –2415 m. Most of these lake-level fluctuations occurred below –2400 m and therefore are unlikely to have been related to the breach of Jezero Crater via the Pliva Vallis outlet, suggesting that the Skrinkle Haven mbr was deposited in a closed lake system.
- The differences between the Skrinkle Haven mbr fluvial–deltaic strata and fluvial–deltaic strata in other parts of the Jezero Crater western fan suggest variability in lake level and watershed dynamics during the deposition of the fan.

DATA AVAILABILITY STATEMENT

The rover and orbiter data used in this study are publicly available in the sources listed in Table 1 and Table S3. Products created in support (shapefiles, code, tables, etc.) of this study are available in the Supplementary Materials.

ACKNOWLEDGMENTS

This research was carried out in part at the Jet Propulsion Laboratory, California Institute of Technology, under a contract with the National Aeronautics and Space Administration. The authors acknowledge the contributions of the large and talented team that conceived, created, and operated the *Perseverance* rover and the Mars 2020 mission. The work of GC and NM was supported by the French Space Agency CNES, focused on SuperCam and on Mars2020-Perseverance. The authors thank D.G.F. Long, L.J. Wood, and B.T. Cardenas for their thoughtful reviews, which strengthened this manuscript.

REFERENCES

Allen, J.R.L., 1970, The avalanching of granular solids on dune and similar slopes: The Journal of Geology, v. 78, p. 326–351, doi:10.1086/627520.

Almeida, R.P., Galeazzi, C.P., Best, J., Ianniruberto, M., Do Prado, A.H., Janikian, L., Mazoca, C.E., Tamura, L.N., and Nicholas, A., 2024, Morphodynamics and depositional architecture of mid-channel bars in large Amazonian rivers: Sedimentology, v. 71, p. 1591–1614, doi:10.1111/sed.13188.

Baker, V.R., 2002, High-energy megafloods: planetary settings and sedimentary dynamics, *in* Martini, I.P., Baker, V.R., and Garzón, G., eds., Flood and Megaflood Processes and Deposits: Recent and Ancient Examples: International Association of Sedimentologists, Special Publication 32, p. 3–16, doi:10.1002/9781444304299.ch1.

Baker, V.R., and Bunker, R.C., 1985, Cataclysmic late Pleistocene flooding from glacial Lake Missoula: a review: Quaternary Science Reviews, v. 4, p. 1–41, doi:10.1016/0277-3791(85)90027-7.

Banham, S.G., Gupta, S., Rubin, D.M., Watkins, J.A., Sumner, D.Y., Edgett, K.S., Grotzinger, J.P., Lewis, K.W., Edgar, L.A., Stack-Morgan, K.M., Barnes, R., Bell, J.F., III, Day, M.D., Ewing, R.C., Lapotre, M.G.A., Stein, N.T., Rivera-Hernandez, F., and Vasavada, A.R., 2018, Ancient Martian aeolian processes and palaeomorphology

reconstructed from the Stimson formation on the lower slope of Aeolis Mons, Gale crater, Mars: Sedimentology, v. 65, p. 993–1042, doi:10.1111/sed.12469.

Beaty, D.W., Grady, M.M., McSween, H.Y., Sefton-Nash, E., Carrier, B.L., Altieri, F., Amelin, Y., Ammannito, E., Anand, M., Benning, L.G., Bishop, J.L., Borg, L.E., Boucher, D., Brucato, J.R., Busemann, H., Campbell, K.A., Czaja, A.D., Debaille, V., Des Marais, D.J., Dixon, M., Ehlmann, B.L., Farmer, J.D., Fernandez-Remolar, D.C., Filiberto, J., Fogarty, J., Glavin, D.P., Goreva, Y.S., Hallis, L.J., Harrington, A.D., Hausrath, E.M., Herd, C.D.K., Horgan, B., Humayun, M., Kleine, T., Kleinhenz, J., Mackelprang, R., Mangold, N., Mayhew, L.E., McCoy, J.T., McCubbin, F.M., McLennan, S.M., Moser, D.E., Moynier, F., Mustard, J.F., Niles, P.B., Ori, G.G., Raulin, F., Rettberg, P., Rucker, M.A., Schmitz, N., Schwenzer, S.P., Sephton, M.A., Shaheen, R., Sharp, Z.D., Shuster, D.L., Siljeström, S., Smith, C.L., Spry, J.A., Steele, A., Swindle, T.D., ten Kate, I.L., Tosca, N.J., Usui, T., Van Kranendonk, M.J., Wadhwa, M., Weiss, B.P., Werner, S.C., Westall, F., Wheeler, R.M., Zipfel, J., and Zorzano, M.P., 2019, The potential science and engineering value of samples delivered to Earth by Mars sample return: Meteoritics and Planetary Science, v. 54, p. S3–S152, doi:10.1111/maps.13242.

Beegle, L.W., and Bhartia, R., 2021, Mars 2020 SHERLOC Bundle: Planetary Data System (PDS) Geosciences (GEO) Node, doi:10.17189/1522643.

Bell, J.F., and Maki, J.N., 2021, Mars 2020 Mast Camera Zoom Bundle: Arizona State University Mastcam-Z Instrument Team, calibrated products, Planetary Data System (PDS) Geosciences (GEO) Node, doi:10.17189/q3ts-c749.

Bell, J.F., Maki, J.N., Mehall, G.L., Ravine, M.A., Caplinger, M.A., Bailey, Z.J., Brylow, S., Schaffner, J.A., Kinch, K.M., Madsen, M.B., Winhold, A., Hayes, A.G., Corlies, P., Tate, C., Barrington, M., Cisneros, E., Jensen, E., Paris, K., Crawford, K., Rojas, C., Mehall, L., Joseph, J., Proton, J.B., Cluff, N., Deen, R.G., Betts, B., Cloutis, E., Coates, A.J., Colaprete, A., Edgett, K.S., Ehlmann, B.L., Fagents, S., Grotzinger, J.P., Hardgrove, C., Herkenhoff, K.E., Horgan, B., Jaumann, R., Johnson, J.R., Lemmon, M., Paar, G., Caballo-Perucha, M., Gupta, S., Traxler, C., Preusker, F., Rice, M.S., Robinson, M.S., Schmitz, N., Sullivan, R., and Wolff, M.J., 2021, The Mars 2020 *Perseverance* Rover Mast Camera Zoom (Mastcam-Z) Multispectral, Stereoscopic Imaging Investigation: Space Science Reviews, v. 217, doi:10.1007/s11214-020-00755-x.

Best, J.L., Ashworth, P.J., Bristow, C.S., and Roden, J., 2003, Three-dimensional sedimentary architecture of a large, mid-channel sand braid bar, Jamuna River, Bangladesh: Journal of Sedimentary Research, v. 73, p. 516–530, doi:10.1306/010603730516.

Beyssac, O., Forni, O., Cousin, A., Udry, A., Kah, L.C., Mandon, L., Clavé, O.E., Liu, Y., Poulet, F., Quantin Nataf, C., Gasnault, O., Johnson, J.R., Benzerara, K., Beck, P., Dehouck, E., Mangold, N., Alvarez Llamas, C., Anderson, R.B., Arana, G., Barnes, R., Bernard, S., Bosak, T., Brown, A.J., Castro, K., Chide, B., Clegg, S.M., Cloutis, E., Fouchet, T., Gabriel, T., Gupta, S., Lacombe, G., Lasue, J., Le Mouelic, S., Lopez-Reyes, G., Madariaga, J.M., McCubbin, F.M., McLennan, S.M., Manrique, J.A., Meslin, P.Y., Montmessin, F., Núñez, J., Ollila, A.M., Ostwald, A., Pilleri, P., Pinet, P., Royer, C., Sharma, S.K., Schröder, S., Simon, J.I., Toplis, M.J., Veneranda, M., Willis, P.A., Maurice, S., Wiens, R.C., and The SuperCam Team, 2023, Petrological traverse of the olivine cumulate Séítah formation at Jezero Crater, Mars: a perspective from SuperCam onboard *Perseverance*: Journal of Geophysical Research, Planets, v. 128, no. e2022JE007638, doi:10.1029/2022JE007638.

Bhartia, R., Beegle, L.W., DeFlores, L., Abbey, W., Razzell Hollis, J., Uckert, K., Monacelli, B., Edgett, K.S., Kennedy, M.R., Sylvia, M., Aldrich, D., Anderson, M., Asher, S.A., Bailey, Z., Boyd, K., Burton, A.S., Caffrey, M., Calaway, M.J., Calvet, R., Cameron, B., Caplinger, M.A., Carrier, B.L., Chen, N., Chen, A., Clark, M.J., Clegg, S., Conrad, P.G., Cooper, M., Davis, K.N., Ehlmann, B., Facto, L., Fries, M.D., Garrison, D.H., Gasway, D., Ghaemi, F.T., Graff, T.G., Hand, K.P., Harris, C., Hein, J.D., Heinz, N., Herzog, H., Hochberg, E., Houck, A., Hug, W.F., Jensen, E.H., Kah, L.C., Kennedy, J., Krylo, R., Lam, J., Lindeman, M., McGlown, J., Michel, J., Miller, E., Mills, Z., Minitti, M.E., Mok, F., Moore, J., Nealson, K.H., Nelson, A., Newell, R., Nixon, B.E., Nordman, D.A., Nuding, D., Orellana, S., Pauken, M., Peterson, G., Pollock, R., Quinn, H., Quinto, C., Ravine, M.A., Reid, R.D., Riendeau, J., Ross, A.J., Sackos, J., Schaffner, J.A., Schwochert, M.O., Shelton, M., Simon, R., Smith, C.L., Sobron, P., Steadman, K., Steele, A., Thiessen, D., Tran, V.D., Tsai, T., Tuite, M., Tung, E., Wehbe, R., Weinberg, R., Weiner, R.H., Wiens, R.C., Williford, K., Wollonciej, C., Wu, Y.-H., Yingst, R.A., and Zan, J., 2021, *Perseverance's* Scanning Habitable Environments with Raman and Luminescence for Organics and Chemicals (SHERLOC) investigation: Space Science Reviews, v. 217, doi:10.1007/s11214-021-00812-z.

Bohacs, K.M., Carroll, A.R., Neal, J.E., and Mankiewicz, P.J., 2000, Lake-basin type, source potential, and hydrocarbon character: an integrated sequence-stratigraphic–geochemical framework, *in* Gierlowski-Kordesch, E.H., and Kelts, K.R., eds., Lake Basins Through Space and Time: American Association of Petroleum Geologists, Studies in Geology, v. 46, p. 3–34, doi:10.1306/St46706C1.

Bosak, T., Moore, K.R., Gong, J., and Grotzinger, J.P., 2021, Searching for biosignatures in sedimentary rocks from early Earth and Mars: Nature Reviews Earth and Environment, v. 2, p. 490–506, doi:10.1038/s43017-021-00169-5.

Bramble, M.S., Mustard, J.F., and Salvatore, M.R., 2017, The geological history of Northeast Syrtis Major, Mars: Icarus, v. 293, p. 66–93, doi:10.1016/j.icarus.2017.03.030.

Breuer, D., and Spohn, T., 2003, Early plate tectonics versus single-plate tectonics on Mars: evidence from magnetic field history and crust evolution: Journal of Geophysical Research, Planets, v. 108, no. E7, doi:10.1029/2002JE001999.

Bridge, J.S., and Lunt, I.A., 2006, Depositional models of braided rivers, *in* Sambrook Smith, G.H., Best, J.L., Bristow, C.S., and Petts, G.E., eds., Braided Rivers: Process, Deposits, Ecology and Management: John Wiley and Sons, p. 11–50, doi:10.1002/9781444304374.ch2.

Bristow, C.S., 1993, Sedimentary structures exposed in bar tops in the Brahmaputra River, Bangladesh, *in* Best, J.L., and Bristow, C.S., eds., Braided Rivers: Geological Society of London, Special Publication, v. 75, p. 277–289, doi:10.1144/GSL.SP.1993.075.01.17.

Brown, L.F., and Fisher, W.L., 1977, Seismic-stratigraphic interpretation of depositional systems: examples from Brazilian rift and pull-apart basins, *in* Payton, C.E., ed., Seismic Stratigraphy: Applications to Hydrocarbon Exploration: American Association of Petroleum Geologists, Special Volumes, v. 26, p. 213–248, doi:10.1306/M26490.

Budai, S., Colombera, L., and Mountney, N.P., 2021, Quantitative characterization of the sedimentary architecture of Gilbert-type deltas: Sedimentary Geology, v. 426, no. 106022, doi:10.1016/j.sedgeo.2021.106022.

Burpee, A.P., Slingerland, R.L., Edmonds, D.A., Parsons, D., Best, J., Cederberg, J., McGuffin, A., Caldwell, R., Nijhuis, A., and Royce, J., 2015, Grain-size controls on the morphology and internal geometry of river-dominated deltas: Journal of Sedimentary Research, v. 85, p. 699–714, doi:10.2110/jsr.2015.39.

Butcher, F.E.G., Arnold, N.S., Conway, S.J., Berman, D.C., Davis, J.M., and Balme, M.R., 2024, The internal structure of a debris-covered glacier on Mars revealed by gully incision: Icarus, v. 419, no. 115717, doi:10.1016/j.icarus.2023.115717.

Caldwell, R.L., and Edmonds, D.A., 2014, The effects of sediment properties on deltaic processes and morphologies: a numerical modeling study: Journal of Geophysical Research, Earth Surface, v. 119, p. 961–982, doi:10.1002/2013JF002965.

Caravaca, G., Dromart, G., Mangold, N., Gupta, S., Kah, L.C., Tate, C., Williams, R.M.E., Le Mouélic, S., Gasnault, O., Bell, J.F., III, Beyssac, O., Nuñez, J.I., Randazzo, N., Rice, J., Jr., Crumpler, L.S., Williams, A., Russel, P., Stack, K.M., Farley, K.A., Maurice, S., and Wiens, R.C., 2024, Depositional facies and sequence stratigraphy of Kodiak Butte, western delta of Jezero Crater, Mars: Journal of Geophysical Research, Planets, v. 129, no. e2023JE008205, doi:10.1029/2023JE008205.

Carling, P.A., Martini, I.P., Herget, J., Borodavko, P., and Parnachov, S., 2009, Megaflood sedimentary valley fill: Altai Mountains, Siberia, *in* Burr, D.M., Carling, P.A., and Baker, V.R., eds., Megaflooding on Earth and Mars: Cambridge University Press, p. 243–264, doi:10.1017/CBO9780511635632.013.

Carling, P., Bristow, C., and Litvinov, A., 2016, Ground-penetrating radar stratigraphy and dynamics of megaflood gravel dunes: Geological Society of London, Journal, v. 173, p. 550–559, doi:10.1144/jgs2015-119.

Catuneanu, O., 2015, Sequence stratigraphy: Reference Module in Earth Systems and Environmental Sciences, Elsevier, 18 p, doi:10.1016/B978-0-12-409548-9.09536-1.

Catuneanu, O., 2022, Principles of Sequence Stratigraphy, Second Edition: Elsevier, 486 p., doi:10.1016/C2009-0-19362-5.

Cohen, S., Wan, T., Islam, M.T., and Syvitski, J.P.M., 2018, Global river slope: a new geospatial dataset and global-scale analysis: Journal of Hydrology, v. 563, p. 1057–1067, doi:10.1016/j.jhydrol.2018.06.066.

Cole, G., Jerrett, R., and Watkinson, M.P., 2021, A stratigraphic example of the architecture and evolution of shallow water mouth bars: Sedimentology, v. 68, p. 1227–1254, doi:10.1111/sed.12825.

Cornwall, C., Bourke, M.C., Jackson, D.W.T., and Cooper, J.A.G., 2018a, Aeolian slipface dynamics and grainflow morphologies on Earth and Mars: Icarus, v. 314, p. 311–326, doi:10.1016/j.icarus.2018.05.033.

Cornwall, C., Jackson, D.W.T., Bourke, M.C., and Cooper, J.A.G., 2018b, Morphometric analysis of slipface processes of an aeolian dune: implications for grain-flow dynamics: Sedimentology, v. 65, p. 2034–2054, doi:10.1111/sed.12456.

Dehouck, E., Forni, O., Quantin-Nataf, C., Beck, P., Mangold, N., Beyssac, O., Royer, C., Clavé, E., Johnson, J.R., Mandon, L., Poulet, F., Udry, A., Lopes-Reyes, G., Caravaca, G., Maurice, S., Wiens, R.C., Stack, K.M., Anderson, R.B., Bernard, S., Bosak, T., Broz, A.P., Castro, K., Clegg, S.M., Cousin, A., Dromat, G., Farley, K.A., Fouchet, T., Frydenvang, J., Gabriel, T.S.J., Gasda, P., Gibbons, E., Horgan, B.H.N., Hurowitz, J.A., Kalucha, H., Lasue, J., Le Mouélic, S., Madariaga, J.M., Meslin, P.-Y., Nachon, M., Nuñez, J.I., Pilleri, P., Pilorget, C., Rice, J.W., Russell, P.S., Schröder, S., Shuster, D.L., Siebach, K.L., Simon, J.I., Weiss, B.P., William, A.J., and the SuperCam team, 2024, Chemostratigraphy and mineralogy of the Jezero western fan as seen by the SuperCam instrument: evidence for a complex aqueous history and variable alteration conditions: Tenth International Conference on Mars, Pasadena, California, n. 3364, https://www.hou.usra.edu/meetings/tenthmars2024/pdf/3364.pdf.

Dickson, J.L., Ehlmann, B.L., Kerber, L.H., and Fassett, C.I., 2023, Release of the global CTX mosaic of Mars: an experiment in information-preserving image data processing: 54th Lunar and Planetary Science Conference, The Woodlands, Texas, n. 2353, https://www.hou.usra.edu/meetings/lpsc2023/pdf/2353.pdf.

Dodd, T.J.H., McCarthy, D.J., Amy, L., Plenderleith, G.E., and Clarke, S.M., 2022, Hybrid even bed character and distribution in the context of ancient deep-lacustrine fan models: Sedimentology, v. 69, p. 1891–1926, doi:10.1111%2Fsed.12979.

Edgett, K.S., and Sarkar, R., 2021, Recognition of sedimentary rock occurrences in satellite and aerial images of other worlds: insights from Mars: Remote Sensing, v. 13, no. 4296, doi:10.3390/rs13214296.

Ehlmann, B.L., Mustard, J.F., Fassett, C.I., Schon, S.C., Head, J.W., Des Marais, D.J., Grant, J.A., and Murchie, S.L., 2008, Clay minerals in delta deposits and organic preservation potential on Mars: Nature Geoscience, v. 1, p. 355–358, doi:10.1038/ngeo207.

Elekes, F., and Parteli, E.J.R., 2021, An expression for the angle of repose of dry cohesive granular materials on Earth and in planetary environments: National Academy of Sciences [U.S.A.], Proceedings, v. 118, no. e2107965118, doi:10.1073/pnas.2107965118.

Embry, A.F., and Johannessen, E.P., 2017, Two approaches to sequence stratigraphy, *in* Montenari, M., ed., Volume 2: Advances in Sequence Stratigraphy, Stratigraphy and Timescales: Elsevier, p. 85–118, doi:10.1016/bs.sats.2017.08.001.

Farley, K.A., and Stack, K.M., 2023, Mars 2020 Initial Reports Volume 2: Delta Front Campaign: Planetary Data System (PDS) Geosciences (GEO) Node, doi:10.17189/49zd-2k55.

Farley, K.A., and Stack, K.M., 2024a, Mars 2020 Initial Reports Volume 3: Fan Top Campaign: Planetary Data System (PDS) Geosciences (GEO) Node, doi:10.17189/68tf-re13.

Farley, K.A., and Stack, K.M., 2024b, Mars 2020 Initial Reports Volume 4: Jezero Margin Campaign: Planetary Data System (PDS) Geosciences (GEO) Node, doi:10.17189/mzx3-k371.

Farley, K.A., Williford, K.H., Stack, K.M., Bhartia, R., Chen, A., de la Torre, M., Hand, K., Goreva, Y., Herd, C.D.K., Hueso, R., Liu, Y., Maki, J.N., Martinez, G., Moeller, R.C., Nelessen, A., Newman, C.E., Nunes, D., Ponce, A., Spanovich, N., Willis, P.A., Beegle, L.W., Bell, J.F., Brown, A.J., Hamran, S.-E., Hurowitz, J.A., Maurice, S., Paige, D.A., Rodriguez-Manfredi, J.A., Schulte, M., and Wiens, R.C., 2020, Mars 2020 Mission Overview: Space Science Reviews, v. 216, no. 142, doi:10.1007/s11214-020-00762-y.

Farley, K.A., Stack, K.M., Shuster, D.L., Horgan, B.H.N., Hurowitz, J.A., Tarnas, J.D., Simon, J.I., Sun, V.Z., Scheller, E.L., Moore, K.R., McLennan, S.M., Vasconcelos, P.M., Wiens, R.C., Treiman, A.H., Mayhew, L.E., Beyssac, O., Kizovski, T.V., Tosca, N.J., Williford, K.H., Crumpler, L.S., Beegle, L.W., Bell, J.F., Ehlmann, B.L., Liu, Y., Maki, J.N., Schmidt, M.E., Allwood, A.C., Amundsen, H.E.F., Bhartia, R., Bosak, T., Brown, A.J., Clark, B.C., Cousin, A., Forni, O., Gabriel, T.S.J., Goreva, Y., Gupta, S., Hamran, S.-E., Herd, C.D.K., Hickman-Lewis, K., Johnson, J.R., Kah, L.C., Kelemen, P.B., Kinch, K.B., Mandon, L., Mangold, N., Quantin-Nataf, C., Rice, M.S., Russell, P.S., Sharma, S., Siljeström, S., Steele, A., Sullivan, R., Wadhwa, M., Weiss, B.P., Williams, A.J., Wogsland, B.V., Willis, P.A., Acosta-Maeda, T.A., Beck, P., Benzerara, K., Bernard, S., Burton, A.S., Cardarelli, E.L., Chide, B., Clavé, E., Cloutis, E.A., Cohen, B.A., Czaja, A.D., Debaille, V., Dehouck, E., Fairén, A.G., Flannery, D.T., Fleron, S.Z., Fouchet, T., Frydenvang, J., Garczynski, B.J., Gibbons, E.F., Hausrath, E.M., Hayes, A.G., Henneke, J., Jørgensen, J.L., Kelly, E.M., Lasue, J., Le Mouélic, S., Madariaga, J.M., Maurice, S., Merusi, M., Meslin, P.-Y., Milkovich, S.M., Million, C.C., Moeller, R.C., Núñez, J.I., Ollila, A.M., Paar, G., Paige, D.A., Pedersen, D.A.K., Pilleri, P., Pilorget, C., Pinet, P.C., Rice, J.W., Royer, C., Sautter, V., Schulte, M., Sephton, M.A., Sharma, S.K., Sholes, S.F., Spanovich, N., St. Clair, M., Tate, C.D., Uckert, K., VanBommel, S.J., Yanchilina, A.G., and Zorzano, M.-P., 2022, Aqueously altered igneous rocks sampled on the floor of Jezero Crater, Mars: Science, v. 377, no. eabo2196, doi:10.1126/science.abo2196.

Fassett, C.I., and Goudge, T.A., 2021, Modeling the hydrodynamics, sediment transport, and valley incision of outlet-forming floods from Martian crater lakes: Journal of Geophysical Research, Planets, v. 126, no. e2021JE006979, doi:10.1029/2021JE006979.

Fassett, C.I., and Head, J.W., III, 2005, Fluvial sedimentary deposits on Mars: ancient deltas in a crater lake in the Nili Fossae region: Geophysical Research Letters, v. 32, no. L14201, doi:10.1029/2005GL023456.

Fergason, R.L., Hare, T.M., and Laura, J., 2018, Mars MGS MOLA-MEX HRSC Blended DEM Global 200m: U.S. Geological Survey, Astropedia, https://astrogeology.usgs.gov/search/map/mars_mgs_mola_mex_hrsc_blended_dem_global_200m.

Fergason, R.L., Hare, T.M., Mayer, D.P., Galuszka, D.M., Redding, B.L., Smith, E.D., Shinaman, J.R., Cheng, Y., and Otero, R.E., 2020, Mars 2020 terrain relative navigation flight product generation: digital terrain model and orthorectified image mosaics: 51st Lunar and Planetary Science Conference, The Woodlands, Texas, https://www.hou.usra.edu/meetings/lpsc2020/pdf/2020.pdf.

Galloway, W.E., 1989, Genetic stratigraphic sequences in basin analysis I: architecture and genesis of flooding-surface bounded depositional units: American Association of Petroleum Geologists, Bulletin, v. 73, p. 125–142, doi:10.1306/703C9AF5-1707-11D7-8645000102C1865D.

Gasnault, O., Virmontois, C., Maurice, S., Wiens, R.C., Mouélic, S.L., Bernardi, P., Forni, O., Pilleri, P., Daydou, Y., Rapin, W., and Caïs, P., 2021, What SuperCam will see: the remote micro-imager aboard *Perseverance*: 52nd Lunar and Planetary Science Conference, The Woodlands, Texas, https://www.hou.usra.edu/meetings/lpsc2021/pdf/2248.pdf.

Gilles, S., 2024, Rasterio: geospatial raster I/O for {Python} programmers, https://rasterio.readthedocs.io/en/stable/.

Gobo, K., Ghinassi, M., and Nemec, W., 2015, Gilbert-type deltas recording short-term base-level changes: delta-brink morphodynamics and related foreset facies: Sedimentology, v. 62, p. 1923–1949, doi:10.1111/sed.12212.

Goudge, T.A., Mustard, J.F., Head, J.W., Fassett, C.I., and Wiseman, S.M., 2015, Assessing the mineralogy of the watershed and fan deposits of the Jezero Crater paleolake system, Mars: Journal of Geophysical Research, Planets, v. 120, p. 775–808, doi:10.1002/2014JE004782.

Goudge, T.A., Milliken, R.E., Head, J.W., Mustard, J.F., and Fassett, C.I., 2017, Sedimentological evidence for a deltaic origin of the western fan deposit in Jezero Crater, Mars and implications for future exploration: Earth and Planetary Science Letters, v. 458, p. 357–365, doi:10.1016/j.epsl.2016.10.056.

Goudge, T.A., Mohrig, D., Cardenas, B.T., Hughes, C.M., and Fassett, C.I., 2018, Stratigraphy and paleohydrology of delta channel deposits, Jezero Crater, Mars: Icarus, v. 301, p. 58–75, doi:10.1016/j.icarus.2017.09.034.

Grotzinger, J.P., and Milliken, R.E., 2012, The sedimentary rock record of Mars: distributions, origins, and global stratigraphy, *in* Grotzinger, J.P., and Milliken, R.E., eds., Sedimentary Geology of Mars: SEPM, Special Publication 102, p. 1–48, doi:10.2110/pec.12.102.

Grotzinger, J.P., Arvidson, R.E., Bell, J.F., Calvin, W., Clark, B.C., Fike, D.A., Golombek, M., Greeley, R., Haldemann, A., Herkenhoff, K.E., Jolliff, B.L., Knoll, A.H., Malin, M., McLennan, S.M., Parker, T., Soderblom, L., Sohl-Dickstein, J.N., Squyres, S.W., Tosca, N.J., and Watters, W.A., 2005, Stratigraphy and sedimentology of a dry to wet eolian depositional system, Burns formation, Meridiani Planum, Mars: Earth and Planetary Science Letters, v. 240, p. 11–72, doi:10.1016/j.epsl.2005.09.039.

Gupta, S., Stack, K.M., Mangold, N., Ives, L.R.W., Gwizd, S., Caravaca, G., Williams, R.M.E., Randazzo, N., Williams, A.J., Russell, P., Horgan, B.H.N., Siebach, K.L., Tice, M.M., Hurowitz, J.A., Barnes, R., Tate, C., Núñez, J.I., Scholes, S., Kah, L.C., Minitti, M.E., Dromart, G., Bell, J.F., Maki, J., Paar, G., Annex, A.M., Weiss, B., Beyssac, O., Frydenvang, J., Nachon, M., Kronyak, R., Sun, V.Z., Jones, A.J., Shuster, D.L., Simon, J.I., Lamb, M.P., Grotzinger, J., Mouélic, S.L., Gasnault, O., Wiens, R.C., Maurice, S., and Farley, K.A., 2024, Going with the flow: sedimentary evolution of the Jezero western fan, Mars: 55th Lunar and Planetary Science Conference, The Woodlands, Texas, https://www.hou.usra.edu/meetings/lpsc2024/pdf/2607.pdf.

Gwizd, S., Fedo, C., Grotzinger, J., Banham, S., Rivera-Hernández, F., Gupta, S., Stack, K.M., Edgar, L.A., Vasavada, A.R., Davis, J., and Kah, L.C., 2024a, Evolution of a lake margin recorded in the Sutton Island member of the Murray formation, Gale Crater, Mars: Journal of Geophysical Research, Planets, v. 129, no. e2023JE007919, doi:10.1029/2023JE007919.

Gwizd, S., Stack, K.M., Ives, L., Gupta, S., Randazzo, N., Lamb, M., Cavallo, N., Williams, N., Crumpler, L., Rice, J., Horgan, B., Kah, L.C., Cianciolo, O., Quantin-Nataf, C., Beyssac, O., Vaughan, A., Simon, J.I., Siebach, K., Nachon, M., Kronyak, R., Sun, V., Sholes, S., Shuster, D., and Bell, J., 2024b, Depositional history of the upper sequence of the western fan: evidence for late-stage fluvial and potential igneous activity, Jezero Crater, Mars: 55th Lunar and Planetary Science Conference, The Woodlands, Texas, https://www.hou.usra.edu/meetings/lpsc2024/pdf/2117.pdf.

Hamran, S.E., and Paige, D.A., 2021, Mars 2020 RIMFAX bundle: Planetary Data System (PDS) Geosciences (GEO) Node, doi:10.17189/1522644.

Hamran, S.-E., Paige, D.A., Amundsen, H.E.F., Berger, T., Brovoll, S., Carter, L., Damsgård, L., Dypvik, H., Eide, J., Eide, S., Ghent, R., Helleren, Ø., Kohler, J., Mellon, M., Nunes, D.C., Plettemeier, D., Rowe, K., Russell, P., and Øyan, M.J., 2020, Radar imager for Mars' subsurface experiment: RIMFAX: Space Science Reviews, v. 216, no. 128, doi:10.1007/s11214-020-00740-4.

Herbert, C.M., Alexander, J., Amos, K.J., and Fielding, C.R., 2020, Unit bar architecture in a highly-variable fluvial discharge regime: examples from the Burdekin River, Australia: Sedimentology, v. 67, p. 576–605, doi:10.1111/sed.12655.

Herd, C.D.K., Bosak, T., Hausrath, E.M., Hickman-Lewis, K., Mayhew, L.E., Shuster, D.L., Siljeström, S., Simon, J.I., Weiss, B.P., Wadhwa, M., Zorzano, M.-P., Maki, J.N., Farley, K.A., and Stack, K.M., 2025, Sampling Mars: geologic context and preliminary characterization of samples collected by the NASA Mars 2020 *Perseverance* Rover Mission: National Academy of Sciences [U.S.A], Proceedings, v. 122, e2404255121, doi:10.1073/pnas.2404255121.

Hiesinger, H., and Head, J.W., 2004, The Syrtis Major volcanic province, Mars: synthesis from Mars Global Surveyor data: Journal of Geophysical Research, v. 109, no. E01004, doi:10.1029/2003JE002143.

Hough, B.K., 1969, Basic Soils Engineering: Ronald Press Company, 590 p.

Jodhpurkar, M.J., Bell, J.F., III, Gupta, S., Horgan, B., Gwizd, S., Caravaca, G., and Randazzo, N., 2024, Mapping and characterizing the northern fan deposits in Jezero Crater, Mars: Journal of Geophysical Research, Planets, v. 129, no. e2024JE008308, doi:10.1029/2024JE008308.

Jordahl, K., Bossche, J.V., den Fleischmann, M., Wasserman, J., McBride, J., Gerard, J., Tratner, J., Perry, M., Badaracco, A.G., Farmer, C., Hjelle, G.A., Snow, A.D., Cochran, M., Gillies, S., Culbertson, L., Bartos, M., Eubank, N., Maxalbert, B.A., Rey, S., Ren, C., Arribas-Bel, D., Wasser, L., Wolf, L.J., Journois, M., Wilson, J., Greenhall, A., Holdgraf, C., Filipe, and Leblanc, F., 2020, geopandas/geopandas: v0.8.1, doi:10.5281/zenodo.3946761.

Kildaras, A., Horgan, B., Vaughan, A.F., Rice, M., Johnson, J.R., Simon, J.I., Orenstein, B., Kathir, B.S., Flannery, D.T., and Bell, J.F., III, 2024, Diversity of fluvially transported clasts in the Jezero western fan using Mastcam-Z: Tenth International Conference on Mars 2024, Pasadena, California, https://www.hou.usra.edu/meetings/tenthmars2024/pdf/3223.pdf.

Kite, E.S., 2019, Geologic constraints on early Mars climate: Space Science Reviews, v. 215, doi:10.1007/s11214-018-0575-5.

Kleinhans, M.G., 2004, Sorting in grain flows at the lee side of dunes: Earth-Science Reviews, v. 65, p. 75–102, doi:10.1016/S0012-8252(03)00081-3.

Kleinhans, M.G., 2005, Grain-size sorting in grainflows at the lee side of deltas: Sedimentology, v. 52, p. 291–311, doi:10.1111/j.1365-3091.2005.00698.x.

Korus, J.T., Joeckel, R.M., and Tucker, S.T., 2020, Genesis of giant, bouldery bars in a Miocene gravel-bed river: insights from outcrop sedimentology, UAS-SfM

photogrammetry, and GPR: Journal of Sedimentary Research, v. 90, p. 27–47, doi:10.2110/jsr.2020.3.

Kronyak, R.E., Stack-Morgan, K.M., Sholes, S.F., Sun, V.Z., Gupta, S., Shuster, D.L., and Caravaca, G., 2023, Geomorphology and relative ages of channel belt deposits in Jezero's western delta. Presented at the 54th Lunar and Planetary Science Conference (LPSC 2023), no. 2067, https://hal.science/hal-04044942v1/file/2067.pdf.

Lapôtre, M.G.A., and Ielpi, A., 2020, The pace of fluvial meanders on Mars and implications for the western delta deposits of Jezero Crater: American Geophysical Union, Advances, v. 1, no. e2019AV000141, doi:10.1029/2019AV000141.

Lapôtre, M.G.A., O'Rourke, J.G., Schaefer, L.K., Siebach, K.L., Spalding, C., Tikoo, S.M., and Wordsworth, R.D., 2020, Probing space to understand Earth: Nature Reviews Earth and Environment, v. 1, p. 170–181, doi:10.1038/s43017-020-0029-y.

Lapôtre, M.G.A., Bishop, J.L., Ielpi, A., Lowe, D.R., Siebach, K.L., Sleep, N.H., and Tikoo, S.M., 2022, Mars as a time machine to Precambrian Earth: Geological Society of London, Journal, v. 179, no. jgs2022-047, doi:10.1144/jgs2022-047.

Laronne, J., Garcia, C., and Reid, I., 2001, Mobility of patch sediment in gravel bed streams: patch character and its implications for bedload, *in* Mosley, M.P., ed., Gravel-Bed Rivers V: Wellington, New Zealand Hydrological Society, p. 249–289.

Le Mouélic, S., Gasnault, O., Pilleri, P., Caravaca, G., Mangold, N., Maurice, S., Herkenhoff, K., Gabriel, T., Wiens, R.C., Newsom, H.E., Gallegos, Z.E., and Mcconnochie, T.H., 2024, Empirical correction of bright halos in ChemCam and SuperCam RMI long distance mosaics, 55th Lunar and Planetary Science Conference, Lunar and Planetary Institute, The Woodlands, Texas, no. 1318, https://www.hou.usra.edu/meetings/lpsc2024/pdf/1318.pdf.

Liu, Y., Tice, M.M., Schmidt, M.E., Treiman, A.H., Kizovski, T.V., Hurowitz, J.A., Allwood, A.C., Henneke, J., Pedersen, D.A.K., VanBommel, S.J., Jones, M.W.M., Knight, A.L., Orenstein, B.J., Clark, B.C., Elam, W.T., Heirwegh, C.M., Barber, T., Beegle, L.W., Benzerara, K., Bernard, S., Beyssac, O., Bosak, T., Brown, A.J., Cardarelli, E.L., Catling, D.C., Christian, J.R., Cloutis, E.A., Cohen, B.A., Davidoff, S., Fairén, A.G., Farley, K.A., Flannery, D.T., Galvin, A., Grotzinger, J.P., Gupta, S., Hall, J., Herd, C.D.K., Hickman-Lewis, K., Hodyss, R.P., Horgan, B.H.N., Johnson, J.R., Jørgensen, J.L., Kah, L.C., Maki, J.N., Mandon, L., Mangold, N., McCubbin, F.M., McLennan, S.M., Moore, K., Nachon, M., Nemere, P., Nothdurft, L.D., Núñez, J.I., O'Neil, L., Quantin-Nataf, C.M., Sautter, V., Shuster, D.L., Siebach, K.L., Simon, J.I., Sinclair, K.P., Stack, K.M., Steele, A., Tarnas, J.D., Tosca, N.J., Uckert, K., Udry, A., Wade, L.A., Weiss, B.P., Wiens, R.C., Williford, K.H., and Zorzano, M.-P., 2022, An olivine cumulate outcrop on the floor of Jezero Crater, Mars: Science, v. 377, p. 1513–1519, doi:10.1126/science.abo2756.

Long, D.G.F., and Lowey, G.M., 2006, Anatomy of a late Jurassic Gilbert-type delta in basal strata of the Tantalus Formation, Whitehorse trough, Yukon, *in* Emond, D.S., Bradshaw, G.D., Lewis, L.L., and Weston, L.H., eds., Yukon Exploration and Geology 2005: Yukon Geological Survey, p. 195–205, https://data.geology.gov.yk.ca/Reference/42283.

Malin, M.C., and Edgett, K.S., 2000, Sedimentary rocks of early Mars: Science, v. 290, no. 1927–1937, doi:10.1126/science.290.5498.1927.

Mandon, L., Quantin-Nataf, C., Thollot, P., Mangold, N., Lozac'h, L., Dromart, G., Beck, P., Dehouck, E., Breton, S., Millot, C., and Volat, M., 2020, Refining the age, emplacement and alteration scenarios of the olivine-rich unit in the Nili Fossae region, Mars: Icarus, v. 336, no. 113436, doi:10.1016/j.icarus.2019.113436.

Mangold, N., Dromart, G., Ansan, V., Salese, F., Kleinhans, M.G., Massé, M., Quantin-Nataf, C., and Stack, K.M., 2020, Fluvial regimes, morphometry, and Age of Jezero Crater paleolake inlet valleys and their exobiological significance for the 2020 Rover mission landing site: Astrobiology, v. 20, p. 994–1013, doi:10.1089/ast.2019.2132.

Mangold, N., Gupta, S., Gasnault, O., Dromart, G., Tarnas, J.D., Sholes, S.F., Horgan, B., Quantin-Nataf, C., Brown, A.J., Le Mouélic, S., Yingst, R.A., Bell, J.F., Beyssac, O., Bosak, T., Calef, F., Ehlmann, B.L., Farley, K.A., Grotzinger, J.P., Hickman-Lewis, K., Holm-Alwmark, S., Kah, L.C., Martinez-Frias, J., McLennan, S.M., Maurice, S., Nuñez, J.I., Ollila, A.M., Pilleri, P., Rice, J.W., Rice, M., Simon, J.I., Shuster, D.L., Stack, K.M., Sun, V.Z., Treiman, A.H., Weiss, B.P., Wiens, R.C., Williams, A.J., Williams, N.R., and Williford, K.H., 2021, *Perseverance* rover reveals an ancient delta-lake system and flood deposits at Jezero Crater, Mars: Science, v. 374, p. 711–717, doi:10.1126/science.abl4051.

Mangold, N., Caravaca, G., Gupta, S., Williams, R.M.E., Dromart, G., Gasnault, O., Le Mouélic, S., Paar, G., Bell, J., Beyssac, O., Carlot, N., Cousin, A., Dehouck, E., Horgan, B., Kah, L.C., Lasue, J., Maurice, S., Núñez, J.I., Shuster, D., Stack, K.M., Weiss, B.P., and Wiens, R.C., 2024, Architecture of fluvial and deltaic deposits exposed along the eastern edge of the western fan of Jezero Crater, Mars: Journal of Geophysical Research, Planets, v. 129, no. e2023JE008204, doi:10.1029/2023JE008204.

Maurice, S., Wiens, R.C., Bernardi, P., Caïs, P., Robinson, S., Nelson, T., Gasnault, O., Reess, J.-M., Deleuze, M., Rull, F., Manrique, J.-A., Abbaki, S., Anderson, R.B., André, Y., Angel, S.M., Arana, G., Battault, T., Beck, P., Benzerara, K., Bernard, S., Berthias, J.-P., Beyssac, O., Bonafous, M., Bousquet, B., Boutillier, M., Cadu, A., Castro, K., Chapron, F., Chide, B., Clark, K., Clavé, E., Clegg, S., Cloutis, E., Collin, C., Cordoba, E.C., Cousin, A., Dameury, J.-C., D'Anna, W., Daydou, Y., Debus, A., Deflores, L., Dehouck, E., Delapp, D., De Los Santos, G., Donny, C., Doressoundiram, A., Dromart, G., Dubois, B., Dufour, A., Dupieux, M., Egan, M., Ervin, J., Fabre, C., Fau, A., Fischer, W., Forni, O., Fouchet, T., Frydenvang, J., Gauffre, S., Gauthier, M., Gharakanian, V., Gilard, O., Gontijo, I., Gonzalez, R., Granena, D., Grotzinger, J., Hassen-Khodja, R., Heim, M., Hello, Y., Hervet, G., Humeau, O., Jacob, X., Jacquinod, S., Johnson, J.R., Kouach, D., Lacombe, G., Lanza, N., Lapauw, L., Laserna, J., Lasue, J., Le Deit, L., Le Mouélic, S., Le Comte, E., Lee, Q.-M., Legett, C., Leveille, R., Lewin, E., Leyrat, C., Lopez-Reyes, G., Lorenz, R., Lucero, B., Madariaga, J.M., Madsen, S., Madsen, M., Mangold, N., Manni, F., Mariscal, J.-F., Martinez-Frias, J., Mathieu, K., Mathon, R., McCabe, K.P., McConnochie, T., McLennan, S.M., Mekki, J., Melikechi, N., Meslin, P.-Y., Micheau, Y., Michel, Y., Michel, J.M., Mimoun, D., Misra, A., Montagnac, G., Montaron, C., Montmessin, F., Moros, J., Mousset, V., Morizet, Y., Murdoch, N., Newell, R.T., Newsom, H., Nguyen Tuong, N., Ollila, A.M., Orttner, G., Oudda, L., Pares, L., Parisot, J., Parot, Y., Pérez, R., Pheav, D., Picot, L., Pilleri, P., Pilorget, C., Pinet, P., Pont, G., Poulet, F., Quantin-Nataf, C., Quertier, B., Rambaud, D., Rapin, W., Romano, P., Roucayrol, L., Royer, C., Ruellan, M., Sandoval, B.F., Sautter, V., Schoppers, M.J., Schröder, S., Seran, H.-C., Sharma, S.K., Sobron, P., Sodki, M., Sournac, A., Sridhar, V., Standarovsky, D., Storms, S., Striebig, N., Tatat, M., Toplis, M., Torre-Fdez, I., Toulemont, N., Velasco, C., Veneranda, M., Venhaus, D., Virmontois, C., Viso, M., Willis, P., and Wong, K.W., 2021, The SuperCam instrument suite on the Mars 2020 rover: science objectives and mast-unit description: Space Science Reviews, v. 217, doi:10.1007/s11214-021-00807-w.

McEwen, A.S., Eliason, E.M., Bergstrom, J.W., Bridges, N.T., Hansen, C.J., Delamere, W.A., Grant, J.A., Gulick, V.C., Herkenhoff, K.E., Keszthelyi, L., Kirk, R.L., Mellon, M.T., Squyres, S.W., Thomas, N., and Weitz, C.M., 2007, Mars Reconnaissance Orbiter's High Resolution Imaging Science Experiment (HiRISE). Journal of Geophysical Research, Planets, v. 112, no. E05S02, doi:10.1029/2005JE002605.

McLennan, S.M., Grotzinger, J.P., Hurowitz, J.A., and Tosca, N.J., 2019, The sedimentary cycle on early Mars: Annual Review of Earth and Planetary Sciences, v. 47, p. 91–118, doi:10.1146/annurev-earth-053018-060332.

Middleton, G.V., and Hampton, M.A., 1973, Part I. Sediment gravity flows: mechanics of flow and deposition, *in* Middleton, G.V., and Bouma, A.H., eds., Turbidites and Deep-Water Sedimentation: Lecture Notes for a Short Course: SEPM, Pacific Section, p. 1–38.

Mikes, D., and Geel, C.R., 2006, Standard facies models to incorporate all heterogeneity levels in a reservoir model: Marine and Petroleum Geology, v. 23, p. 943–959, doi:10.1016/j.marpetgeo.2005.06.007.

Milliken, R.E., Mustard, J.F., and Goldsby, D.L., 2003, Viscous flow features on the surface of Mars: Observations from high-resolution Mars Orbiter Camera (MOC) images: Journal of Geophysical Research, Planets, v. 108, v. E6, no. 5057, doi:10.1029/2002JE002005.

Moran, M.G., Holbrook, J., Lensky, N.G., Ben Moshe, L., Mor, Z., Eyal, H., and Enzel, Y., 2023, Century-scale sequences and density-flow deltas of the late Holocene and modern Dead Sea coast, Israel: Sedimentology, v. 70, p. 1945–1980, doi:10.1111/sed.13101.

Mortimer, E., Gupta, S., and Cowie, P., 2005, Clinoform nucleation and growth in coarse-grained deltas, Loreto basin, Baja California Sur, Mexico: a response to episodic accelerations in fault displacement: Basin Research, v. 17, p. 337–359, doi:10.1111/j.1365-2117.2005.00273.x.

Mumpy, A.J., Jol, H.M., Kean, W.F., and Isbell, J.L., 2007, Architecture and sedimentology of an active braid bar in the Wisconsin River based on 3-D ground penetrating radar, *in* Baker, G.S., and Jol, H.M., eds., Stratigraphic Analyses Using GPR: Geological Society of America, Special Paper, v. 432, p. 111–132, doi:10.1130/2007.2432(09).

Murchie, S.L., Seelos, F.P., Hash, C.D., Humm, D.C., Malaret, E., McGovern, J.A., Choo, T.H., Seelos, K.D., Buczkowski, D.L., Morgan, M.F., Barnouin-Jha, O.S., Nair, H., Taylor, H.W., Patterson, G.W., Harvel, C.A., Mustard, J.F., Arvidson, R.E., McGuire, P., Smith, M.D., Wolff, M.J., Titus, T.N., Bibring, J.-P., and Poulet, F., 2009, Compact Reconnaissance Imaging Spectrometer for Mars investigation and data set from the Mars Reconnaissance Orbiter's primary science phase: Journal of Geophysical Research, Planets, v. 114, no. E00D07, doi:10.1029/2009JE003344.

Nakashima, H., Shioji, Y., Kobayashi, T., Aoki, S., Shimizu, H., Miyasaka, J., and Ohdoi, K., 2011, Determining the angle of repose of sand under low-gravity conditions using discrete element method: Journal of Terramechanics, v. 48, p. 17–26, doi:10.1016/j.jterra.2010.09.002.

Nanson, G.C., 1980, Point bar and floodplain formation of the meandering Beatton River, northeastern British Columbia, Canada: Sedimentology, v. 27, p. 3–29, doi:10.1111/j.1365-3091.1980.tb01155.x.

Nemec, W., 1990, Aspects of sediment movement on steep delta slopes, *in* Colella, A., and Prior, D.B., eds., Coarse-Grained Deltas: John Wiley and Sons, p. 29–73, doi:10.1002/9781444303858.ch3.

Nittrouer, J.A., Shaw, J., Lamb, M.P., and Mohrig, D., 2012, Spatial and temporal trends for water-flow velocity and bed-material sediment transport in the lower Mississippi River: Geological Society of America, Bulletin, v. 124, p. 400–414, doi:10.1130/B30497.1.

Núñez, J.I., Johnson, J.R., Rice, M.S., Horgan, B., Vaughan, A., Garczynski, B.J., Kildaras, A., Million, C.C., St. Clair, M., Merusi, M., Hayes, A.G., Tate, C., Gupta, S., Barnes, R., Kah, L.C., Maki, J., Bell, J.F., III, Benison, K.C., Brown, A., Hurowitz, J., Mandon, L., and Russell, P., 2024, Spectral diversity of fluvio-deltaic deposits in the delta fan in Jezero Crater, Mars as seen with the Marscam-Z on Mars 2020: Tenth International Conference on Mars, Pasadena, California, https://www.hou.usra.edu/meetings/tenthmars2024/pdf/3508.pdf.

Orton, G.J., and Reading, H.G., 1993, Variability of deltaic processes in terms of sediment supply, with particular emphasis on grain size: Sedimentology, v. 40, p. 475–512, doi:10.1111/j.1365-3091.1993.tb01347.x.

Paige, D.A., Hamran, S.-E., Amundsen, H.E.F., Berger, T., Russell, P., Kakaria, R., Mellon, M.T., Eide, S., Carter, L.M., Casademont, T.M., Nunes, D.C., Shoemaker, E.S., Plettemeier, D., Dypvik, H., Holm-Alwmark, S., and Horgan, B.H.N., 2024, Ground penetrating radar observations of the contact between the western delta and the crater floor of Jezero Crater, Mars: Science Advances, v. 10, no. eadi8339, doi:10.1126/sciadv.adi8339.

Paola, C., and Seal, R., 1995, Grain size patchiness as a cause of selective deposition and downstream fining: Water Resources Research, v. 31, p. 1395–1407, doi:10.1029/94WR02975.

Perry, M., 2024, rasterstats, https://pythonhosted.org/rasterstats/.

Phua, Y.Y., Ehlmann, B.L., Siljeström, S., Czaja, A.D., Beck, P., Connell, S., Wiens, R.C., Jakubek, R.S., Williams, R.M.E., Zorzano, M., Minitti, M.E., Pascuzzo, A.C., Hand, K.P., Bhartia, R., Kah, L.C., Mandon, L., Razzell Hollis, J., Scheller, E.L., Sharma, S., Steele, A., Uckert, K., Williford, K.H., and Yanchilina, A.G., 2024, Characterizing hydrated sulfates and altered phases in Jezero Crater fan and floor geologic units with SHERLOC on Mars 2020: Journal of Geophysical Research, Planets, v. 129, no. e2023JE008251, doi:10.1029/2023JE008251.

Pickering, K.T., Clark, J.D., Smith, R.D.A., Hiscott, R.N., Ricci Lucchi, F., and Kenyon, N.H., 1995, Architectural element analysis of turbidite systems, and selected topical problems for sand-prone deep-water systems, *in* Pickering, K.T., Hiscott, R.N., Kenyon, N.H., Ricci Lucchi, F., and Smith, R.D.A., eds., Atlas of Deep Water Environments: Dordrecht, Springer, p. 1–10, doi:10.1007/978-94-011-1234-51.

Pohlman, N.A., Severson, B.L., Ottino, J.M., and Lueptow, R.M., 2006, Surface roughness effects in granular matter: influence on angle of repose and the absence of segregation: Physical Review E, v. 73, no. 031304, doi:10.1103/PhysRevE.73.031304.

Posamentier, H.W., and Allen, G.P., 1999, Siliciclastic Sequence Stratigraphy: Concepts and Applications: SEPM, Concepts in Sedimentology and Paleontology, v. 7, 210 p, doi:10.2110/csp.99.07.

Posamentier, H.W., and Morris, W.R., 2000, Aspects of the stratal architecture of forced regressive deposits, *in* Hunt, D., and Gawthorpe, R.L., eds., Sedimentary Responses to Forced Regressions: Geological Society of London, Special Publication 72, p. 19–46, doi:10.1144/GSL.SP.2000.172.01.02.

Preston, S.L., Siebach, K.L., Lapôtre, M.G.A., and Banham, S.G., 2024, Grain size measurements of the eolian Stimson formation, Gale Crater, Mars and implications for sand provenance and paleoatmospheric conditions: Journal of Geophysical Research, Planets, v. 129, no. e2024JE008369, doi:10.1029/2024JE008369.

Qayyum, F., Betzler, C., and Catuneanu, O., 2017, The Wheeler diagram, flattening theory, and time: Marine and Petroleum Geology, v. 86, p. 1417–1430, doi:10.1016/j.marpetgeo.2017.07.034.

QGIS.org, 2024, QGIS Geographic Information System.

Quinn, D.P., and Ehlmann, B.L., 2019, A PCA-based framework for determining remotely sensed geological surface orientations and their statistical quality: Earth and Space Science, v. 6, p. 1378–1408, doi:10.1029/2018EA000416.

Reesink, A.J.H., and Bridge, J.S., 2011, Evidence of bedform superimposition and flow unsteadiness in unit-bar deposits, South Saskatchewan River, Canada: Journal of Sedimentary Research, v. 81, p. 814–840, doi:10.2110/jsr.2011.69.

Salese, F., Kleinhans, M.G., Mangold, N., Ansan, V., McMahon, W., De Haas, T., and Dromart, G., 2020, Estimated minimum life span of the Jezero fluvial delta (Mars): Astrobiology, v. 20, p. 977–993, doi:10.1089/ast.2020.2228.

Sambrook Smith, G.H., Ashworth, P.J., Best, J.L., Lunt, I.A., Orfeo, O., and Parsons, D.R., 2009, The sedimentology and alluvial architecture of a large braid bar, Río Paraná, Argentina: Journal of Sedimentary Research, v. 79, p. 629–642, doi:10.2110/jsr.2009.066.

Schneider, C.A., Rasband, W.S., and Eliceiri, K.W., 2012, NIH Image to ImageJ: 25 years of image analysis: Nature Methods, v. 9, p. 671–675, doi:10.1038/nmeth.2089.

Schon, S.C., Head, J.W., and Fassett, C.I., 2012, An overfilled lacustrine system and progradational delta in Jezero Crater, Mars: implications for Noachian climate: Planetary and Space Science, v. 67, p. 28–45, doi:10.1016/j.pss.2012.02.003.

Shanmugam, G., 2021, Mass Transport, Gravity Flows, and Bottom Currents: Downslope and Alongslope Processes and Deposits: Elsevier, 571 p., doi:10.1016/C2019-0-03665-5.

Sharma, S., Pascuzzo, A., Uckert, K., Abbey, W., Bhartia, R., Berger, E., and Gómez, F., 2024, Multi-instrument image correlation for in situ planetary science on Mars: Institute of Electrical and Electronics Engineers, Aerospace Conference, Big Sky, Montana, 13 p., doi:10.1109/AERO58975.2024.10521366.

Simon, J.I., Hickman-Lewis, K., Cohen, B.A., Mayhew, L.E., Shuster, D.L., Debaille, V., Hausrath, E.M., Weiss, B.P., Bosak, T., Zorzano, M.-P., Amundsen, H.E.F., Beegle, L.W., Bell J.F., III, Benison, K.C., Berger, E.L., Beyssac, O., Brown, A.J., Calef, F., Casademont, T.M., Clark, B., Clavé, E., Crumpler, L., Czaja, A.D., Fairén, A.G., Farley, K.A., Flannery, D.T., Fornaro, T., Forni, O., Gómez, F., Goreva, Y., Gorin, A., Hand, K.P., Hamran, S.-E., Henneke, J., Herd, C.D.K., Horgan, B.H.N., Johnson, J.R., Joseph, J., Kronyak, R.E., Madariaga, J.M., Maki, J.N., Mandon, L., McCubbin, F.M., McLennan, S.M., Moeller, R.C., Newman, C.E., Núñez, J.I., Pascuzzo, A.C., Pedersen, D.A., Poggiali, G., Pinet, P., Quantin-Nataf, C., Rice, M., Rice, J.W., Jr., Royer, C., Schmidt, M., Sephton, M., Sharma, S., Siljeström, S., Stack, K.M., Steele, A., Sun, V.Z., Udry, A., VanBommel, S., Wadhwa, M., Wiens, R.C., Williams, A.J., and Williford, K.H., 2023, Samples collected from the floor of Jezero Crater with the Mars 2020 *Perseverance* rover: Journal of Geophysical Research, Planets, v. 128, no. e2022JE007474, doi:10.1029/2022JE007474.

St. Clair, M., Million, C., and Rice, M., 2022, Software tools for rapid analysis of Mastcam-Z multispectral data: 53rd Lunar and Planetary Science Conference, The Woodlands, Texas, no. 2533, https://www.hou.usra.edu/meetings/lpsc2022/pdf/2533.pdf.

Stack, K.M., Williams, N.R., Calef, F., Sun, V.Z., Williford, K.H., Farley, K.A., Eide, S., Flannery, D., Hughes, C., Jacob, S.R., Kah, L.C., Meyen, F., Molina, A., Quantin-Nataf, C., Rice, M., Russell, P., Scheller, E., Seeger, C.H., Abbey, W.J., Adler, J.B., Amundsen, H., Anderson, R.B., Angel, S.M., Arana, G., Atkins, J., Barrington, M., Berger, T., Borden, R., Boring, B., Brown, A., Carrier, B.L., Conrad, P., Dypvik, H., Fagents, S.A., Gallegos, Z.E., Garczynski, B., Golder, K., Gomez, F., Goreva, Y., Gupta, S., Hamran, S.-E., Hicks, T., Hinterman, E.D., Horgan, B.N., Hurowitz, J., Johnson, J.R., Lasue, J., Kronyak, R.E., Liu, Y., Madariaga, J.M., Mangold, N., McClean, J., Miklusicak, N., Nunes, D., Rojas, C., Runyon, K., Schmitz, N., Scudder, N., Shaver, E., SooHoo, J., Spaulding, R., Stanish, E., Tamppari, L.K., Tice, M.M., Turenne, N., Willis, P.A., and Yingst, A.R., 2020, Photogeologic map of the *Perseverance* rover field site in Jezero Crater constructed by the Mars 2020 science team: Space Science Reviews, v. 216, no. 127, doi:10.1007/s11214-020-00739-x.

Stack, K.M., Ives, L.R.W., Gupta, S., Lamb, M.P., Tebolt, M., Caravaca, G., Grotzinger, J.P., Russell, P., Shuster, D.L., Williams, A.J., Amundsen, H., Alwmark, S., Annex, A.M., Barnes, R., Bell, J., Beyssac, O., Bosak, T., Crumpler, L.S., Dehouck, E., Gwizd, S.J., Hickman-Lewis, K., Horgan, B.H.N., Hurowitz, J., Kalucha, H., Kanine, O., Lesh, C., Maki, J., Mangold, N., Randazzo, N., Seeger, C., Williams, R.M.E., Brown, A., Cardarelli, E., Dypvik, H., Flannery, D., Frydenvang, J., Hamran, S.-E., Núñez, J.I., Paige, D., Simon, J.I., Tice, M., Tate, C., and Wiens, R.C., 2024, Sedimentology and stratigraphy of the Shenandoah formation, western fan, Jezero Crater, Mars: Journal of Geophysical Research, Planets, v. 129, no. e2023JE008187, doi:10.1029/2023JE008187.

Summons, R.E., Amend, J.P., Bish, D., Buick, R., Cody, G.D., Des Marais, D.J., Dromart, G., Eigenbrode, J.L., Knoll, A.H., and Sumner, D.Y., 2011, Preservation of martian organic and environmental records: final report of the Mars biosignature working group: Astrobiology, v. 11, p. 157–181, doi:10.1089/ast.2010.0506.

Sun, V.Z., Hand, K.P., Stack, K.M., Farley, K.A., Simon, J.I., Newman, C., Sharma, S., Liu, Y., Wiens, R.C., Williams, A.J., Tosca, N., Alwmark, S., Beyssac, O., Brown, A., Calef, F., Cardarelli, E.L., Clavé, E., Cohen, B., Corpolongo, A., Czaja, A.D., Del Sesto, T., Fairen, A., Fornaro, T., Fouchet, T., Garczynski, B., Gupta, S., Herd, C.D.K., Hickman-Lewis, K., Horgan, B., Johnson, J., Kinch, K., Kizovski, T., Kronyak, R., Lange, R., Mandon, L., Milkovich, S., Moeller, R., Núñez, J., Paar, G., Pyrzak, G., Quantin-Nataf, C., Shuster, D.L., Siljestrom, S., Steele, A., Tice, M., Toupet, O., Udry, A., Vaughan, A., and Wogsland, B., 2023, Overview and results from the Mars 2020 *Perseverance* rover's first science campaign on the Jezero Crater floor: Journal of Geophysical Research, Planets, v. 128, no. e2022JE007613, doi:10.1029/2022JE007613.

Talling, P.J., Masson, D.G., Sumner, E.J., and Malgesini, G., 2012, Subaqueous sediment density flows: depositional processes and deposit types: Sedimentology, v. 59, p. 1937–2003, doi:10.1111/j.1365-3091.2012.01353.x.

Tebolt, M., Stack, K.M., Goudge, T.A., Ives, L.R.W., Gupta, S., Caravaca, G., Barnes, R., Paar, G., and Randazzo, N., 2025, Characterizing the facies and stratigraphy of the Enchanted Lake area in Jezero Crater, Mars: Journal of Geophysical Research, Planets, v. 130, no. e2023JE008278, doi:10.1029/2023JE008278.

USGS Astrogeology Science Center, 2009, Mars Viking Colorized Global Mosaic 232m, Astropedia: U.S. Geological Survey, https://astrogeology.usgs.gov/search/map/mars_viking_colorized_global_mosaic_232m.

van Burkalow, A., 1945, Angle of repose and angle of sliding friction: an experimental study: Geological Society of America, Bulletin, v. 56, p. 669–707, doi:10.1130/0016-7606(1945)56[669:AORAAO]2.0.CO;2.

Van Wagoner, J.C., Posamentier, H.W., Mitchum, R.M., Vail, P.R., Sarg, J.F., Loutit, T.S., and Hardenbol, J., 1988, An overview of the fundamentals of sequence stratigraphy and key definitions, *in* Wilgus, C.K., Hastings, B.S., Posamentier, H., Wagoner, J.V., Ross, C.A., and Kendall, C.G.St.C., eds., Sea-Level Changes: An Integrated Approach: SEPM, v. 42, p. 39–46, doi:10.2110/pec.88.01.0039.

van Yperen, A.E., Poyatos-Moré, M., Holbrook, J.M., and Midtkandal, I., 2020, Internal mouth-bar variability and preservation of subordinate coastal processes in low-accommodation proximal deltaic settings (Cretaceous Dakota Group, New Mexico, USA): The Depositional Record, v. 6, p. 431–458, doi:10.1002/dep2.100.

van Yperen, A.E., Holbrook, J.M., Poyatos-Moré, M., and Midtkandal, I., 2024, Backwater length estimates in modern and ancient fluvio-deltaic settings: review and proposal of standardized workflows: Earth-Science Reviews, v. 250, no. 104692, doi:10.1016/j.earscirev.2024.104692.

Villette, J., Mangold, N., Kite, E.S., Conway, S.J., and Le Deit, L., 2025, The sporadic fluvial regime of Pliva Vallis, the outlet valley of Jezero Crater lake, Mars: Journal of Geophysical Research, Planets, v. 130, no. e2024JE008862, doi:10.1029/2024JE008862.

Weiss, B.P., Nachon, M., Siebach, K., Farley, K.A., Stack, K.M., Bosak, T., Bell, J.F., Benison, K.C., Czaja, A.D., Debaille, V., Hausrath, E.M., Herd, C.D.K., Hickman-Lewis, K., Mayhew, L.E., Sephton, M.A., Sholes, S.F., Shuster, D.L., Siljeström, S., Simon, J.I., Wadhwa, M., and Zorzano, M.-P., 2024, *Perseverance* samples from the Jezero upper fan: 55th Lunar and Planetary Science Conference, The Woodlands, Texas, no. 1843, https://www.hou.usra.edu/meetings/lpsc2024/pdf/1843.pdf.

Wentworth, C.K., 1922, A scale of grade and class terms for clastic sediments: The Journal of Geology, v. 30, p. 377–392, doi:10.1086/622910.

Werner, S.C., 2008, The early martian evolution: constraints from basin formation ages: Icarus, v. 195, p. 45–60, doi:10.1016/j.icarus.2007.12.008.

Wheeler, H.E., 1964, Baselevel, lithosphere surface, and time-stratigraphy: Geological Society of America, Bulletin, v. 75, p. 599–610, doi:10.1130/0016-7606(1964)75[599:BLSAT]2.0.CO;2.

Wiens, R.C., and Maurice, S.A., 2021, Mars 2020 SuperCam Bundle: Planetary Data System (PDS) Geosciences (GEO) Node, doi:10.17189/1522646.

Wiens, R.C., Maurice, S., Robinson, S.H., Nelson, A.E., Cais, P., Bernardi, P., Newell, R.T., Clegg, S., Sharma, S.K., Storms, S., Deming, J., Beckman, D., Ollila, A.M., Gasnault, O., Anderson, R.B., André, Y., Michael Angel, S., Arana, G., Auden, E., Beck, P., Becker, J., Benzerara, K., Bernard, S., Beyssac, O., Borges, L., Bousquet, B., Boyd, K., Caffrey, M., Carlson, J., Castro, K., Celis, J., Chide, B., Clark, K., Cloutis, E., Cordoba, E.C., Cousin, A., Dale, M., Deflores, L., Delapp, D., Deleuze, M., Dirmyer, M., Donny, C., Dromart, G., George Duran, M., Egan, M., Ervin, J., Fabre, C., Fau, A., Fischer, W., Forni, O., Fouchet, T., Fresquez, R., Frydenvang, J., Gasway, D., Gontijo, I., Grotzinger, J., Jacob, X., Jacquinod, S., Johnson, J.R., Klisiewicz, R.A., Lake, J., Lanza, N., Laserna, J., Lasue, J., Le Mouélic, S., Legett, C., Leveille, R., Lewin, E., Lopez-Reyes, G., Lorenz, R., Lorigny, E., Love, S.P., Lucero, B., Madariaga, J.M., Madsen, M., Madsen, S., Mangold, N., Manrique, J.A., Martinez, J.P., Martinez-Frias, J., McCabe, K.P., McConnochie, T.H., McGlown, J.M., McLennan, S.M., Melikechi, N., Meslin, P.-Y., Michel, J.M., Mimoun, D., Misra, A., Montagnac, G., Montmessin, F., Mousset, V., Murdoch, N., Newsom, H., Ott, L.A., Ousnamer, Z.R., Pares, L., Parot, Y., Pawluczyk, R., Glen Peterson, C., Pilleri, P., Pinet, P., Pont, G., Poulet, F., Provost, C., Quertier, B., Quinn, H., Rapin, W., Reess, J.-M., Regan, A.H., Reyes-Newell, A.L., Romano, P.J., Royer, C., Rull, F., Sandoval, B., Sarrao, J.H., Sautter, V., Schoppers, M.J., Schröder, S., Seitz, D., Shepherd, T., Sobron, P., Dubois, B., Sridhar, V., Toplis, M.J., Torre-Fdez, I., Trettel, I.A., Underwood, M., Valdez, A., Valdez, J., Venhaus, D., and Willis, P., 2020, The SuperCam instrument suite on the NASA Mars 2020 rover: body unit and combined system tests: Space Science Reviews, v. 217, doi:10.1007/s11214-020-00777-5.

Wiens, R.C., Udry, A., Beyssac, O., Quantin-Nataf, C., Mangold, N., Cousin, A., Mandon, L., Bosak, T., Forni, O., McLennan, S.M., Sautter, V., Brown, A., Benzerara, K., Johnson, J.R., Mayhew, L., Maurice, S., Anderson, R.B., Clegg, S.M., Crumpler, L., Gabriel, T.S.J., Gasda, P., Hall, J., Horgan, B.H.N., Kah, L., Legett, C., Madariaga, J.M., Meslin, P.-Y., Ollila, A.M., Poulet, F., Royer, C., Sharma, S.K., Siljeström, S., Simon, J.I., Acosta-Maeda, T.E., Alvarez-Llamas, C., Angel, S.M., Arana, G., Beck, P., Bernard, S., Bertrand, T., Bousquet, B., Castro, K., Chide, B., Clavé, E., Cloutis, E., Connell, S., Dehouck, E., Dromart, G., Fischer, W., Fouchet, T., Francis, R., Frydenvang, J., Gasnault, O., Gibbons, E., Gupta, S., Hausrath, E.M., Jacob, X., Kalucha, H., Kelly, E., Knutsen, E., Lanza, N., Laserna, J., Lasue, J., Le Mouélic, S., Leveille, R., Lopez Reyes, G., Lorenz, R., Manrique, J.A., Martinez-Frias, J., McConnochie, T., Melikechi, N., Mimoun, D., Montmessin, F., Moros, J., Murdoch, N., Pilleri, P., Pilorget, C., Pinet, P., Rapin, W., Rull, F., Schröder, S., Shuster, D.L., Smith, R.J., Stott, A.E., Tarnas, J., Turenne, N., Veneranda, M., Vogt, D.S., Weiss, B.P., Willis, P., Stack, K.M., Williford, K.H., and Farley, K.A., 2022, Compositionally and density stratified igneous terrain in Jezero Crater, Mars: Science Advances, v. 8, no. eabo3399, doi:10.1126/sciadv.abo3399.

Williams, R.M.E., Grotzinger, J.P., Dietrich, W.E., Gupta, S., Sumner, D.Y., Wiens, R.C., Mangold, N., Malin, M.C., Edgett, K.S., Maurice, S., Forni, O., Gasnault, O., Ollila, A., Newsom, H.E., Dromart, G., Palucis, M.C., Yingst, R.A., Anderson, R.B., Herkenhoff, K.E., Le Mouélic, S., Goetz, W., Madsen, M.B., Koefoed, A., Jensen, J.K., Bridges, J.C., Schwenzer, S.P., Lewis, K.W., Stack, K.M., Rubin, D., Kah, L.C., Bell, J.F., Farmer, J.D., Sullivan, R., Van Beek, T., Blaney, D.L., Pariser, O., Deen, R.G., MSL Science Team, Kemppinen, O., Bridges, N., Johnson, J.R., Minitti, M., Cremers, D., Edgar, L., Godber, A., Wadhwa, M., Wellington, D., McEwan, I., Newman, C., Richardson, M., Charpentier, A., Peret, L., King, P., Blank, J., Weigle, G., Schmidt, M., Li, S., Milliken, R., Robertson, K., Sun, V., Baker, M., Edwards, C., Ehlmann, B., Farley, K., Griffes, J., Miller, H., Newcombe, M., Pilorget, C., Rice, M., Siebach, K., Stolper, E., Brunet, C., Hipkin, V., Léveillé, R., Marchand, G., Sobrón Sánchez, P., Favot, L., Cody, G., Steele, A., Flückiger, L., Lees, D., Nefian, A., Martin, M., Gailhanou, M., Westall, F., Israël, G., Agard, C., Baroukh, J., Donny, C., Gaboriaud, A., Guillemot, P., Lafaille, V., Lorigny, E., Paillet, A., Pérez, R., Saccoccio, M., Yana, C., Aparicio, C.A., Caride Rodríguez, J., Carrasco Blázquez, I., Gómez Gómez, F., Elvira, J.G., Hettrich, S., Lepinette Malvitte, A., Marín Jiménez, M., Frías, J.M., Soler, J.M., Torres, F.J.M., Molina Jurado, A., Sotomayor, L.M., Muñoz Caro, G., Navarro López, S., González, V.P., García, J.P., Rodriguez Manfredi, J.A., Planelló, J.J.R., Alejandra Sans Fuentes, S., Sebastian Martinez, E., Torres Redondo, J., O'Callaghan, R.U., Zorzano Mier, M.-P., Chipera, S., Lacour, J.-L., Mauchien, P., Sirven, J.-B., Manning, H., Fairén, A., Hayes, A., Joseph, J., Squyres, S., Thomas, P., Dupont, A., Lundberg, A., Melikechi, N., Mezzacappa, A., DeMarines, J., Grinspoon, D., Reitz, G., Prats, B., Atlaskin, E., Genzer, M., Harri, A.-M., Haukka, H., Kahanpää, H., Kauhanen, J., Paton, M., Polkko, J., Schmidt, W., Siili, T., Fabre, C., Wray, J., Wilhelm, M.B., Poitrasson, F., Patel, K., Gorevan, S., Indyk, S., Paulsen, G., Bish, D., Schieber, J., Gondet, B., Langevin, Y., Geffroy, C., Baratoux, D., Berger, G., Cros, A., Uston, C.D., Lasue, J., Lee, Q.-M., Meslin, P.-Y., Pallier, E., Parot, Y., Pinet, P., Schröder, S., Toplis, M., Lewin, É., Brunner, W., Heydari, E., Achilles, C., Oehler, D., Sutter, B., Cabane, M., Coscia, D., Szopa, C., Robert, F., Sautter, V., Nachon, M., Buch, A., Stalport, F., Coll, P., François, P., Raulin, F., Teinturier, S., Cameron, J., Clegg, S., Cousin, A., DeLapp, D., Dingler, R., Jackson, R.S., Johnstone, S., Lanza, N., Little, C., Nelson, T., Williams, R.B., Jones, A., Kirkland, L., Treiman, A., Baker, B., Cantor, B., Caplinger, M., Davis, S., Duston, B., Fay, D., Hardgrove, C., Harker, D., Herrera, P., Jensen, E., Kennedy, M.R., Krezoski, G., Krysak, D., Lipkaman, L., McCartney, E., McNair, S., Nixon, B., Posiolova, L., Ravine, M., Salamon, A., Saper, L., Stoiber, K., Supulver, K., Van Beek, J., Zimdar, R., French, K.L., Iagnemma, K., Miller, K., Summons, R., Goesmann, F., Hviid, S., Johnson, M., Lefavor, M., Lyness, E., Breves, E., Dyar, M.D., Fassett, C., Blake, D.F., Bristow, T., DesMarais, D., Edwards, L., Haberle, R., Hoehler, T., Hollingsworth, J., Kahre, M., Keely, L., McKay, C., Bleacher, L., Brinckerhoff, W., Choi, D., Conrad, P., Dworkin, J.P., Eigenbrode, J., Floyd, M., Freissinet, C., Garvin, J., Glavin, D., Harpold, D., Mahaffy, P., Martin, D.K., McAdam, A., Pavlov, A., Raaen, E., Smith, M.D., Stern, J., Tan, F., Trainer, M., Meyer, M., Posner, A., Voytek, M., Anderson, R.C., Aubrey, A., Beegle, L.W., Behar, A., Brinza, D., Calef, F., Christensen, L., Crisp, J.A., DeFlores, L., Feldman, J., Feldman, S., Flesch, G., Hurowitz, J., Jun, I., Keymeulen, D., Maki, J., Mischna, M., Morookian, J.M., Parker, T., Pavri, B., Schoppers, M., Sengstacken, A., Simmonds, J.J., Spanovich, N., de la Torre Juarez, M., Vasavada, A.R., Webster, C.R., Yen, A., Archer, P.D., Cucinotta, F., Jones, J.H., Ming, D., Morris, R.V., Niles, P., Rampe, E., Nolan, T., Fisk, M., Radziemski, L., Barraclough, B., Bender, S., Berman, D., Dobrea, E.N., Tokar, R., Vaniman, D., Leshin, L., Cleghorn, T., Huntress, W., Manhès, G., Hudgins, J., Olson, T., Stewart, N., Sarrazin, P., Grant, J., Vicenzi, E., Wilson, S.A., Bullock, M., Ehresmann, B., Hamilton, V., Hassler, D., Peterson, J., Rafkin, S., Zeitlin, C., Fedosov, F., Golovin, D., Karpushkina, N., Kozyrev, A., Litvak, M., Malakhov, A., Mitrofanov, I., Mokrousov, M., Nikiforov, S., Prokhorov, V., Sanin, A., Tretyakov, V., Varenikov, A., Vostrukhin, A., Kuzmin, R., Clark, B., Wolff, M., McLennan, S., Botta, O., Drake, D., Bean, K., Lemmon, M., Lee, E.M., Sucharski, R., Hernández, M.Á. de P., Blanco Ávalos, J.J., Ramos, M., Kim, M.-H., Malespin, C., Plante, I., Muller, J.-P., González, R.N., Ewing, R., Boynton, W., Downs, R., Fitzgibbon, M., Harshman, K., Morrison, S., Kortmann, O., Williams, A., Lugmair, G., Wilson, M.A., Jakosky, B., Zunic, T.B., Frydenvang, J., Kinch, K., Stipp, S.L.S., Boyd, N., Campbell, J.L., Gellert, R., Perrett, G., Pradler, I., VanBommel, S., Jacob, S., Owen, T., Rowland, S., Savijärvi, H., Boehm, E., Böttcher, S., Burmeister, S., Guo, J., Köhler, J., García, C.M., Mellin, R.M., Schweingruber, R.W., McConnochie, T., Benna, M., Franz, H., Bower, H., Brunner, A., Blau, H., Boucher, T., Carmosino, M., Atreya, S., Elliott, H., Halleaux, D., Rennó, N., Wong, M., Pepin, R., Elliott, B., Spray, J., Thompson, L., Gordon, S., Williams, J., Vasconcelos, P., Bentz, J., Nealson, K., Popa, R., Moersch, J., Tate, C., Day, M., Kocurek, G., Hallet, B., Sletten, R., Francis, R., McCullough, E., Cloutis, E., ten Kate, I.L., Arvidson, R., Fraeman, A., Scholes, D., Slavney, S., Stein, T., Ward, J., Berger, J., and Moores, J.E., 2013. Martian fluvial conglomerates at Gale Crater: Science, v. 340, p. 1068–1072, doi:10.1126/science.1237317.

Winsemann, J., Lang, J., Polom, U., Loewer, M., Igel, J., Pollok, L., and Brandes, C., 2018, Ice-marginal forced regressive deltas in glacial lake basins: geomorphology, facies variability and large-scale depositional architecture: BOREAS, v. 47, p. 973–1002, doi:10.1111/bor.12317.

Winsemann, J., Lang, J., Fedele, J.J., Zavala, C., and Hoyal, D.C.J.D., 2021, Re-examining models of shallow-water deltas: insights from tank experiments and field examples: Sedimentary Geology, v. 421, no. 105962, doi:10.1016/j.sedgeo.2021.105962.

Wordsworth, R.D., 2016, The climate of early Mars: Annual Review of Earth and Planetary Sciences, v. 44, p. 381–408, doi:10.1146/annurev-earth-060115-012355.

Zavala, C., Liu, H.-Q., Li, X.-B., Trobbiani, V., Li, Y., Arcuri, M., and Zorzano, A., 2024, High-frequency lacustrine sequence stratigraphy of clastic lakes: lessons from ancient successions: Journal of Palaeogeography, v. 13, p. 621–645, doi:10.1016/j.jop.2024.08.004.

Zecchin, M., and Catuneanu, O., 2013, High-resolution sequence stratigraphy of clastic shelves I: units and bounding surfaces: Marine and Petroleum Geology, v. 39, p. 1–25, doi:10.1016/j.marpetgeo.2012.08.015.

Zurek, R.W., and Smrekar, S.E., 2007, An overview of the Mars Reconnaissance Orbiter (MRO) science mission: Journal of Geophysical Research, v. 112, doi:10.1029/2006JE002701.

Received 26 February 2025; accepted 28 August 2025.